Diploma Thesis

The Lagrangian Exploration Module

Generation of homogeneous and isotropic turbulence with little mean flow for Lagrangian experiments

Robert Zimmermann

Göttingen, November 4, 2008

Georg-August-Universität Göttingen

&

Max-Planck-Institut für Dynamik und Selbstorganisation

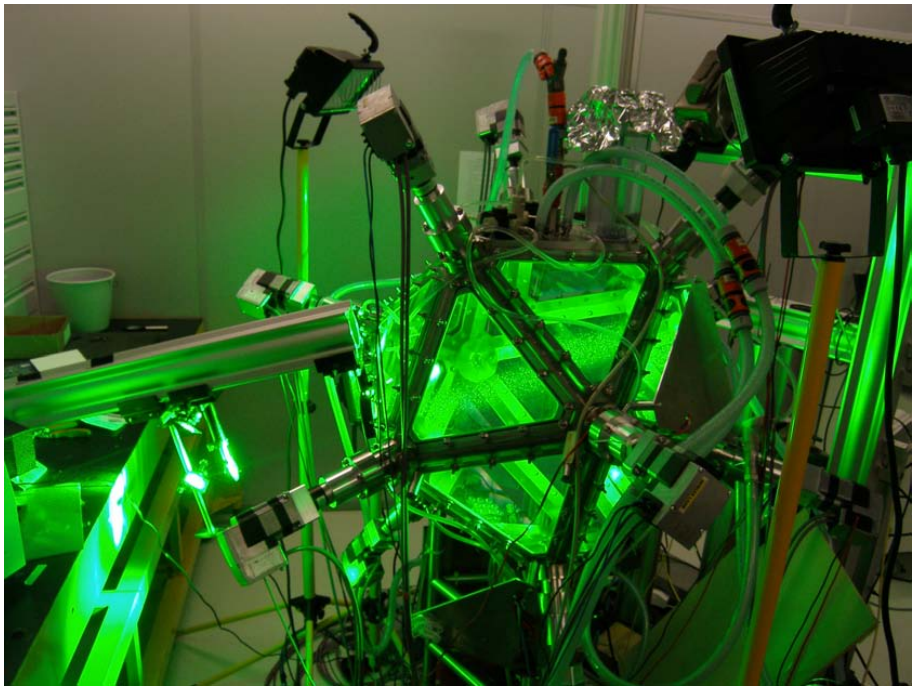

Contents

I Abstract

We designed and built an apparatus that generates nearly homogeneous and isotropic turbulence with a small mean flow. The apparatus is shaped as an icosahedron, and contains 140 liters of water. The flow is driven by 12 independently controlled propellers, each located at one of the vertices of the icosahedron. We carried out Lagrangian particle tracking measurements experiments with measurement volumes up to a size of $10 \times 10 \times 10$ $[cm^3]$, which is comparable with the integral length scale of the turbulent flow. The apparatus generates nearly homogeneous and isotropic turbulence with a Taylor microscale Reynolds number $R_\lambda \approx 350$. The measured mean flow was found to be less than 20% of the fluctuating velocity throughout the observed volume. We also measured the Lagrangian $n-$th order structure functions of position, $R_n(\tau) = \langle |\mathbf{x}(t+\tau) - \mathbf{x}(t)|^n \rangle$, and velocity, $K_n(\tau) = \langle |\mathbf{v}(t+\tau) - \mathbf{v}(t)|^n \rangle$, in the flow and compared the measurements with theoretical predictions from Zybin *et al* [1]. At $R_\lambda \approx 200$, we measured the Lagrangian structure functions of position up to the ninth order, and found that they were proportional to $\tau^{0.9\,n}$ in the inertial range.

II Introduction

Turbulence is a phenomenon which we encounter every day. Starting from the way vapor rises from a hot cup of coffee, to the mixing of milk and coffee caused by stirring, to the combustion process in a car engine, to pipe flows and a thunderstorm in the evening, turbulence plays a major role.

Predominant in every flow are inertial forces and damping frictional, or viscous, forces. If the viscous forces dominate, the flow is organized in lamina, hence it is referred to as a laminar flow. An increase in the flow speed leads to an increase in the importance of inertia. When this happens, perturbations arising from the boundaries (e.g. propellers) or from body forces acting on the flow are not damped out and sum up until the flow breaks up into eddies of different sizes, which are advected by the mean flow. The flow is then called turbulent.

Although the equations that describe a flow are known since the time of Navier and Stokes [2], it is still not possible to predict the behavior of turbulent flows. The reason for this lies in the fact that these equations are hardly ever analytically solvable. In 1941, Kolmogorov [3] established a universal, statistical approach to describe turbulence. In this approach the flow is characterized by means of distribution and autocorrelation functions. Due to his work and that of his successors it is possible to estimate the shape of these functions for a sufficiently turbulent flow. Although the original idea was formulated in the Eulerian framework, i.e. by observing a fixed region in the flow, new theoretical insights (see e.g. [4, 5]) were gained from models using the Lagrangian framework. The latter describes the flow by trajectories of fluid elements or particles. One would like to test these theories but the difficulty lies in that they are only applicable where the turbulence is statistically homogenous and isotropic. The creation of experimental conditions fulfilling these two requirements is already a hard task. In addition, further problems arise from the measurement techniques available.

For a long time only Eulerian measurements were accessible to the experimentalist. In 1971 [6], fluid elements were followed in a comoving coordinate system by introducing particles in the flow for the first time. These Lagrangian measurement techniques have enabled scientists to gain better understanding of processes such as the mixing of two different fluids or the properties of scalar fields like temperature or pressure [7]. However, to follow particles for sufficiently long times, Lagrangian measurement techniques require the mean flow to be small compared to the fluctuations in the particles' velocity over a large volume.

This requirement, however, is difficult to be met by apparatuses such as wind tunnels or mixers. Additional problems for typical mixers in testing Kolmogorov's theories lie in the absence of local isotropy and homogeneity over a sufficiently large observation volume.

In the current research project, the Lagrangian Exploration Module (LEM) will be presented as an apparatus meeting both isotropy and homogeneity requirements over a region comparable to the size of the biggest eddies. Furthermore, the LEM has a small mean-flow, thus providing ideal conditions for Lagrangian experiments on turbulent flows. To achieve these properties, the apparatus is shaped as an icosahedron, and the flow is driven by twelve independently controlled propellers, each at one of the vertices of the icosahedron. This setup enables us to also investigate the influence of different forcings on the flow.

Furthermore, we compared four different ways of driving the flow. For two of the four forcings, a detailed study on their influence on the mean flow was carried out.

Lagrangian Particle Tracking measurements were performed on the LEM to characterize the machine. Parts of the results were compared with a so far untested prediction on the Lagrangian structure functions from Zybin *et al* [1].

The present work is organized as follows:
Chapters III and IV provide the theoretical and experimental background. The experimental setup is explained in chapter V and the analysis methods are described in chapter VI. The results are subdivided into three main parts. Basic properties of the apparatus, such as Reynolds number and velocities are discussed in section VII.3. The influence of different forcings is investigated in section VII.4, and the predictions of Zybin *et al* [1] on the shape of the Lagrangian structure functions of position and velocity are compared with our experimental results in section VII.5.

A resume of the results is provided in chapter VIII.

III Theoretical Background

III.1 Describing a flow

Describing a simple flow from a molecular point of view is, however, not practical due to the large number of molecules present. One, therefore, turns to a continuum approach, as employed for example by Euler, Navier and Stokes.

All physical properties of the flow are then described by a field $\mathbf{A}(\mathbf{X}, t)$ or $\phi(\mathbf{X}, t)$, where the fields are assumed to be smooth.

The following is mostly based on references [8] and [9]. Further details can also be found under [10], [2] and [11].

III.2 Hydrodynamics

III.2.1 Continuum equation

In classical physics mass is conserved. For fluid dynamics mass conservation can be expressed in terms of the density ρ:

$$\frac{\partial}{\partial t}\int_V \rho \, dV = \int_{\partial V} \rho \, \mathbf{u} \, dA \tag{III.1}$$

where $\mathbf{u}$ is the fluid velocity through the surface ∂V of the volume V .

Using Gauss' Law we get

$$\begin{aligned} \frac{\partial}{\partial t}\int_V \rho \, dV &= \int_V \nabla \cdot (\rho \, \mathbf{u}) \, dV \\ \Leftrightarrow \qquad \frac{\partial}{\partial t}\rho &= \nabla \cdot (\rho \, \mathbf{u}) \end{aligned} \tag{III.2}$$

A constant density reduces equation (III.2) to

$$\nabla \cdot \mathbf{u} = 0 \tag{III.3}$$

Consequently there are neither sinks nor sources in flows of incompressible fluids.

III.2.2 Euler equation

In the middle of the 18th century Euler introduced the idea of internal pressure. Using this concept one can consider a small box with an edge length Δx and calculate

the forces acting upon it. In the non-viscous case only pressure and inertial force apply. To conserve momentum both forces have to be equal.

$$\begin{aligned} \overbrace{-\Delta p_i \cdot (\Delta x)^2}^{F_{pressure}} &= \overbrace{\rho\,(\Delta x)^3\,\frac{d}{dt}u_i}^{F_{inertial}} \\ \Leftrightarrow \quad -\frac{\Delta p_i}{\Delta x} &= \rho\,\frac{d}{dt}u_i \end{aligned} \tag{III.4}$$

Going to infinitesimally small sizes one can write

$$\rho\,\frac{d}{dt}\mathbf{u}(\mathbf{x},t) = -\nabla p \tag{III.5}$$

The total derivative $\frac{d}{dt}\phi(\mathbf{x},t)$ of an arbitrary field depending only on position and time is

$$\begin{aligned} \frac{d}{dt}\phi(\mathbf{x},t) &= \frac{\partial}{\partial t}\phi(\mathbf{x},t) + \frac{\partial}{\partial \mathbf{x}}\phi(\mathbf{x},t)\,\frac{\partial \mathbf{x}}{\partial t} \\ &= \left[\frac{\partial}{\partial t} + \mathbf{u}(\mathbf{x},t)\cdot\nabla\right]\phi(\mathbf{x},t) \end{aligned} \tag{III.6}$$

The term in brackets is called the comoving time derivative or the substantial time derivative. Applying equation (III.6) to equation (III.5) one gets

$$\rho\left(\frac{\partial}{\partial t} + \mathbf{u}(\mathbf{x},t)\cdot\nabla\right)\mathbf{u}(\mathbf{x},t) = -\nabla\mathbf{p} \tag{III.7}$$

The result (III.7) is a nonlinear equation. Frictional forces, that have been neglected so far, will introduce further terms to (III.7). As friction becomes relevant when calculating drag forces, it is necessary to expand the considerations above to viscous fluids. Details of the derivation are presented in the following section.

III.2.3 Navier–Stokes equation

The Euler equation (III.7) can be improved by refining the pressure force term. The surface forces acting on the small box, introduced in the section before, originate from the molecular forces inside the box. Using the stress tensor τ_{ij} – also known from solid state physics – we get[1]

$$\rho\frac{du_j}{dt} = \frac{\partial \tau_{ij}}{\partial x_i} + f_j \tag{III.8}$$

where $\mathbf{f}$ describes the body forces which act on the fluid.

The stress tensor can be decomposed into the hydrostatic pressure, p, and a stress term, s_{ij}:

$$\tau_{ij} = -p\delta_{ij} + s_{ij} \tag{III.9}$$

[1]Repeated indices are implicitly summed over (Einstein notation).

In general, the stress tensor, s_{ij}, is a complicated tensor depending on the fluid properties, the flow and in some case also on the history of the flow. As a simplification, we will focus on so-called Newtonian fluids, e.g. water. They are characterized by the fact that the fluid is isotropic, with the stress, $s_{ij}(\mathbf{r}, t)$, vanishing for the fluid at rest and depending only on the strain rate at the same point $\mathbf{r}$ and at the same time t. For small strain rates, $\frac{\partial u_k}{\partial x_l}$, we can assume that $s_{ij}(\mathbf{r}, t)$ does only depend linearly on spatial derivatives, $\frac{\partial u_k}{\partial x_l}$.

s_{ij} can decomposed into a symmetric, $\frac{1}{2}(s_{ij} + s_{ji})$, and an antisymmetric part, $\frac{1}{2}(s_{ij} - s_{ji})$. If we picture a fluid with a uniform rotation of angular velocity, ω, it has the velocity, $\mathbf{u}s(\mathbf{r}) = \omega \times \mathbf{r}$. Applying this field to the symmetric and antisymmetric part one can easily see that only the symmetric part of s_{ij} vanishes. However, if the fluid is rotating as a whole, there is no relative motion between fluid elements, i.e. the stress vanishes. Consequently, s_{ij} has to be symmetric. In other words

$$s_{ij} = s_{ji} \tag{III.10}$$

The most general linear symmetric combination of $\frac{\partial u_k}{\partial x_i}$ for an isotropic fluid [2] is:

$$s_{ij} = a\left(\frac{\partial u_j}{\partial x_i} + \frac{\partial u_i}{\partial x_j}\right) + b\left(\frac{\partial u_k}{\partial x_k}\delta_{ij}\right) \tag{III.11}$$

where a and b are parameters. Equation (III.11) can be rewritten to

$$s_{ij} = \underbrace{\mu\left(\frac{\partial u_j}{\partial x_i} + \frac{\partial u_i}{\partial x_j} - \frac{2}{3}\frac{\partial u_k}{\partial x_k}\delta_{ij}\right)}_{\text{rate of shear tensor}} + \underbrace{\zeta\left(\frac{\partial u_k}{\partial x_k}\delta_{ij}\right)}_{\text{rate of expansion tensor}} \tag{III.12}$$

The parameter μ is the so-called dynamic viscosity, and ζ is the bulk viscosity[2], the two material parameters describe how the fluid reacts to shear and changes in its volume. As an approximation they are assumed to be independent of velocity, position and time. The derivative of equation (III.12) is

$$\begin{aligned}
\frac{\partial}{\partial x_j}s_{ij} &= \mu\left(\frac{\partial}{\partial x_i}\frac{\partial u_j}{\partial x_j} + \frac{\partial}{\partial x_j}\frac{\partial u_i}{\partial x_j} - \frac{2}{3}\frac{\partial}{\partial x_j}\frac{\partial u_k}{\partial x_k}\delta_{ij}\right) + \zeta\left(\frac{\partial}{\partial x_j}\frac{\partial u_k}{\partial x_k}\delta_{ij}\right) \\
&= \mu\frac{\partial}{\partial x_j}\frac{\partial u_i}{\partial x_j} + \mu\left(\frac{\partial}{\partial x_i}\frac{\partial u_j}{\partial x_j} - \frac{2}{3}\frac{\partial}{\partial x_j}\frac{\partial u_k}{\partial x_k}\delta_{ij}\right) + \zeta\left(\frac{\partial}{\partial x_j}\frac{\partial u_k}{\partial x_k}\delta_{ij}\right) \\
&= \mu\frac{\partial^2 u_i}{\partial x_j^2} + \mu\left(\frac{\partial}{\partial x_i}\frac{\partial u_j}{\partial x_j} - \frac{2}{3}\frac{\partial}{\partial x_i}\frac{\partial u_k}{\partial x_k}\right) + \zeta\left(\frac{\partial}{\partial x_i}\frac{\partial u_k}{\partial x_k}\right) \\
&= \mu\frac{\partial^2 u_i}{\partial x_j^2} + \left(\frac{\mu}{3} + \zeta\right)\left(\frac{\partial}{\partial x_i}\frac{\partial u_k}{\partial x_k}\right)
\end{aligned} \tag{III.13}$$

Inserting the obtained stress tensor in equation (III.8) we get

$$\begin{aligned}
\rho\frac{d\,u_j}{dt} &= -\frac{\partial p}{\partial x_i}\delta_{ij} + \mu\frac{\partial^2 u_j}{\partial x_i^2} + \left(\frac{\mu}{3} + \zeta\right)\left(\frac{\partial}{\partial x_j}\frac{\partial u_k}{\partial x_k}\right) + f_j \\
\Leftrightarrow \quad \rho\left[\frac{\partial}{\partial t} + \mathbf{u}\cdot\nabla\right]\mathbf{u} &= -\nabla p + \mu\nabla^2\mathbf{u} + \left(\frac{\mu}{3} + \zeta\right)\nabla\left(\nabla\cdot\mathbf{u}\right) + \mathbf{f}
\end{aligned} \tag{III.14}$$

[2] also called second viscosity

This is the Navier–Stokes equation for a compressible Newtonian fluid. It should be noted that μ and ζ are depending on the temperature and the pressure. Thus, further information is needed to fully describe a flow. For incompressible fluids the divergence of $\mathbf{u}$ vanishes, so that the Navier–Stokes equation turns into

$$\rho\left[\frac{\partial}{\partial t}+\mathbf{u}\cdot\nabla\right]\mathbf{u}=-\nabla p+\mu\nabla^2\mathbf{u}+\mathbf{f} \tag{III.15}$$

III.2.4 The nondimensional Navier-Stokes equation

Usually the Navier-Stokes equation is presented in a dimensionless form. The advantage of such a representation is that different hydrodynamical setups can be compared. So long as their relative dimensions correspond, they'll be described by the same (dimensionless) equation. Accordingly their flow behavior should be the same.

Introducing a length scale, $\mathcal{L}$, and a velocity scale, $\mathcal{U}$, we can write

$$\hat{\mathbf{x}}=\frac{\mathbf{x}}{\mathcal{L}}\quad\text{and}\quad\hat{t}=t\frac{\mathcal{L}}{\mathcal{U}} \tag{III.16}$$

as well as

$$\hat{\mathbf{p}}=\frac{\mathbf{p}}{\rho\mathcal{U}^2}\quad\text{and}\quad\hat{\mathbf{u}}=\frac{\mathbf{u}}{\mathcal{L}} \tag{III.17}$$

Plugging these new parameters into equation (III.15) one obtains:

$$\frac{\partial\mathbf{u}}{\partial t}+\mathbf{u}\cdot\nabla\mathbf{u}=-\nabla\mathbf{p}+\frac{1}{Re}\nabla^2\mathbf{u} \tag{III.18}$$

where Re is the so-called Reynolds number

$$Re=\frac{\rho\mathcal{U}\,\mathcal{L}}{\mu}=\frac{\mathcal{U}\,\mathcal{L}}{\nu} \tag{III.19}$$

with $\nu\equiv\frac{\mu}{\rho}$ denoting the kinematic viscosity. It is advantageous to use the kinematic viscosity, ν, instead of the two parameters density, ρ and dynamic viscosity, μ, to describe the fluid properties.

As already indicated, setups having the same boundary conditions and the same Reynolds number develop the same flow characteristics. The Reynolds number can be seen as the ratio between the magnitude of inertia forces arising from $\partial_t\mathbf{u}+\mathbf{u}\cdot\nabla\mathbf{u}$ and the viscous forces represented by $\nabla^2\mathbf{u}$. For sufficiently high Reynolds number the flow is dominated by inertia and frictional forces are negligible. Moreover, one obtains the Euler equation (III.7) in the limit of $Re\to\infty$.

III.3 Introduction to turbulent flows

Due to its non-linear term the Navier-Stokes equation (III.15) is sensitive to initial conditions and boundary conditions. An additional problem arises from the pressure term. Although this term is linear, one has to use Green's function to compute the

pressure field. Consequently, this term depends on the complete flow field and its boundary conditions.

For a small Reynolds number, Re, the viscous term of the Navier-Stokes equation dominates. Thus small perturbations arising from the boundaries or body forces acting on the fluid are damped out, and one can find steady-state[3] solutions of the Navier-Stokes equation. The flow is then organized in stationary streamlines. In other words, the flow can be pictured as fluid lamina which glide along each other but do not cross. Hence, this type of flow is called *laminar*.

For an increasing Reynolds number perturbations arising from the boundaries or body forces acting on the fluid are not damped out anymore and the lamina break up into many eddies, which are advected with the mean-flow. The system evolves into a spatio-temporal chaotic system which is called *turbulence*. In this regime mixing is enhanced, but also the drag force acting on a body moving through the flow is higher in a turbulent flow than in the laminar case.

For an easier characterization, it is useful to decompose the velocity field, $\mathbf{u}(\mathbf{x}, t)$, into a mean flow field $\langle \mathbf{u}(\mathbf{x}) \rangle$ plus the turbulent fluctuations of the velocity $\mathbf{u}'(\mathbf{x}, t)$:

$$\mathbf{u}(\mathbf{x}, t) = \langle \mathbf{u}(\mathbf{x}) \rangle + \mathbf{u}'(\mathbf{x}, t) \tag{III.20}$$

The theories referred to in this text assume a negligible mean flow.

III.4 Energy cascade

The description of turbulence relies very much on one concept first introduced by Richardson: the energy cascade.

Starting a flow through e.g. propellers creates big whirls of a size, L, and a Reynolds number, $Re(L)$. For sufficiently strong forcing at this scale L, the Reynolds number, $Re(L)$, is large enough to neglect viscosity and resulting energy losses. However, the injected energy has to be dissipated.

Following Richardson's proposal each big vortex then breaks up into several smaller vortices. The latter would be of a different length scale l and more importantly of a smaller Reynolds number $Re(l) < Re(L)$. Energy conservation dictates that all energy from the first generation of vortices has to be passed to the next. The child vortices again split into more vortices of even smaller size l' and $Re(l') < Re(l)$. This self-similar process is repeated until molecular interactions start playing a role, which occurs at $Re \approx 1$.

In 1941, Kolmogorov put Richardson's proposal in mathematical terms by making three hypotheses. According to these, energy conservation dictates that the rate of energy transfered from a length scale to its child vortices is the same at all scales in the energy cascade. Thus, one can define the energy dissipation rate, ε, as the dissipated energy per unit time and unit mass. Since the rate of transfered energy per unit mass equals the rate of energy dissipated, ε, it is also called energy transfer rate.

[3] Of course, only if the boundary conditions are not time dependent.

Furthermore, he postulated that the size of the smallest eddies depends only on the viscosity of the fluid and the energy transfer rate. It is common to use the letter, η, to indicate the smallest (Kolmogorov) scale.

Kolmogorov also stated, that the statistical behavior of eddies much smaller than the biggest length scales, L, but still much bigger than the smallest eddies depends only on the energy transfer rate, ε. This range is called inertial range. A size characteristic for this range is the Taylor micro-scale, λ. The application of Kolmogorov's hypotheses will be shown in section III.6.

A visualization of the Richardson cascade is provided in figure III.1.

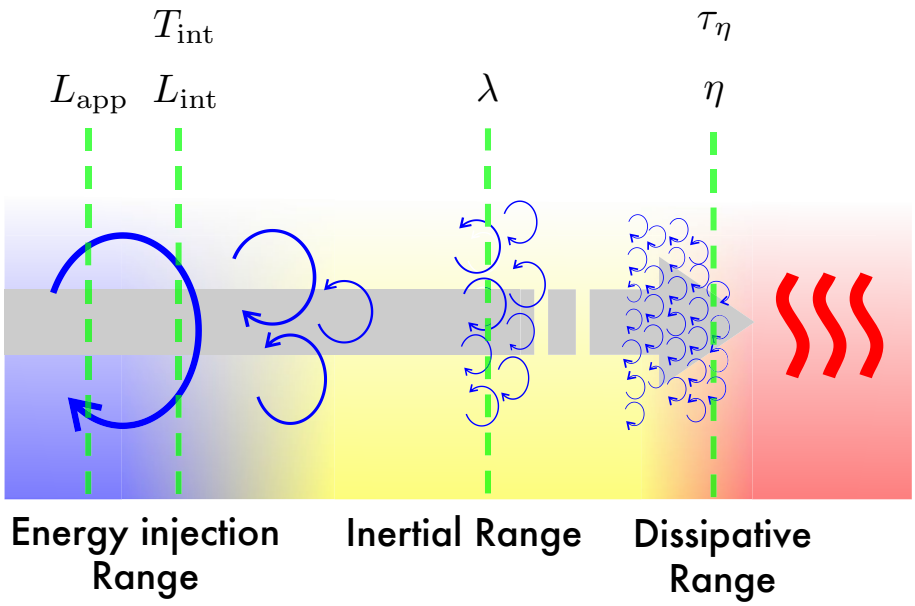

Figure III.1: Sketch of the Richardson cascade. The system (of size L_{app}) injects energy at the size L characterizing the biggest whirls. These whirls break up into smaller whirls, which break up into even smaller eddies, and so forth. This process is stopping in the dissipative range when viscosity becomes non-neglectible and the injected energy is finally converted to heat.

III.5 Dimensional arguments

Dimensional arguments provide a useful tool for order of magnitude estimates. The Navier-Stokes equation (III.15) is fully described by length, velocity, pressure, density and viscosity.

For example, the characteristic time scale, T, for the big whirls with size $\mathcal{L}$ and characteristic velocity, $\mathcal{U}$, is

$$T \sim \frac{\mathcal{L}}{\mathcal{U}} \tag{III.21}$$

Further, the energy dissipation rate ε is measured in $\left[\frac{kg\,m^2}{s^2}\cdot\frac{1}{kg}\cdot\frac{1}{s}\right]=\left[\frac{m^2}{s^3}\right]$ and is fully characterized by the velocity and the length scale of turbulent eddies. The only possible combination using only these parameters with the same units is:

$$\varepsilon \sim \frac{\mathcal{U}^3}{\mathcal{L}} \tag{III.22}$$

III.6 K41

In 1941, Kolmogorov [3] derived important properties of turbulent flows using Richardson's idea of the energy cascade. His publications had such a big impact on the turbulence community that his theory is referred to as K41.

III.6.1 Kolmogorov's hypotheses & scales

Before Kolmogorov's hypotheses can be introduced one has to define local homogeneity and isotropy.

Looking at region $\mathcal{G}$ in a turbulent flow, let $\mathbf{x}^{(1)}$, … , $\mathbf{x}^{(N)}$ represent a set of points within $\mathcal{G}$. Choosing one of the $\mathbf{x}^{(i)}$ as a reference $\mathbf{x}^{(0)}$, one can introduce new coordinates

$$\mathbf{y}^{(i)} = \mathbf{x}^{(i)} - \mathbf{x}^{(0)}$$

and velocity differences

$$\mathbf{v}(\mathbf{y}^{(i)}) = \mathbf{U}(\mathbf{x}^{(i)}, t) - \mathbf{U}(\mathbf{x}^{(0)}, t)$$

Every $\mathbf{v}(\mathbf{y}^{(i)})$ is itself a random variable following a probability density function dependent on the flow properties at $\mathbf{y}^{(i)}$. Allowing $f_v \equiv f_v\left(\mathbf{y}^{(1)}, \ldots, \mathbf{y}^{(N)}\right)$ to designate the joint probability density function (PDF) of finding a given set of velocities $\mathbf{v}(\mathbf{y}^{(1)}), \ldots, \mathbf{v}(\mathbf{y}^{(N)})$ at the N points and the same time, the following definitions are possible:

local homogeneity A turbulent flow is locally homogeneous in $\mathcal{G}$, if, for a set $\mathbf{y}^{(n)}(n = 1, \ldots, N)$, the PDF f_v is independent of the exact choice of the reference point $\mathbf{x}^{(0)}$.

local isotropy The turbulent flow is locally isotropic in $\mathcal{G}$ if it is locally homogeneous and invariant to rotations and reflections.

With the help of these definitions Kolmogorov established three hypotheses

hypothesis of local isotropy In any turbulent flow with a sufficiently high Reynolds number, the turbulence is – to a good approximation – locally isotropic for a sufficiently small $\mathcal{G}$ not situated near the boundaries or singularities of the flow.

first similarity hypothesis For locally isotropic turbulent flows f_v is only determined by the kinematic viscosity, ν, and the energy dissipation rate, ε.

second similarity hypothesis If the separation between the vectors $\mathbf{y}^{(m)}$ is large compared to the Kolmogorov scale, η, the joint PDF f_v is uniquely determined by the energy dissipation rate, ε, and does not depend on ν.

Kolmogorov's hypotheses make it possible to describe the turbulent flow in terms of statistical measures.

Kolmogorov realized that, according the Richardson cascade model, the smallest scales of motion occur at a Reynolds number equal to 1.

Using the first similarity hypothesis and equation (III.22), one can define the smallest length scale η, the smallest velocity scale u_η and the smallest time scale τ_η:

$$\begin{aligned} 1 = Re = \frac{\eta\, u_\eta}{\nu} = \frac{\eta^{4/3}\,\varepsilon^{1/3}}{\nu} \\ \Rightarrow \eta = (\nu^3/\varepsilon)^{1/4} \end{aligned} \tag{III.23}$$

Similarly for the smallest velocity scale, u_η, one arrives at:

$$\begin{aligned} 1 = Re = \frac{\eta\, u_\eta}{\nu} = \frac{u_\eta^4}{\varepsilon\,\nu} \\ \Rightarrow u_\eta = (\varepsilon\nu)^{1/4} \end{aligned} \tag{III.24}$$

And for the smallest time scale, τ_η, one deduces:

$$\tau_\eta = \frac{\eta}{u_\eta} = (\nu/\varepsilon)^{1/2} \tag{III.25}$$

One generally speaks of η, u_η and τ_η as Kolmogorov scales.

The Reynolds number of the flow is

$$Re = \frac{U\,L}{\nu} \tag{III.26}$$

where L represent the biggest scale of the flow and U the velocity corresponding to this scale. Thus, we can relate the Kolmogorov scales to the biggest scales of the flow

$$\eta/L \propto Re^{-3/4} \tag{III.27a}$$

$$u_\eta/U \propto Re^{-1/4} \tag{III.27b}$$

$$\tau_\eta/T \propto Re^{-1/2} \tag{III.27c}$$

where $T \equiv \frac{L}{U}$ is the time scale of the flow.

A consequence of the equations (III.27) is that the Kolmogorov scales and the biggest scales of the flow become more separated with increasing Re. This conclusion is sometimes referred to as *Kolmogorov's idea of scale separation.*

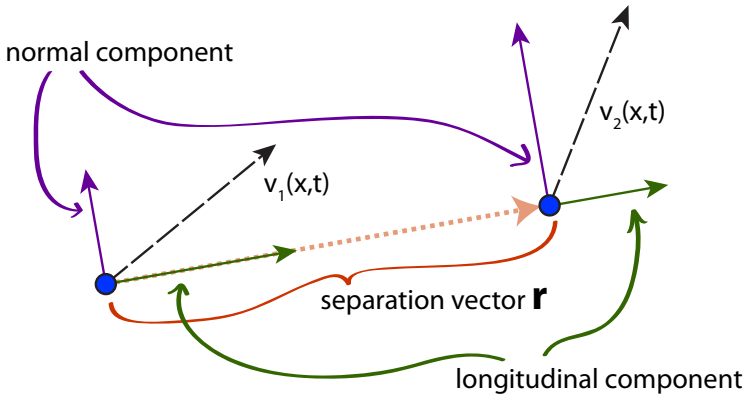

Figure III.2: Sketch of D_{NN} and D_{LL}. Two uid elements indicated by the blue dots have a velocity $\mathbf{v}_1$ and $\mathbf{v}_2$, and are separated by the separation vector $\mathbf{r}$. The longitudinal second order structure function, D_{LL}, is computed from the component of the velocities parallel to $\mathbf{r}$, whereas the transverse, or normal, second order structure function is build using the components of the velocity vectors which are normal to $\mathbf{r}$.

III.6.2 Second order structure functions D_{LL} and D_{NN}

The Eulerian second order structure function is de ned as

$$D_{ij}(\mathbf{r}\ \mathbf{x}\ t) = [U_i(\mathbf{x}+\mathbf{r}\ t) \quad U_i(\mathbf{x}\ t)]\,[U_j(\mathbf{x}+\mathbf{r}\ t) \quad U_j(\mathbf{x}\ t)] \tag{III.28}$$

where the index refers to one component of the velocity vector $\mathbf{U}$ and the brackets denote the average over several similarly prepared experiments.

In terms of $\mathbf{y}$ and $\mathbf{v}$ i.e. substituting $\mathbf{r} = \mathbf{y}^{(2)} \quad \mathbf{y}^{(1)}$, $\mathbf{x} = \mathbf{y}^{(1)} + \mathbf{x}^{(0)}$ and choosing the origin to be $\mathbf{x}^{(0)}$:

$$D_{ij}(\mathbf{y}^{(2)} \quad \mathbf{y}^{(1)}\ \mathbf{y}^{(1)} + \mathbf{x}^{(0)}\ t) = \quad v_i(\mathbf{y}^{(2)}) \quad v_i(\mathbf{y}^{(1)}) \quad v_j(\mathbf{y}^{(2)}) \quad v_j(\mathbf{y}^{(1)}) \tag{III.29}$$

Assuming local isotropy i.e. $r \ll \mathbf{r}$ much smaller than the biggest length scale then D_{ij} is neither dependent on its second argument $\mathbf{x}$ in equation (III.28) nor on $\mathbf{x}^{(0)}$ in equation (III.29). It only depends on $\mathbf{r}$ and can be written $D_{ij}(\mathbf{r}\ t)$. Seeing that it only depends on $\mathbf{r}$, D_{ij} can be split up into a term containing the inter-dependence between the vector components r_i and r_j and a term independent of these.

Such a representation would be

$$D_{ij} = A(r\ t)\ _{ij} + B(r\ t)\frac{r_i}{r}\frac{r_j}{r}$$

with two (yet) arbitrary functions $A(r\ t)$ and $B(r\ t)$. It is convenient to rotate the coordinate system such that $\mathbf{r}$ is $r \quad \mathbf{e}_x$. One obtains:

$$D_{LL} \ll D_{xx} = A(r\ t) + B(r\ t) = \quad (\quad v_x)^2 \tag{III.30}$$

$$D_{ij} = B(r\ t)\frac{r_i}{r}\frac{r_j}{r} = 0 \quad \text{with} \quad \mathrm{i} = \mathrm{j} \tag{III.31}$$

$$D_{NN} \ll D_{yy} = D_{zz} = A(r\ t) = \quad (\quad v_y)^2 \quad = \quad (\quad v_z)^2 \tag{III.32}$$

D_{LL} is the so-called longitudinal second order structure function, whereas D_{NN} denotes the transverse, or normal, second order structure function. An illustration of D_{NN} and D_{LL} is provided in figure III.2.

Combining the equations above we arrive at

$$D_{ij}(\mathbf{r},t) = D_{NN}(r,t)\delta_{ij} + [D_{LL}(r,t) - D_{NN}(r,t)]\,\frac{r_i r_j}{r^2} \tag{III.33}$$

In order to relate D_{NN} and D_{LL} consider again equation (III.29). Rewriting $v_i^{(k)} \equiv v_i(\mathbf{y}^k)$ for $k = 1$ or 2 and expanding equation (III.29) one calculates:

$$D_{ij}(\mathbf{r},t) = \left\langle v_i^{(1)} v_j^{(1)} \right\rangle + \left\langle v_i^{(2)} v_j^{(2)} \right\rangle - \left\langle v_i^{(1)} v_j^{(2)} \right\rangle - \left\langle v_i^{(2)} v_j^{(1)} \right\rangle \tag{III.34}$$

Because of isotropy $\left\langle v_i^{(1)} v_j^{(1)} \right\rangle = \left\langle v_i^{(2)} v_j^{(2)} \right\rangle$. By mirroring the coordinate system we get $\left\langle v_i^{(1)} v_j^{(2)} \right\rangle = \left\langle v_i^{(2)} v_j^{(1)} \right\rangle$. Thus

$$D_{ij}(\mathbf{r},t) = 2\left\langle v_i^{(1)} v_j^{(1)} \right\rangle - 2\left\langle v_i^{(1)} v_j^{(2)} \right\rangle = \frac{2}{3}\left\langle \mathbf{v}^2 \right\rangle - 2\left\langle v_i^{(1)} v_j^{(2)} \right\rangle \tag{III.35}$$

The derivative of (III.35) yields:

$$\frac{\partial D_{ij}}{\partial y_j^{(2)}} = -2\left\langle v_i^{(1)} \frac{\partial v_j^{(2)}}{\partial y_j^{(2)}} \right\rangle$$

The continuity equation dictates:

$$\frac{\partial v_j^{(2)}}{\partial y_j^{(2)}} = 0 \quad \Rightarrow \quad \frac{\partial D_{ij}}{\partial y_j^{(2)}} = 0$$

The same holds true for the derivative $\frac{\partial D_{ij}}{\partial y_j^{(1)}}$. Hence[4]:

$$\begin{aligned} 0 = \frac{\partial D_{ij}(\mathbf{r},t)}{\partial r_i} &= \frac{\partial}{\partial r_i}\left(D_{NN}(r,t)\delta_{ij}\right) + \frac{\partial}{\partial r_i}\left(\left[D_{LL}(r,t) - D_{NN}(r,t)\right]\frac{r_i r_j}{r^2}\right) \\ &= \frac{r_j}{r^2}\left[r\frac{\partial D_{LL}(r,t)}{\partial r} + 2\left(D_{LL}(r,t) - D_{NN}(r,t)\right)\right] \end{aligned} \tag{III.36}$$

Therefore:

$$D_{NN} = D_{LL} + \frac{r}{2}\frac{\partial D_{LL}(r,t)}{\partial r} \tag{III.37}$$

In consequence, D_{NN} is completely determined by D_{LL}. Assuming a statistically stationary turbulent flow the brackets $\langle\cdot\rangle$ denoting the average over identically or rather similarly prepared experiments can be replaced by a temporal average.

The term $(\varepsilon r)^{2/3}$ has the unit of velocity squared and can be used to create a non-dimensional second-order structure function $\hat{D}_{LL}(r/\eta)$.

$$D_{LL}(r) = (\varepsilon r)^{2/3}\hat{D}_{LL}(r/\eta)$$

For large r/η the second similarity hypothesis claims that D_{LL} is independent of ν. Since η is a function of ε and ν, to satisfy the hypothesis $\hat{D}$ cannot depend on r/η. I.e. $\hat{D}_{LL} = const = C_2$. Experiments have shown that C_2 is approximately 2.1. Plugging that into equation (III.37) we get

$$D_{NN} = D_{LL} + \frac{1}{3}D_{LL} = \frac{4}{3}D_{LL} = \frac{4}{3}C_2(\varepsilon r)^{2/3} \tag{III.38}$$

Equation (III.38) allows to measure the energy dissipation rate by investigating the compensated second order structure function

$$\varepsilon(r) \approx \left(\frac{D_{LL}}{C_2}\right)^{3/2}\frac{1}{r} = \left(\frac{3\,D_{NN}}{4\,C_2}\right)^{3/2}\frac{1}{r} \tag{III.39}$$

For sufficiently turbulent flows equation (III.39) shows a plateau in the inertial range.

[4] Auxiliary calculations using Einstein summation convention:

$$\frac{\partial}{\partial r_i}(D_{NN}(r,t)\delta_{ij}) = \frac{\partial D_{NN}(r,t)}{\partial r_i}\delta_{ij} + D_{NN}(r,t)\frac{\partial \delta_{ij}}{\partial r_i} = \frac{\partial D_{NN}(r,t)}{\partial r}\frac{\partial r}{\partial r_j} = \frac{r_j}{r}\frac{\partial D_{NN}(r,t)}{\partial r}$$

$$\begin{aligned} \frac{\partial}{\partial r_i}\left(r_i r_j r^{-2}\right) &= \frac{\partial r_i}{\partial r_i}r_j r^{-2} + \frac{\partial r_j}{\partial r_i}r_i r^{-2} + \frac{\partial r^{-2}}{\partial r_i}r_i r_j \\ &= 3r_j r^{-2} + r_i\delta_{ij}r^{-2} + \frac{\partial r^{-2}}{\partial r_i}r_i r_j \\ &= 3r_j r^{-2} + r_j r^{-2} - 2r_j r^{-2} \\ &= 2\frac{r_j}{r^2} \end{aligned}$$

$$\frac{r_i r_j}{r^2}\frac{\partial}{\partial r_i}D_{LL}(r,t) - \frac{r_i r_j}{r^2}\frac{\partial}{\partial r_i}D_{NN}(r,t) = \frac{r_j}{r^2}\left(r\frac{\partial D_{LL}(r,t)}{\partial r} - r\frac{\partial D_{NN}(r,t)}{\partial r}\right)$$

For $\mathbf{r}$ parallel to $\mathbf{e}_x$ we have $r_i r_j = 0$ for $i \neq j$. Hence, the two derivative terms of D_{NN} are the same and cancel each other.

III.6.3 Eulerian structure functions of order three and higher – D_{LLL} and D_p

The Eulerian structure function of order p is defined as

$$D_p = \left\langle \, |v_L(\mathbf{x}+\mathbf{r},t) - v_L(\mathbf{x},t)|^p \, \right\rangle \tag{III.40}$$

The second similarity hypothesis and dimensional analysis yields that D scales as

$$D_p = C_p \, (\varepsilon \; r)^{p/3} \tag{III.41}$$

where C_p is a constant. It should be noted that the predicted scaling exponent of $p/3$ for $p \neq 3$ has not been observed experimentally.

For the third order, an exact solution can be derived from the Navier-Stokes equation:

$$D_{LLL}(r,t) = -\frac{4}{5}\varepsilon \, r \tag{III.42}$$

Equation III.42 is called Kolmogorov $\frac{4}{5}$ law.

A detailed discussion of the Kolmogorov $\frac{4}{5}$ law as well as of higher order structure functions can be found in Frisch's book [10].

III.6.4 Eulerian Autocorrelation

Let

$$R_{ij}(\mathbf{r},t) \equiv \langle u_i(\mathbf{x}+\mathbf{r},t) u_j(\mathbf{x},t) \rangle \tag{III.43}$$

denote the Eulerian autocorrelation. In the case of homogeneous isotropic turbulence with zero mean velocity R_{ij} is independent of $\mathbf{x}$. Using the same arguments and the same notation already used to obtain (III.33) we get

$$\begin{aligned} R_{ij}(\mathbf{r},t) &= R_{NN}(r,t)\delta_{ij} + [R_{LL}(r,t) - R_{NN}(r,t)] \, \frac{r_i r_j}{r^2} \\ &= \langle u_L^2 \rangle \left(g(r,t)\delta_{ij} + [f(r,t) - g(r,t)] \, \frac{r_i r_j}{r^2} \right) \text{ with } \langle u_L^2 \rangle \equiv \left\langle (\mathbf{u}\cdot\mathbf{e}_r)^2 \right\rangle \end{aligned} \tag{III.44}$$

where $f \equiv R_{LL}/\langle u_L^2 \rangle$ is the longitudinal and $g \equiv R_{NN}/\langle u_L^2 \rangle$ is the transverse autocorrelation functions. In conformity with the continuity equation the following relation has to be valid:

$$\frac{\partial R_{ij}}{\partial r_j} = \frac{\partial}{\partial r_j} \langle u_i(\mathbf{x}+\mathbf{r},t) u_j(\mathbf{x},t) \rangle = \langle u_i(\mathbf{x}+\mathbf{r},t) \frac{\partial}{\partial r_j} u_j(\mathbf{x},t) \rangle = 0 \tag{III.45}$$

Analogous to equation (III.37) one deduces:

$$g(r,t) = f + \frac{r}{2} \frac{\partial f(r,t)}{\partial r} \tag{III.46}$$

Two distinct length scales can be defined from the autocorrelation f: the integral length scale, L, and the Taylor micro scale, λ. Since transverse and longitudinal functions are connected by equation (III.46) theses scales can also be computed from g.

III.6.5 Integral Length Scale

The longitudinal integral length scale is defined as

$$L_{LL} \equiv \int_0^\infty f(r,t)dr \tag{III.47}$$

whereas the transverse integral length scale is given by

$$\begin{aligned} L_{NN} &\equiv \int_0^\infty g(r,t)dr \\ &= \int_0^\infty f(r,t)dr + \int_0^\infty \frac{1}{2} r \frac{\partial}{\partial r} f(r,t)dr \\ &= L_{LL} + \left[\frac{1}{2} r f(r,t)\right]_0^\infty - \int_0^\infty \frac{1}{2} f(r,t)dr \end{aligned} \tag{III.48}$$

If $f(r,t)$ decays more rapidly than r^{-2}, the term $\left[\frac{1}{2} r f(r,t)\right]_0^\infty$ vanishes and hence

$$L_{NN} = \frac{1}{2} L_{LL} \tag{III.49}$$

The longitudinal integral length scale L_{LL} can be considered to be the scale of the biggest eddies. Since longitudinal and transverse integral length scale are related, it is common to use the integral length scale $L = L_{LL}$.

III.6.6 Taylor microscale & Taylor scale Reynolds number – R_λ

The second length scale which can be obtained from the autocorrelation f is the Taylor microscale $\lambda_f(t)$. Because of isotropy $f(r)$ is an even function assuming values below or equal to unity. Thus, the first derivate $f'(0,t)$ at the origin has to be zero. Furthermore, autocorrelation functions decrease at the origin. Consequently, the origin will be a maximum and the second derivative $f''(0,t)$ at that point will be non-positive. The Taylor microscale can then be defined as

$$\lambda_f(t) \equiv \left[-\frac{1}{2} f''(0,t)\right]^{-1/2} \tag{III.50}$$

Using equation (III.46) it is

$$\begin{aligned}
-\langle u^2\rangle f''(0,t) &= -\langle u^2\rangle \lim_{r\to 0}\frac{\partial^2}{\partial r^2} f(r,t) \\
&= -\lim_{r\to 0}\left\langle \left(\frac{\partial^2 u_L}{\partial r^2}\right)_{\mathbf{x}+\mathbf{e}_r r} u_L(\mathbf{x},t)\right\rangle \\
&= -\left\langle \left(\frac{\partial^2 u_L}{\partial x_L^2}\right) u_L\right\rangle \\
&= -\left\langle \frac{\partial}{\partial x_L}\left(u_L\frac{\partial u_L}{\partial x_L}\right)\right\rangle + \left\langle \left(\frac{\partial u_L}{\partial x_L}\right)^2\right\rangle \\
&= -\frac{\partial}{\partial x_L}\left\langle \left(u_L\frac{\partial u_L}{\partial x_L}\right)\right\rangle + \left\langle \left(\frac{\partial u_L}{\partial x_L}\right)^2\right\rangle \\
&= \left\langle \left(\frac{\partial u_L}{\partial x_L}\right)^2\right\rangle
\end{aligned} \tag{III.51}$$

Combining (III.51) and (III.50) it is

$$\left\langle \left(\frac{\partial u_L}{\partial x_L}\right)^2\right\rangle = \frac{2\,\langle u^2\rangle}{\lambda_f^2(t)} \tag{III.52}$$

$\lambda_g(t) \equiv \left[-\frac{1}{2}g''(0,t)\right]^{-1/2}$ is the transverse Taylor microscale, using equation (III.46) one can calculate the relation between longitudinal and transverse microscale.

$$\begin{aligned}
\lambda_g(t) &= \left[-\frac{1}{2}g''(0,t)\right]^{-1/2} \\
&= \left[-\frac{1}{2}\left(f'' + \lim_{r\to 0}\frac{r}{2}\frac{\partial^3 f(r,t)}{\partial r^3}\right)\right]^{-1/2} \\
&= \left[-\frac{1}{2}\left(f'' + \frac{1}{2}\lim_{r\to 0}\left[\frac{\partial}{\partial r}\left[r f''\right] - f''\right]\right)\right]^{-1/2} \\
&= \left[-\frac{1}{2}\left(f'' - \frac{1}{2}f''\right)\right]^{-1/2} \\
&= \frac{\lambda_f(t)}{\sqrt{2}}
\end{aligned} \tag{III.53}$$

For historic reasons, one usually talks about the Taylor microscale $\lambda = \lambda_g$.

It can be shown [9] that

$$\varepsilon = 15\,\nu\left\langle \left(\frac{\partial u_L}{\partial x_L}\right)^2\right\rangle \tag{III.54}$$

Using equation (III.53) and (III.52) it follows

$$\varepsilon = 15\,\nu\,\frac{u'^2}{\lambda_g^2} \tag{III.55}$$

This can be used to define the Taylor scale Reynolds number

$$R_\lambda \equiv \frac{u' \lambda_g}{\nu} \tag{III.56}$$

The relation between Re and R_λ can be easily shown

$$\begin{aligned} R_\lambda^2 &= \frac{u'^2 \lambda_g^2}{\nu^2} \\ &= 15\,\nu \frac{u'^2}{\varepsilon} \cdot \frac{u'^2}{\nu^2} \\ &= 15 \frac{l}{u'^3} \frac{u'^4}{\nu} \\ &= 15\,Re \end{aligned} \tag{III.57}$$

Thus, R_λ is the Reynolds number at the intermediate length scale λ_g lying between then η and L. There is no direct physical meaning of this length scale but that λ is well situated in the inertial range. In turbulence research it is common to use R_λ instead of Re as a measure for the strength of the turbulence. The magnitude of λ_g can be estimated by applying the definition of the Kolmogorov scales to equation (III.55). It is

$$\lambda_g = \sqrt{15}\,\tau_\eta\,u' \;\sim\; \sqrt{15}\,\eta\,R_\lambda^{1/2} \tag{III.58}$$

For example for intense turbulence of $R_\lambda \approx 660$ the Taylor micro scale is 100 times the Kolmogorov length scale but still only 1/44 of the integral length scale.

III.7 Limitations

The results obtained in the section III.6 are based on Kolmogorov's hypotheses and the Richardson cascade. Only Kolmogorov's four-fifth law (equation III.42) can be derived directly from the Navier-Stokes equation. Therefore, some limitations arise.

Landau pointed out (see [9], page 176), that the averaging process makes it impossible to find universal laws for the structure functions. The ensemble average over n realizations of the turbulent flow of a structure function D_p is

$$D_p^{avg} = \frac{1}{N} \sum_{i=1}^{N} D_i \tag{III.59}$$

and the average of their corresponding energy transfer rate ε_i

$$\varepsilon^{avg} = \frac{1}{N} \sum_{i=1}^{N} \varepsilon_i \tag{III.60}$$

Combining equations (III.41), (III.60) and (III.59) yields

$$\left(\frac{1}{N} \sum_{i=1}^{N} \varepsilon \right)^{p/3} = \frac{1}{N} \sum_{i=1}^{N} (\varepsilon_i)^{p/3} \tag{III.61}$$

Equation (III.61) can only be true for the third order structure function. Therefore, the structure functions depend on the way the turbulence is created.

A further problem emerges from the Richardson cascade picture. There the energy is strictly transfered from bigger whirls to their smaller child whirls. In nature smaller whirls can act also on bigger whirls. Furthermore, the child eddies do not necessarily occupy the same amount of volume than their parent eddy. This leads to a violation of the self similarity of the model.

Kolmogorov's requirements on the choice of $\mathcal{G}$ and the Reynolds number are experimentally vague. There is experimental evidence that the turbulence approaches local isotropy with increasing Re. Yet, at intense turbulence of $R_\lambda \approx 970$ the flow is still locally anisotropic [12, 7, 13, 14].

The limitations named above are usually referred to as *internal intermittency*. Newer models tried to improve K41 predictions, but we still lack of a good understanding of turbulence.

A locally isotropic flow regime is major hypothesis of most models. In [15] Bachelor investigated axisymmetric turbulence, which is still a strong constraint on the flow. For instance, for axisymmetric turbulence the Eulerian autocorrelation R_{ij} can be decomposed into four[5] dimensionless functions A, B, C and D depending on r and the ratio between the angular and radial velocity. Analogous to equation (III.46) the continuity equation dictates that A, B, C and D are related. However, this relation is also much more complicated than equation (III.46). Furthermore, it is possible to define four Taylor scales and four integral length scales. This complicates measurements and models further. Therefore, an isotropic flow is preferred in most models.

To investigate turbulence, wind tunnels and mixers were able to provide local isotropy and homogeneity to a good extent. However, in a wind tunnel the fluctuating velocity is typically 5% to 20% of the mean velocity. Many Lagrangian measurement techniques observe a small, fixed area. For example, particles in a wind tunnel sweeping through a $(50\ cm)^3$ observation volume at 5 $\frac{m}{s}$, pass the volume in average in $\frac{1}{10}s$. If the fluctuating velocity is small compared to the mean velocity, then the measured Lagrangian trajectories are only few τ_η (or even less) short. Therefore, the creation of mean velocities much smaller than the turbulent fluctuations is desired for Lagrangian measurements. It should be noted that it is also possible to extend the observation time of the particles by moving the observation volume with the flow. For example, Ayyalasomayajula *et al* [16] mounted the measurement equipment on a sledge which was moving with the mean velocity in the wind tunnel observed.

On the other hand, mixers like the very common *counterrotating von Kármán mixing flow*[6] i.e. a cylindrical tank with two counterrotating propellers at the top and the bottom, create an axisymmetric flow field with little mean flow within a very

[5] Remember that in isotropic turbulence R_{ij} is fully described by f and $\langle u_L \rangle$.
[6] This arrangement is also called French–Washing–Machine.

small region in the center of the apparatus. Unfortunately, the turbulent flow inside this region is not isotropic even at high Reynolds numbers [12]. The Lagrangian Exploration Module can be seen as six pairs of counterrotating von Kármán mixing flows interacting in one apparatus. As we show in chapter VII this arrangement provides a flow which is locally isotropic in a region of the size of the integral length scale and nearly negligible mean flow. More details on the setup of the machine can be found in chapter V.

IV Overview of measurement techniques

In the last hundred years of research in hydrodynamics and aerodynamics a broad collection of measurement techniques had been developed. A broad overview on techniques used in experimental fluid mechanics can be found in [17]. Nevertheless, this chapter introduces some common techniques. Particle tracking velocimetry will be explained in detail since it was used to obtain the data.

IV.1 Hot wire Anemometry

In hot wire anemometry [18] a current is passed through a thin wire and thus the wire is heated to a temperature T. The resistance of the wire is related to its temperature. Gas passing by the hot wire convects heat away and thus changes temperature, which consequently changes the resistance. Either the temperature or the current is kept constant and by measuring the other parameter as a function of time one can obtain the velocity at the wire. With hot wire anemometry it is not possible to determine the flow direction. Due to technical limitations this method can only be used in gas flows with a high mean flow.

IV.2 Laser Doppler Velocimetry

Laser–Doppler–Velocimetry (LDV) allows the non-intrusive measurement of velocity and acceleration at a small measurement volume. As pictured in figure IV.1, a laser beam is split in two. The frequency of one of the two beams is shifted by Δf (typically several MHz) using Bragg–reflexion in a so called Bragg–cell. Thereafter the beams are aligned such that they cross at the region of interest. The cigar shaped region is typically a few millimeters long and a few tenth of a millimeter wide. Because of interference a pattern of parallel planes with high light intensity is created. The distance Δx between the interference fringes is:

$$\Delta x = \frac{\lambda}{2 \sin(\phi/2)} \tag{IV.1}$$

where λ denotes the wave length of the laser and ϕ the angle between the two beams. Because of the slight frequency shift the stripes are moving with velocity $v_f = \Delta f \, \Delta x$. Particles passing the measurement volume blink. The frequency of the blinking light is the beat frequency of the fringes, which is Doppler shifted by the velocity component perpendicular to the fringes. A receiver, consisting of a photo multiplier

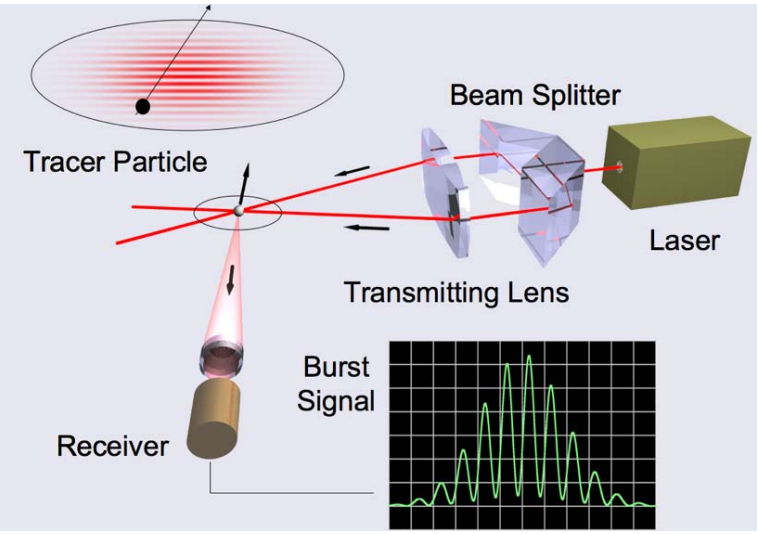

Figure IV.1: Sketch of a LDV system. Image courtesy of Holger Nobach. A laser beam is split in two part, whereas one is frequency shifted in a Bragg cell; both beams cross at the measurement volume and interfere; because of the frequency shift the interference stripe pattern is moving with a velocity $\mathbf{v}$; particles crossing the intersection, will blink with a frequency depending on their own velocity, the angle between the beams and the beat frequency; acceleration and velocity can be obtained from frequency of the beating signal

and fast signal processor, measures the light intensity as a function of time. The velocity is calculated from the frequency of the signal. As described in [19] it is possible to obtain particle accelerations from laser-Doppler measurements using also the change in frequency of the time the particle passes through the measurement volume. Unfortunately, only one particle at a time can be measured. Using two or three LDV systems, more components of the velocity can be obtained.

IV.3 Particle Image Velocimetry

Particle Image Velocimetry (PIV) (see e.g. the review by Adrian [20]) uses one camera to acquire a two dimensional velocity eld. A thin laser sheet is directed to illuminate a region in a ow seeded with small particles. One (or more) camera(s) is orientated at the illuminated region taking two consequent images. The time di erence between the images, t, is typically very small. Thus, either high speed lm cameras or special PIV cameras are used. The rst image is subdivided into small blocks and the cross correlation between each block and the image t later is calculated. The point with the maximum cross correlation is considered as the new position of the block. Thus, one can calculate the velocity of all blocks. Using more cameras it is possible to increase the accuracy and robustness of the measurement. Furthermore, two cameras observing from di erent angles enable to obtain three-dimensional velocity data on the plane de ned by the thin laser sheet.

IV.4 Tomographic Particle Image Velocimetry

Tomographic particle image velocimetry (tomo–PIV) is a recent development with which one can obtain three dimensional velocity fields. Three or four cameras are directed on an illuminated measurement volume and take synchronously images. By using tomographic methods two 3D density fields of the two image sets are created. Analogous to PIV, the cross correlation between a region from the first density field and the second field is calculated. The maximum in the cross correlation is considered to be the new position of the selected region. The velocity field can be obtained from the three–dimensional displacement of each block from t to $t + \Delta t$.

IV.5 Particle Tracking Velocimetry

Most measurement techniques (e.g. Hot wire Anemometry, PIV and LDV) allow observation from the Eulerian point of view, meaning that the velocity is measured at one – or several – fixed points in space. Measurement techniques working in the Lagrangian framework make it possible to follow fluid segments along their trajectories in the flow using particles as a probe.

In principle, Eulerian and Lagrangian measurements can be transformed into their counterpart. In the case of two-dimensional turbulent flows the transformation can be realized from PIV measurements [21, 22]. Yet, transforming three-dimensional Eulerian to Lagrangian fields (and vice versa) is still impossible due to the extremely high requirements on resolving the spatio-temporal structure of the flow. Therefore, the Lagrangian framework is more convenient to study Lagrangian correlations and structure functions, as well as particle dispersion and mixing.

The basic idea of Particle Tracking Velocimetry[1] (PTV) is to determine the three dimensional position of tracer particles in the flow at certain times and to build up the points into trajectories of particles. Afterwards the velocity and acceleration can be computed from the trajectories. To detect the tracer particles two ways have been created so far: using the Doppler shift of a scattered wave[2], and optical detection using digital cameras.

We are using an optical method with a calibration method proposed by Tsai [26].

IV.5.1 Experimental Setup

A laser beam or a bright light source illuminates particles in a measurement volume. The scattered light from a particle is detected by two or more high speed cameras looking from different angles into the volume. In other words particles produce an image on the image sensors of each camera. After taking synchronized movies, these are downloaded to a computer for the evaluation process.

[1] also called Lagrangian Particle Tracking (LPT)

[2] The scattered wave can either be created through ultrasound [23] or a modified LDV system [24]. It should be noted that it is also possible to use small sensors which are advected with the turbulent flows sending continuously their current status via an antenna [25].

The PTV method used in the experiment consists of the following three steps, which are: particle nding (IV.5.4), stereo matching (IV.5.5) and connection of the points to trajectories (IV.5.6). However, before a PTV system can be used is has to be calibrated according to the following camera model and calibration procedure.

IV.5.2 The Camera Model

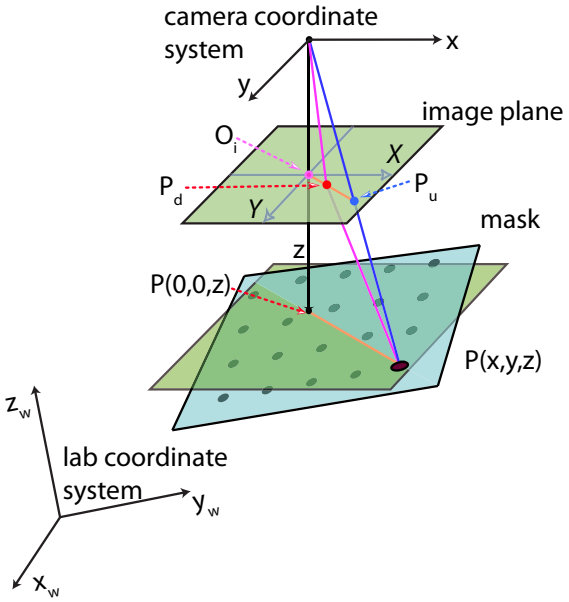

Figure IV.2: Sketch of the camera model proposed by Tsai [26]. The two green planes are parallel. For calibration a mask (blue) with a known dot pattern is moved along the z_w axis. It is assumed that the image is only distorted along the orange lines. This is the radial alignment constraint used in the calibration.

As proposed by Tsai [26], modern o -the-shelf cameras and lenses are well described by a pin hole camera with radial distortion but negligible tangential distortion.

The mathematical projection of a point in 3D onto an image sensor of a model camera can be done in four steps. A sketch of the di erent coordinate systems is provided in gure IV.2.

Step 1: A point $\begin{matrix} x_w \\ y_w \\ z_w \end{matrix}$ in the object world coordinate system can be transformed to the camera coordinate system by rigid body transformation

$$\begin{matrix} x \\ y \\ z \end{matrix} = \underline{\underline{\mathbf{R}}} \begin{matrix} x_w \\ y_w \\ z_w \end{matrix} + \mathbf{T} \tag{IV.2}$$

$\underline{\underline{\mathbf{R}}} = \begin{matrix} r_1 & r_2 & r_3 \\ r_4 & r_5 & r_6 \\ r_7 & r_8 & r_9 \end{matrix}$ is a 3 3 rotation matrix and $\mathbf{T} = \begin{matrix} T_x \\ T_y \\ T_z \end{matrix}$ a translation vector. Since $\underline{\underline{\mathbf{R}}}$ can be expressed in terms of three Eulerian angles and the

translation also has three degrees of freedom, this step involves six unknown parameters.

Step 2: Transformation of the 3D camera coordinates to ideal (undistorted) image coordinates (X_u, Y_u).

$$X_u = f\frac{x}{z} \qquad Y_u = f\frac{y}{z} \tag{IV.3}$$

where f is the distance between the projection center to the image sensor. Although f should be known from the camera's specifications and the focal length of the objetive, it is used a free fitting parameter during calibration. In fitting f possible distortions caused by the windows of the apparatus can be included and better accuracy can be achieved.

Step 3: Only radial distortion is considered to be relevant for modern lenses. The correction can be expressed as

$$X_d + D_x = X_u \qquad Y_d + D_y = Y_u \tag{IV.4}$$

with

$$D_x = X_d \left(\kappa_1 r^2 + \kappa_2 r^4 + \dots\right) \tag{IV.5a}$$

$$D_y = Y_d \left(\kappa_1 r^2 + \kappa_2 r^4 + \dots\right) \tag{IV.5b}$$

$$r = \sqrt{X_d^2 + Y_d^2} \tag{IV.5c}$$

Carrying out the correction only up to the first order provides good results at low computational costs and is numerically stable. The radial distortion factor κ_1 is introduced as another unknown parameter to be determined during calibration.

Step 4: The real image coordinate has to be transformed to the pixel representation in the computer:

$$X = X_f - C_x = \frac{s_x X_d}{d_x} \tag{IV.6a}$$

$$Y = Y_f - C_y = \frac{Y_d}{d_y} \tag{IV.6b}$$

with (X_f, Y_f) the position in pixels, (C_x, C_y) the position of the image center (in pixels), d_x and d_y the size of a pixel in x and y direction respectively and the so-called uncertainty image scale factor s_x. The latter allows to correct hardware issues of the cameras. In the case of an ideal sensor s_x is unity. However, it is kept as the ninth unknown parameter to be identified by the calibration.

The center of the image plane (C_x, C_y) as well as the size of a pixel (d_x, d_y) is assumed to be known.

All these steps need detailed information about the lab coordinate system, cameras, etc. The nine parameters can be determined using a calibration method described in the following subsection.

IV.5.3 Calibration

The four steps described in subsection IV.5.2 involve nine unknown parameters depending on the arrangement of the cameras, the cameras itself and the objectives. The calibration method proposed by Tsai [26] allows to determine these parameters in a robust and accurate way.

First, one has to take images of a known structure, such as a regular dot pattern with a marked center, at several known positions in the lab system. To do so one usually moves a plate[3] with a regular dot pattern along an axis in the lab system. To be compliant with figure IV.2, we will assume that the mask is moved in z_w–direction.

In a second step, the images are being processed such that one gets a set of 3D points $(x_w, y_w, z_w)_i$ in the lab system and their corresponding projection on the image plane (X_i, Y_i). If only radial distortion of the image is considered, we can always choose the rotation matrix $\underline{\underline{\mathbf{R}}}$ and $\mathbf{T}$ such that $\overline{\mathbf{O}_i\mathbf{P}_d}$ is parallel to $\overline{\mathbf{P}(0,0,z)\mathbf{P}(x,y,z)}$ (as displayed by the orange lines in figure IV.2). This can be rewritten as:

$$\begin{aligned} & (X_d, Y_d) \times (x, y) = 0 \\ \Leftrightarrow \quad & X_d \cdot y = Y_d \cdot x \end{aligned} \tag{IV.7}$$

Inserting equation (IV.2) into equation (IV.7) yields:

$$X_d\,(r_4\,x_w + r_5\,y_w + r_6\,z_w + T_y) = Y_d\,(r_1\,x_w + r_2\,y_w + r_3\,z_w + T_x) \tag{IV.8}$$

This constraint is called *radial alignment constraint*. Rearranging equation (IV.8), one can see that it yields a set of linear equations with seven unknowns.

$$\begin{bmatrix} Y_d\,x_w & Y_d\,y_w & Y_d\,z_w & Y_d & -X_d\,x_w & -X_d\,y_w & -X_d\,z_w \end{bmatrix} \cdot \mathbf{A} = X_d \tag{IV.9}$$

where $\mathbf{A} = \begin{bmatrix} T_y^{-1}\,s_x\,r_1 & T_y^{-1}\,s_x\,r_2 & T_y^{-1}\,s_x\,r_3 & T_y^{-1}\,s_x\,T_x & T_y^{-1}r_4 & T_y^{-1}r_5 & T_y^{-1}r_6 \end{bmatrix}^T$ contains the unknown parameters.

If the number of 3D points found is much higher than seven, equation (IV.9) is overdetermined. In this case one can find $\mathbf{A}$ with a least square fit. For any three dimensional rotation matrix $\underline{\underline{\mathbf{R}}}$ it is $\sum_{i=1}^{3} R_{ij}^2 = \sum_{j=1}^{3} R_{ij}^2 = 1$. Thus one can determine $|T_y|$, r_7, r_8, r_9 and s_x analytically.

The last three steps in the camera model can be combined to obtain the equations

$$f\frac{x}{z} = X_u = X\,\frac{d_x}{s_x}\left(1 + \kappa_1 r^2\right) \tag{IV.10a}$$

$$f\frac{y}{z} = Y_u = Y\,d_y\,\left(1 + \kappa_1 r^2\right) \tag{IV.10b}$$

Expressing x, y and z in terms of x_w, y_w and z_w yields:

$$f\frac{r_1\,x_w + r_2\,y_w + r_3\,z_w + T_x}{r_7\,x_w + r_8\,y_w + r_9\,z_w + T_z} = X\,\frac{d_x}{s_x}\left(1 + \kappa_1 r^2\right) \tag{IV.11a}$$

$$f\frac{r_3\,x_w + r_5\,y_w + r_6\,z_w + T_y}{r_7\,x_w + r_8\,y_w + r_9\,z_w + T_z} = Y\,d_y\left(1 + \kappa_1 r^2\right) \tag{IV.11b}$$

[3] Also called mask

Setting κ_1 to zero in a first run, one gains an overdetermined set of linear equations, which enables us to acquire good initial guesses for f and T_z. The precise values of κ_1, f and T_z can be found by employing a standard fitting scheme to equation (IV.11b) and the found 3D points. This calibration method allows an accurate and robust determination of the nine independent parameters in the camera model. It is as least as accurate as and more robust than optimization schemes working on all of the nine parameters at the same time.

IV.5.4 Particle Finding

The scattered light from the particle leaves a bright spot on the digital image. Such a spot has a size of several pixels and – in the case of spherical particles – can be approximated by a two-dimensional Gaussian with added noise. The spots are identified using a segmentation technique which considers every pixel with a intensity above a certain threshold as part of a spot.

Ouellette *et al* [27] discussed several methods to identify the center of a spot and tested these methods on their performance and accuracy. The discussed attempts are

Two-dimensional Gaussian: Homogenous spherical particles should – to a first approach – result in an intensity profile which can be described as a two-dimensional Gaussian. However, the fitting process is computationally expensive.

Two one-dimensional Gaussians: Fitting a one dimensional Gaussian in x direction and one Gaussian in y direction produces mostly the same accuracy as the two-dimensional Gaussian but the computational cost of the fitting are minimal since they can be calculated from an analytical solution.

Center-Of-Mass: Non-elliptical particles and particles[4] which are not uniform, will most likely produce a non-elliptical shape with several intensity peaks. In this case, the Center-Of-Mass can compute the approximate center of the spot with greater accuracy than a Gaussian approach.

Neural Networks: After training, also neural networks achieved a good accuracy even for noisy images.

All the experiments described with in this diploma thesis have been performed using spherical particles. Therefore, the two one-dimensional Gaussian method was sufficient.

IV.5.5 Stereo-matching

The stereo-matching code is explainded in figure IV.3. This algorithm is only able to find particles which create a light spot on all cameras. Thus, the selection of the threshold is the particle finding step is crucial to the stereo-matching process.

[4]For example: biological particles, such as algae and copepods

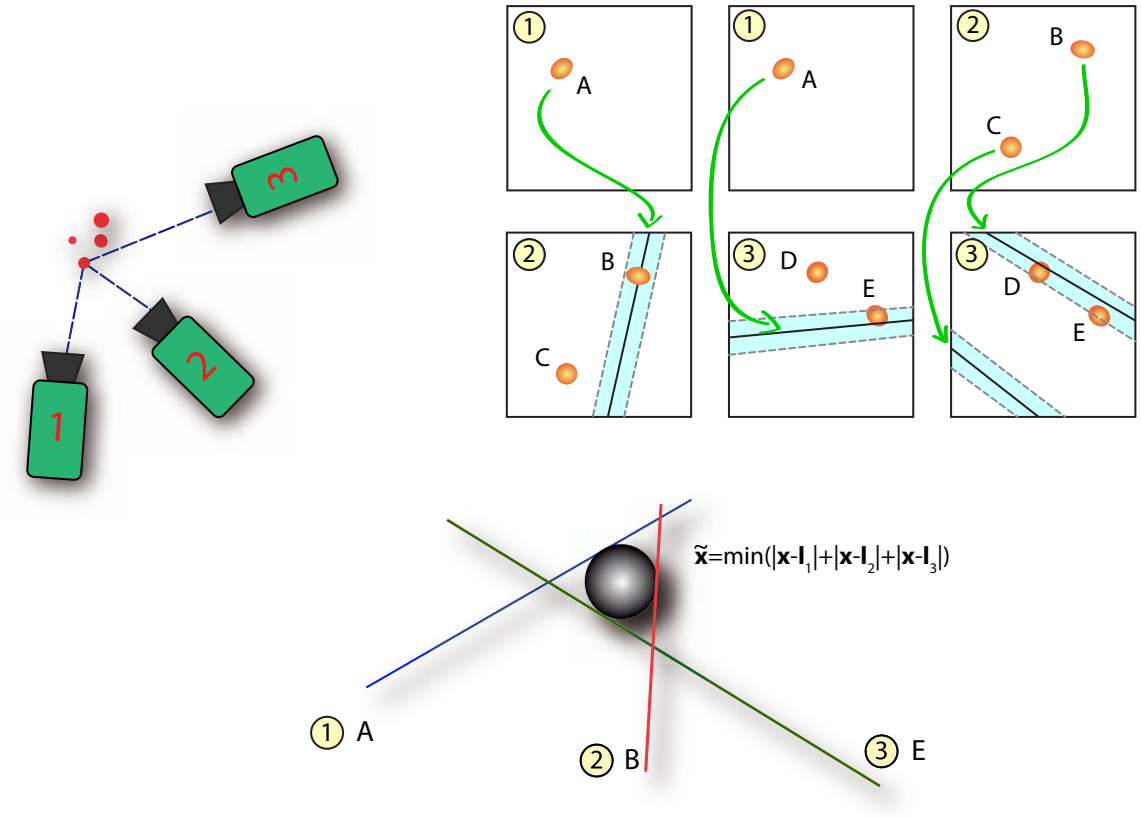

Figure IV.3: Sketch of the stereo-matching algorithm. The particles create light spots on the image planes of the three cameras, which are identi ed with a particle nding method. For each pair of image planes, one nd a spots on the rst image plane and projects its line of sight on the other image plane. Spots which are close to this line are candidates for representing a real particle. They will be added to a list containing the all spots one image plane and their corresponding candidates on the other image plane. If it is possible to nd a path through the lists with ends at the start spot, one has identi ed the spots corresponding to a particle. In this picture, the path is $1\ A \approx 2\ B \approx 3\ E \approx 1\ A$. The position of the particle, $\mathbf{x}$, is the point which has minimal distance to the lines of sight, $\mathbf{l}_1$, $\mathbf{l}_2$ and $\mathbf{l}_3$.

IV.5.6 Building the trajectories

The points in 3D space at di erent timesteps are yet not associated with each other. The connection of the points, obtained from the stereo-matching step, into a trajectory, $\mathbf{x}(t)$, in time is called tracking. In [27] , Ouellette *et al* investigated the following techniques on their accuracy. A visualization of the algorithms explained below is provided in gure IV.4.

Nearest Neighbor: Starting with a particle $\mathbf{x}(t)$ every point $\mathbf{x}(t+\ t)$ on the next frame within a maximum distance $\mathbf{x}(t)\ \ \mathbf{x}(t+\ t)\ < d_{max}$ can be considered a possible part of the trajectory. In order to detect high velocities, d_{max} has

to be large enough, and because of having several particles in the measurement volume multiple continuations of a track are usually possible. Hence, it is recommended to look several frames ahead to avoid building physically meaningless trajectories.

Minimal Acceleration – 3 Frames: Using the particle position at $t - \Delta t$ and the one at the current frame, the velocity can be calculated and the position at $\tilde{\mathbf{x}}_p(t + 1\,\Delta t)$ can be predicted. For all particles in the search volume around the estimate the acceleration can be calculated. The trajectory showing minimal acceleration is considered to be more likely to be physically correct.

Minimal Change in Acceleration – 4 Frames: The position, velocity, $\tilde{\mathbf{v}}_p$, and acceleration, $\tilde{\mathbf{a}}_p$, of the particle in frame $n + 1$ is estimated using the described "Minimal Acceleration" method (as described above) . The position in frame $n + 2$ can be estimated as $\tilde{\mathbf{x}}_p(t + 2\Delta t) = \tilde{\mathbf{x}}(t) + \tilde{\mathbf{v}}_p \cdot (2\Delta t) + \tilde{\mathbf{a}}_p \cdot (2\Delta t)$. For all points in a search region around $\tilde{\mathbf{x}}_p(t + 2\Delta t)$ the third time derivative, (i.e. change in acceleration), is calculated. The best match for the frame $n + 1$ is the particle showing the minimum change in acceleration from the prediction in frame $n + 2$.

Best Estimate – 4 Frames: Instead of the third time derivate for frame $n + 2$, the distance to the estimate $\tilde{\mathbf{x}}_p(t + 2\Delta t)$ is calculated for all points in the search volume. The best match for the frame $n + 1$ is now the particle showing minimum distance between estimate $\tilde{\mathbf{x}}_p(t + 2\Delta t)$ and points $\tilde{\mathbf{x}}_i(t + 2\Delta t)$.

At the beginning of a trajectory the *Nearest Neighbor* has to be used. Ouellette *et al* [27] showed that the *Best Estimate* produces the best results even for higher particle densities. Therefore, this method had been implemented in the particle tracking method.

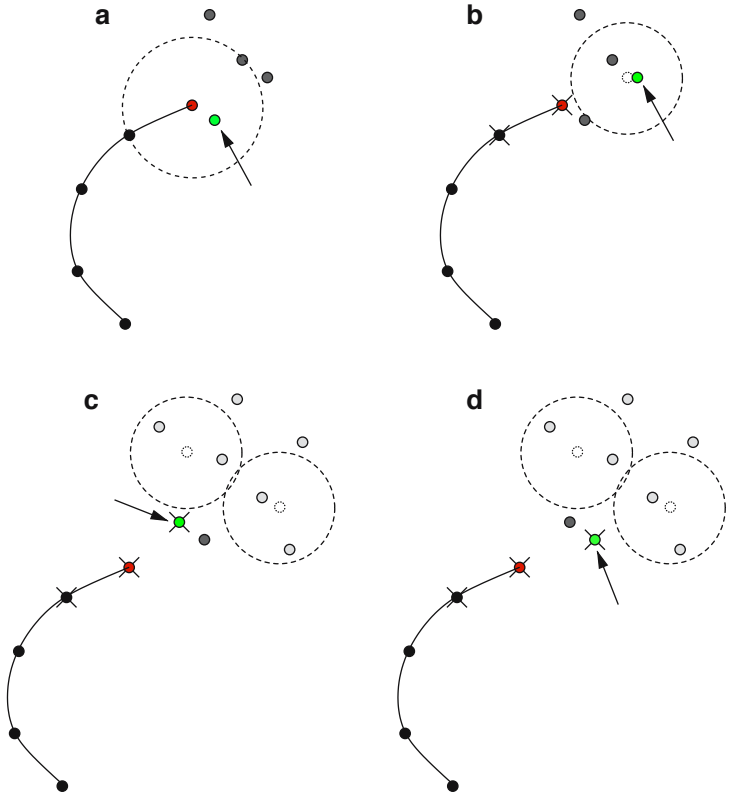

Figure IV.4: Sketch of the discussed techniques to build the trajectories. Image taken from [27]. Red dots indicate the particle position at t, and the arrows point at the green particle chosen for $t + \Delta t$. The sub figures are: *a: Nearest Neighbor* As indicated by the arrow, the particle at $t + \Delta t$ which closest to the particle at t was picked. Clearly, this method has a high risk of building physically incorrect trajectories. *b: Minimal Accleration* Using the already known particle positions at t and $t - \Delta t$ one can estimate the position in frame $t + \Delta t$. The particle closest to point will be picked. *c: Minimal Change in Accleration* By looking one frame back and one frame ahead one can estimate velocity and acceleration for all possible continuations of the track. The particle at $t + \Delta t$ for which the particle in frame $t + 2\Delta t$ shows the least change in acceleration, will be chosen. *d: Best Estimate* Instead of minimizing the change of acceleration, the particle at $t + \Delta t$ is picked which shows the best estimate for a particle in $t + 2\Delta t$. The PTV system employed in this diploma thesis uses the *Best Estimate* technique.

IV.5.7 Connection of Tracks

Fluctuations in the intensity of the illumination, and hardware (e.g. dead pixels) and software problems can cause an earlier termination of trajectories.

To avoid this H. Xu [28] developed a technique to reconnect trajectories broken into several shorter pieces using linear interpolation in a six dimensional position velocity space. The algorithm is explained in gure IV.5. The reconnected trajectories are much longer in duration, thus providing much better Lagrangian statistics. However, the interpolated points themselves can not be used since they would introduce an arti cial bias to the statistics.

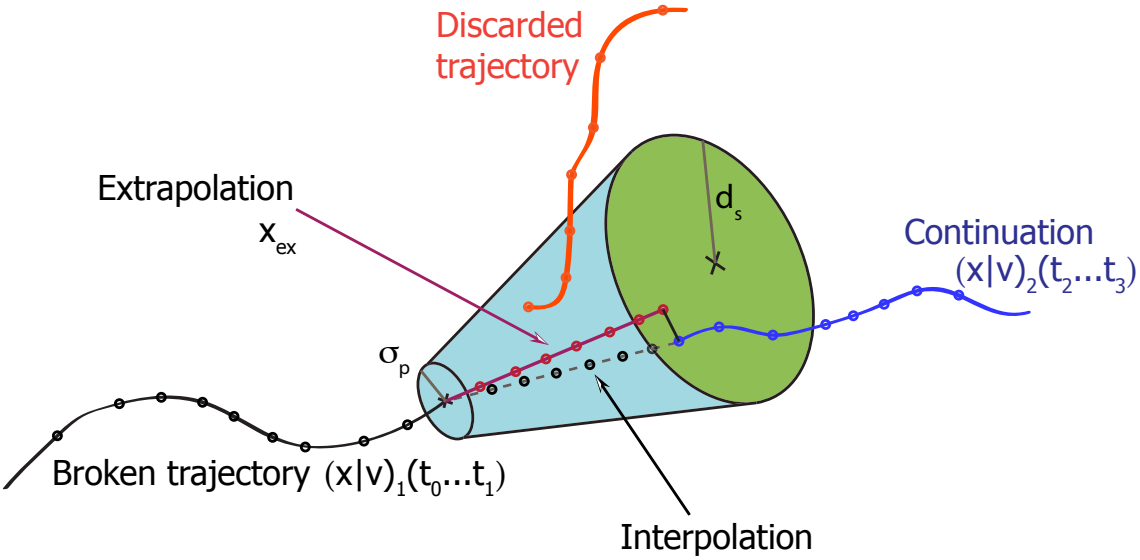

Figure IV.5: The broken trajectory $(\mathbf{x}\ \mathbf{v})_1(t)$ is extrapolated from its end, t_1, up to temporal search distance, t_{max}, along its last known velocity vector. Trajectory starts at time t_2, found within a spatial search distance $d(t) = \phi_p + t\ \ t_{max}\, d_s$ to the extrapolation, are possible candidates for a continuation of the track. ϕ_p is the uncertainty in postion measurement and d_s is user set maximum. The search area can be imagined as a truncated cone. Nevertheless, the cone is situated in four-dimensional time-position space. For each candidate an extrapolation $\mathbf{x}_{ex}(t_2) = \mathbf{x}_1(t_1) + (t_2 \quad t_1)\,\frac{\mathbf{v}_1(t_1)+\mathbf{v}_2(t_2)}{2}$ and its distance to the candidate are calculated. The trajectory showing the least distance is picked as the continuation. The unknown points between $\mathbf{x}_1(t_1)$ and $\mathbf{x}_2(t_2)$ are created through a linear interpolation. For the linear interpolation the direct connection between $x_1(t_1)$ and $x_2(t_2)$ is established. To avoid a bias of the data, these arti cial points are marked as interpolated.

V Experimental Setup

V.1 The Lagrangian Exploration Module

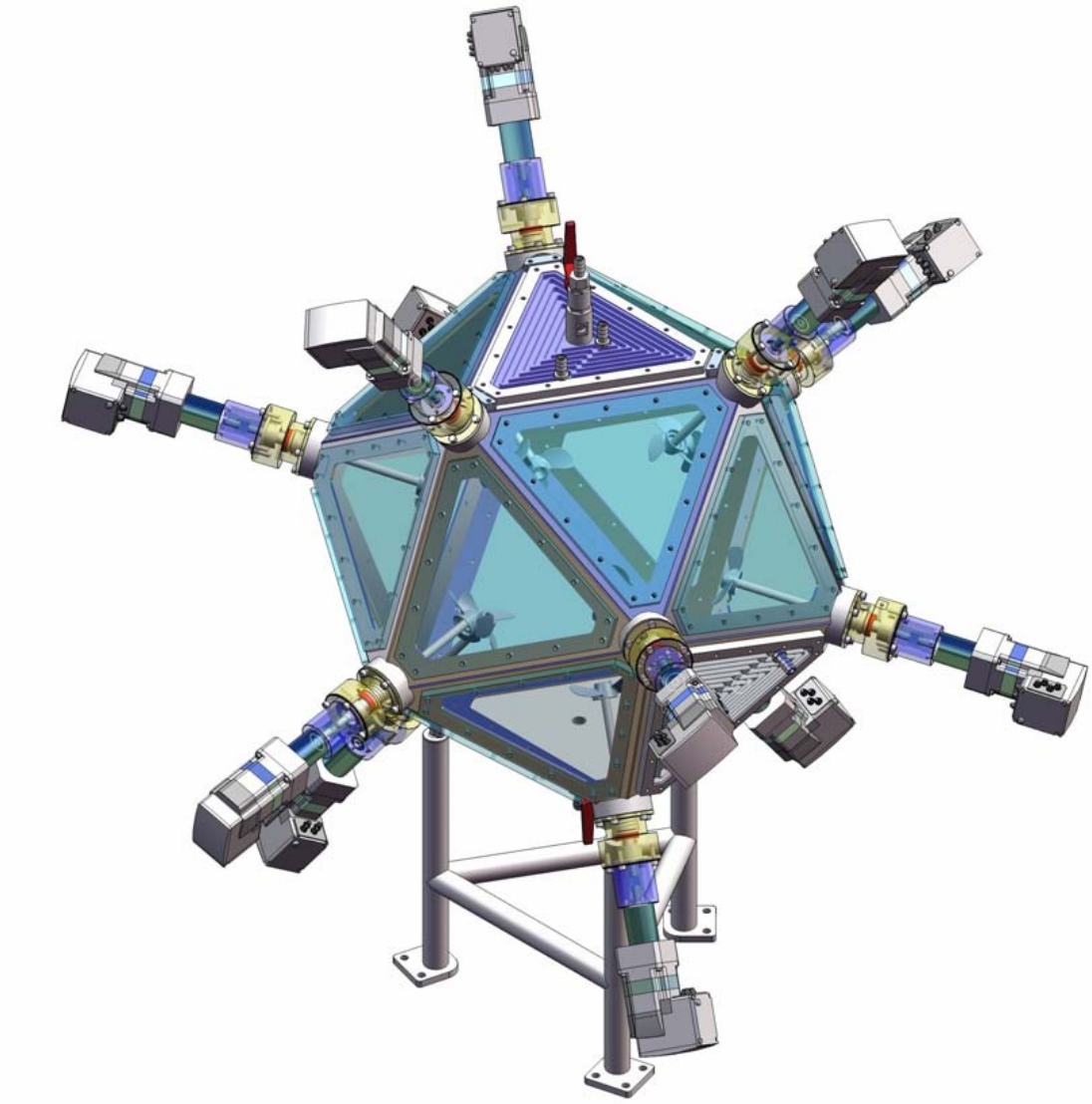

Figure V.1: CAD drawing of the LEM

V.1.1 Basic structure

The Lagrangian Exploration Module (LEM) has a skeletal structure made of stainless steel in the shape of an icosahedron. The edge s length is $40cm$ leading to a total volume of 140 liters. On each face either a plexiglas window or a cooling plate can be mounted. To avoid corrosion, all parts that are in contact with water, are made either of plastic or stainless steel. The top and the bottom plate are two cooling plates which have an additional hose attached to them, so that the tank can be lled with, or emptied of, the working uid. On each of the 12 vertexes a propeller unit is mounted.

15 M6 screws per face are used to mount windows and cooling plates. Each screw is screwed in from the inside of the tank with a Nylon washer between the screw head and the LEM skeleton. From the outside, standard stainless steel nuts and washers are used to x the plate. Additionally, an o-ring is placed along the edge between the triangular window or cooling plate and the LEM structure to avoid leakage. Screw glue is added to help seal o the screw threads. Applying high vacuum grease to the o-ring also proved to be an e ective way to prevent leakages.

V.1.2 Propeller unit

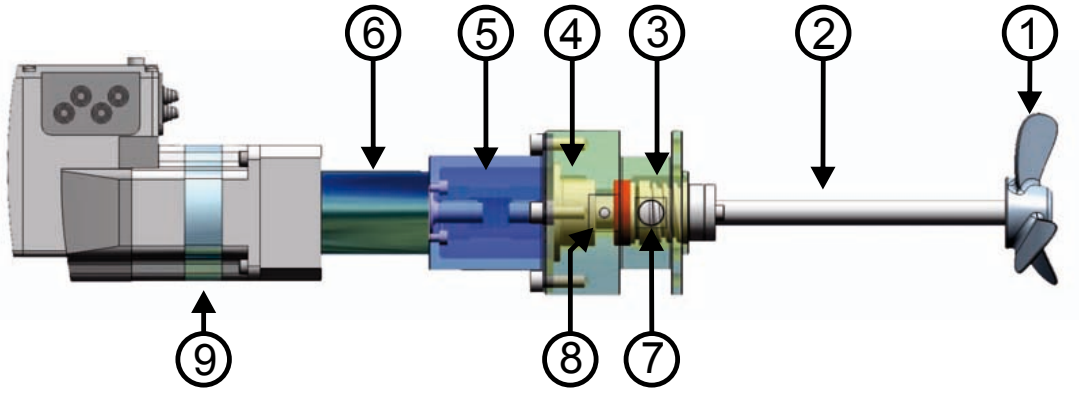

Figure V.2: CAD drawing of the propeller unit; *1*: propeller, *2*: exchangeable propeller shaft, *3*: rotating seal, *4*: bearing, *5*: shaft coupling, *6*: gearbox, *7*: threaded hole connecting the propeller unit to the bubble trap, *8*: hole allowing water vapor produced by the seal to leave the housing, *9*: brushless DC motor

A propeller unit (PU) is mounted to each vortex. Figure V.2 shows a CAD drawing of the propeller unit. Both propeller and propeller shaft can be replaced, allowing di erent propellers to be tested at di erent distances into the tank. The inner part of the shaft is held by a standard double-row ball bearing. Sealing is achieved with a rotating seal (Pac Seal). The propeller is driven by a brushless DC-motor (IFE71, Berger-Lahr) whose speed is reduced by a $5:1$ planetary gear box. The gearbox and inner shaft are connected by a stainless steel exible coupling. A threaded hole in front of the rotating seal makes it possible to connect a hose to

the propeller unit, which can be used for particle insertion or bubble removal. A second hole drilled on the other side of the seal allows water vapor produced by the rotating seal to leave the housing.

Motors

Each of the 12 motors is supplied with a constant voltage of 36 V and connected to a CANbus. A maximum power of 120 W can be conferred to the flow. The power is provided by two adjustable 1.5 kW power supplies (N5766A, Agilent). It is possible to read out the actual voltage and current of both power supplies via ethernet.

Via CANopen commands sent over the CANbus, speed and acceleration can be set (and changed during runtime) for each individual motor. The maximum speed is ± 5000 rpm (resp. $16\frac{2}{3}$ Hz after the $5:1$ gear box) and the minimum speed, apart from 0 rpm, is ± 300 rpm (1 Hz after gear box). The acceleration can be set between 1000 rpm/s and 10000 rpm/s. If prompted, a motor will return its actual status, displaying for example its temperature, speed and current.

A PC with a CAN-USB adapter (PCAN-USB, isolated – Peak Systems GmbH) is used to control the motors. The software is written in Delphi providing an automatic and a manual mode. In the automatic mode a text file, specifying the speed and rotation sense for each individual motor at different times, is interpreted by the program.

Propellers

In a first attempt, we used round anodized aluminum disks of 10 cm diameter cut in at every 60 degrees, where the corners were bent in (see figure V.3). As the first trial produced a highly rotating flow with little pushing (measured by hand), we bent the vanes some more until they stood out at an angle of about 30 degrees. The result was satisfactory. It should be noted that the propellers were bent by hand, so that each of them produces a slightly different flow.

Figure V.3: figure on the left: propeller made out of anodized aluminum, the diameter is 10 cm;
figure in the middle: a propeller after 1 week in saline water (15 g marine salt per liter) – the dent has a depth of ≈ 2 mm
figure on the right: stainless steel propeller of the same size and shape

Although anodized, the propellers were still subject to corrosion in salt water (see figure V.3). Consequently, they were replaced by stainless steel propellers of the same size and approximately the same shape. In order to test the influence of different propeller sizes on the flow we further designed a four-vane plastic propeller with exchangeable vanes.

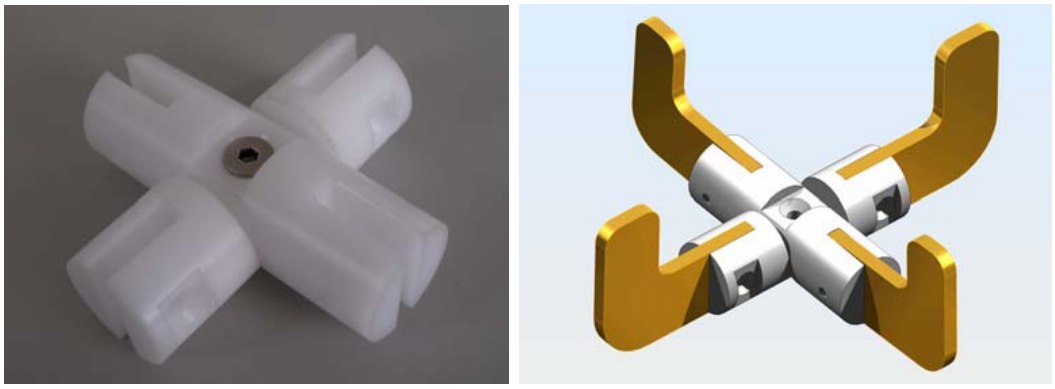

Figure V.4: plastic propeller: up to 4 vanes of different sizes can be mounted

V.1.3 Particle insertion & bubble removal

The removal of bubbles and insertion of particles is done by the same device – the bubble trap which is shown in figure V.5. For that purpose all downward pointing propeller units (PU) are connected to the upper inlet of a container – a modified filter housing (Thermo Fisher Scientific). The lower outlet in return is linked to the upward pointing PUs through a pump. The content of the container is pumped through the six upward pointing PUs into the LEM. Hence, the fluid and bubbles which are trapped in these PUs are transported back into the container. There, air bubbles can escape due to their buoyancy. On the other hand, new particles inserted into the container, will be pumped into the LEM.

It is possible to connect the container to a vacuum pump to lower the pressure in the tank. In this case, it is necessary to bypass the pump using the three valves shown in figure V.5. Assuming a horizontal throw of water out of the inlet of the container a flow rate through the pump of about $1\frac{l}{min}$ was calculated.

V.1.4 Filtering & plumbing

We are using two filter housings with a 10 μm and a 5 μm filter. Both were bought at Thermo Fisher Scientific. A garden pump from the local Bahr Baumarkt is used to pump water from the connector at the base plate of the LEM through the coarse and the fine filter and back into the LEM through the top plate.

The connectors, plugs, distributors and valves integrated into the water system were manufactured by Gardena. The standard hose also belonging to the water system has a diameter of half an inch.

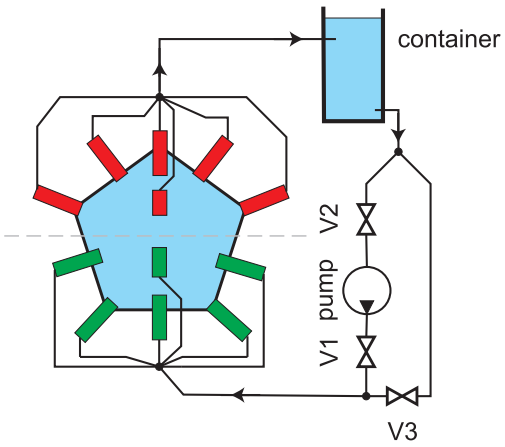

Figure V.5: Particle insertion and bubble removing: particles inserted into the container will be pumped into the LEM through the six lower propeller units (green); on the other hand, bubbles which get trapped in one of the six upper propeller units (red) are pumped into the container, where they leave the system due to their buoyancy; the 3 valves (V1, V2 &V3) allow the bypass of the pump, which is required for depressurization of the tank.

V.1.5 Temperature control

Without the cooling system heat would be a major problem of the LEM. Since the motors are connected to body of the LEM without any insulator in between, electronic and mechanical heat will raise the temperature of the fluid. For example, 2 kW will increase the temperature of 140 l of water by 12 K in one hour. To control the temperature in the tank, we glued a PT100[1] resistor to each of the top and bottom plates with silicone. As shown in figure V.7 both are separated by $\approx 4mm$ thick layer of silicone from the metal surface. The bias introduced by attaching the sensors to the cooling plates is surpassed by the errors of the temperature measuring system, and therefore negligible.

With the help of the circuit shown in figure V.8, the resistance of the PT100 is converted into a voltage signal. The circuit was adjusted and calibrated such that a range between 0 $°C$ and 50 $°C$ can be covered. The result is passed to a 10-bit analogue-digital converter of a micro-controller (C-Control 2, Conrad). If the moving average of the temperature over 2 seconds is higher than a user-set value, it opens a magnetic valve to flush the cooling plates with cooling water. The accuracy is 0.4 K due to the internal noise of the AD–converter of the micro-controller. Using a micro-controller with less internal noise of the AD conversion will yield better control of the fluid temperature.

[1] A PT100 is thin platinum resistor with a resistance of 100 Ω at 0 $°C$ and a linear temperature dependence of their resistance within 0 and 100 $°C$

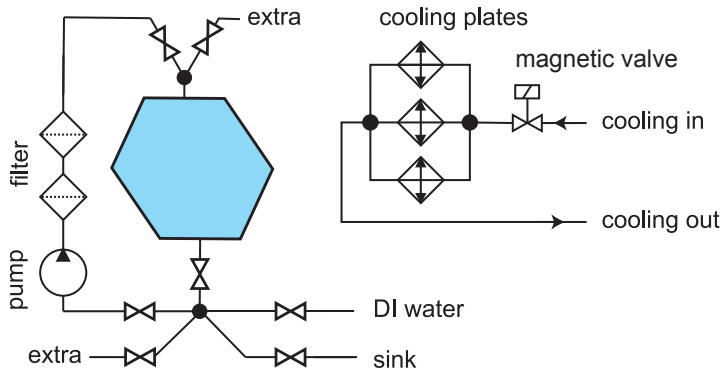

Figure V.6: Left side: schematic of the plumbing system used to fill and filter the tank: the LEM is filled with deionized water; through an extra inlet at the top and an extra outlet at the bottom samples can be taken or bigger amounts of chemicals can be administered to the tank; a pump can transfer the tank content through a 5 μm and a 10 μm filter to remove particles and dirt;
right side: schematic of the cooling system: in opening the magnetic valve the cooling water can run through the cooling plates mounted to the LEM; the micro-controller described in section V.1.5 opens the valve after comparing the measured temperature to a user-specified threshold.

Figure V.7: The PT100 sensor glued to a cooling plate; the wire is passed trough a former water outlet.

V.1.6 PTV setup

The Particle Tracking Velocimetry system consists of 3 cameras, a laser, a control–PC and a cluster of several node computers, where the particle tracking program runs.

Figure V.9 shows a sketch of the wiring for the PTV system. Three Phantom V7.2 high speed cameras from Vision Research take 8-bit grayscale movies at frame rates up to 11.000 fps at a resolution of 512×512 pixels. The control and download of the movies is done via ethernet. A frequency generator creates a square wave, which is passed to a frequency divider. There, the frequency is adjusted to the frame rate

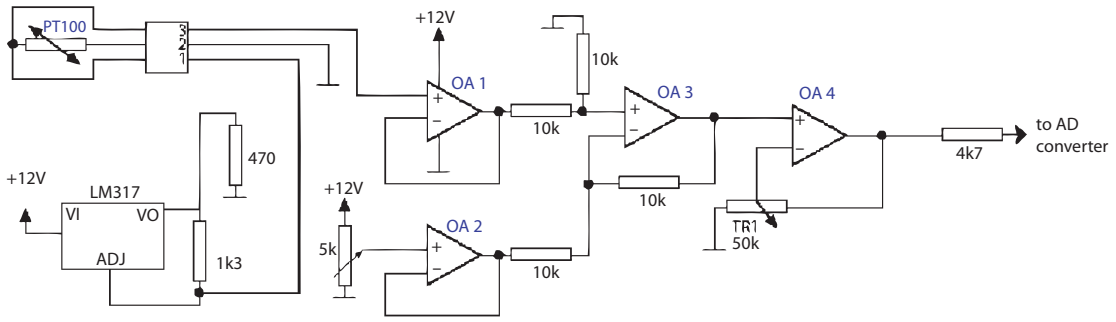

Figure V.8: Represented is the circuit converting the resistance of a PT100 to a voltage signal readable by an AD converter:
IC LM317 creates a constant current through the PT100; the voltage drop over PT100 is amplified 1 : 1 with an operational amplifier (OA) 1 to reduce noise; a stable offset voltage is created at OA 2; OA 3 subtracts the signal of OA 2 from OA 1 which corresponds to the subtraction of an offset temperature (a PT100 already has a resistance of 100 Ω at 0° C); in the last step OA 4 amplifies the input such that the maximum signal to be expected corresponds to the maximum input voltage of the AD converter.

of the three cameras. Then it is passed as a synchronization signal to the latter. A part of the unreduced output from the frequency generator is also passed to a delay unit. The delayed signal is then passed to the Q-switch of the laser. The cameras need a few micro seconds to prepare the electronics before a picture can be taken. Delaying the laser pulse allows the efficient capture of laser pulses for one frame. A small reed relay driven by the parallel port allows both to switch on or off the laser and to externally trigger the cameras. All cameras, the PC and the cluster are connected to a Gigabit ethernet switch.

Setting frame rate, resolution and other properties is done with a program (named `QTalkCam`) running on the control–PC. For the simultaneous recording of three movies, the same program switches on the laser via the relay and starts the recording (albeit at slightly different times) for each camera. Due to initial instabilities of the laser, heat up procedures, etc, the recording goes over a longer period than necessary for the specified amount of frames. The recording is stopped synchronously by switching off the laser. After terminating the recording process only a specified amount of the last frames is downloaded:

A server program (called `ph7server5`) running on the cluster is waiting to download the movies using the second network interface of the cameras. If the recording was successful, the control program `QTalkCam` transfers IPs, basic camera properties, the number of frames to download and a black–reference from each camera to the server program, which starts the simultaneous download of the movies. Once the download of all three movies has finished, `ph7server5` signals to the control program that the next movie set can be started. A third program called `controller_node` processes available movie sets according to the PTV algorithm described in sec-

tion IV.5 with user specified thresholds. The original movies are usually deleted after computing and storing the trajectory files.

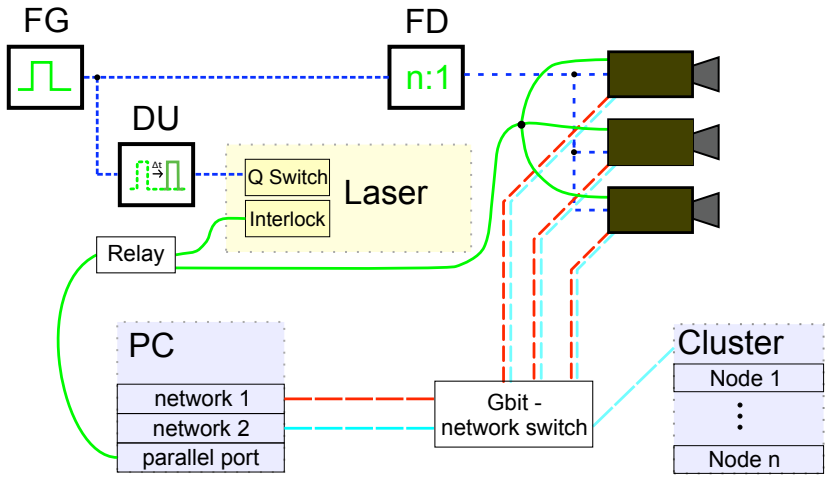

Figure V.9: Schematic wiring of the PTV system: The frequency generator (FG) generates a square wave (blue) with frequency $> 10kHz$, the signal is passed to a frequency divider (FD) and divided such that the new frequency corresponds to the frame rate of the cameras, the divided signal is the synchronization signal for the cameras; a delay unit(DU) delays the frequency such that laser pulses occur only after camera electronics are prepared; cameras are controlled via a PC (red), whereas movie downloading and particle tracking is done on a cluster connected to a second ethernet card on the cameras (cyan); operating the laser and triggering the cameras is done via a parallel port driven relay

Camera mounting

The challenge for developing a camera mounting system was to find a design compatible with the non-perpendicular angles between the faces of the LEM. The system was required to be easily adjustable, yet rigid enough to enable particle tracking velocimetry without additional position errors. We settled for Linos X95 profiles, and mounted them with adaptor plates on a platform. The platform consists of two 600 $mm \times 450$ mm aluminum plates with a M6-threaded 25 mm hole pattern from Thorlabs mounted on a frame built out of 45 mm aluminum profiles (FM-Systeme).

The cameras are attached to the Linos profiles with the help adaptors built by our machine shop. The camera mounts for the two side-cameras were constructed in such a way that a rotation will not affect the position of the CMOS-chip. Figure V.10 shows the camera mount for the top camera. The design enables the camera to be both tilted and moved in a range of about 3 cm in the direction towards the LEM.

Figure V.11 shows two pictures of the camera arrangement. After calibration, the camera position is fixed. Any unintentional movement can be registered by a Matlab code written by Haitao Xu. This program measures the shift and rotation of the

image plane with respect to its original position during calibration. It was observed that the shift after a few weeks was less than a pixel. No rotation of the image plane could be measured. Therefore, the structure has proven its stability.

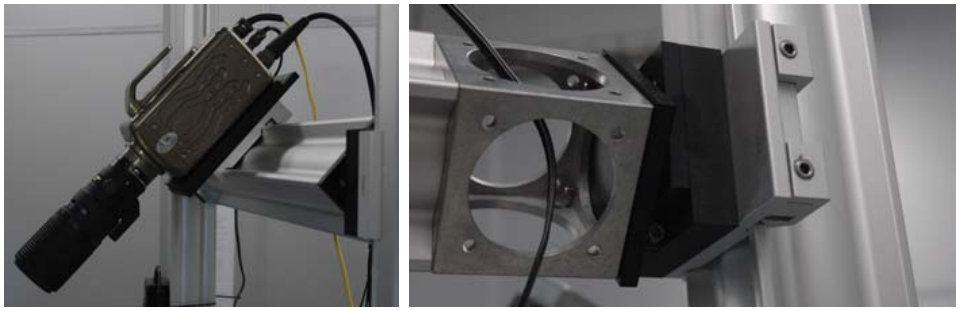

Figure V.10: Camera mounts for the top camera:
figure on the left:height and position in y-direction can be changed with the Linos carriers; the figure on the right: the piece which allows tilting of the camera.

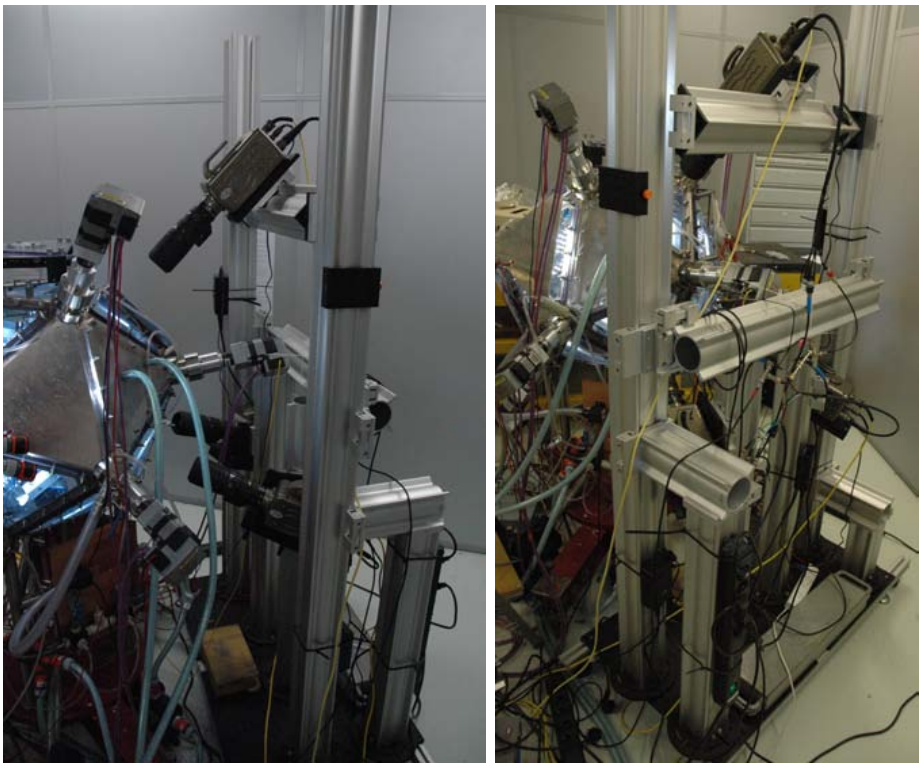

Figure V.11: figure on the left: side view from the construction holding the cameras; figure on the right: backside view from the structure on which the cameras are mounted.

Light

Light is provided by a frequency doubled Nd-YAG laser (DDC technologies) with a high pulse rate. Its power during the experiments was approximately 30 W at pulse rates between 10 kHz and 30 kHz. Each camera frame captured several laser pulses. The beam was expanded via a convex and a concave lens mounted on a tilted Linos X95 profile. The whole system was aligned in a way that the beam enters the LEM perpendicular to a face and passes through the center of the volume. For security reasons the face on the opposite side has to be blocked. Therefore, we mounted an additional cooling plate onto this site.

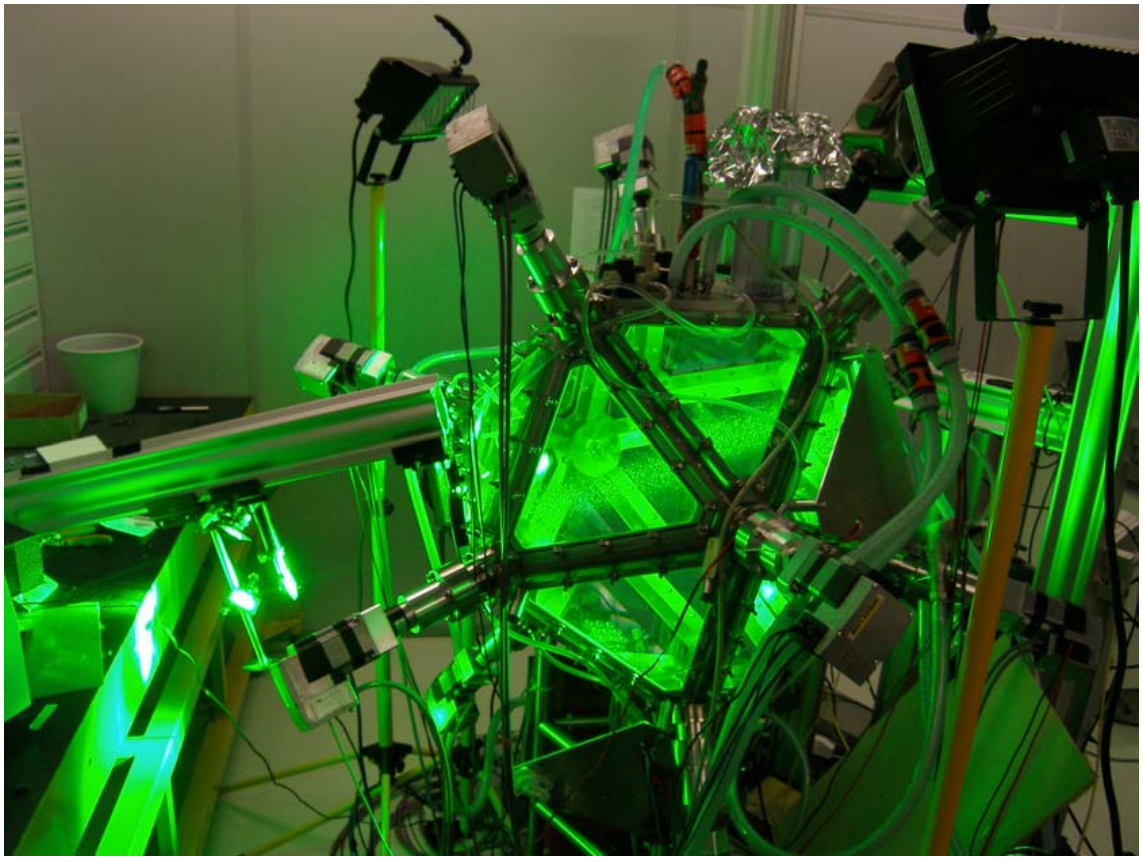

Figure V.12: The expanded laser beam illuminating the LEM; a 400 mm convex lens is sitting close to the window, the two optical components at the left are mirrors

Initially, 12 high power LEDs (Ostar HEX-6, $\approx$ 1000 lm of white light, Osram) and 18 less powerful LEDs (Osram) were added to the setup to increase the amount of light in the measurement volume. However, the attempt was abandoned, since a lot more LEDs would be needed to register a significant improvement in the total light available.

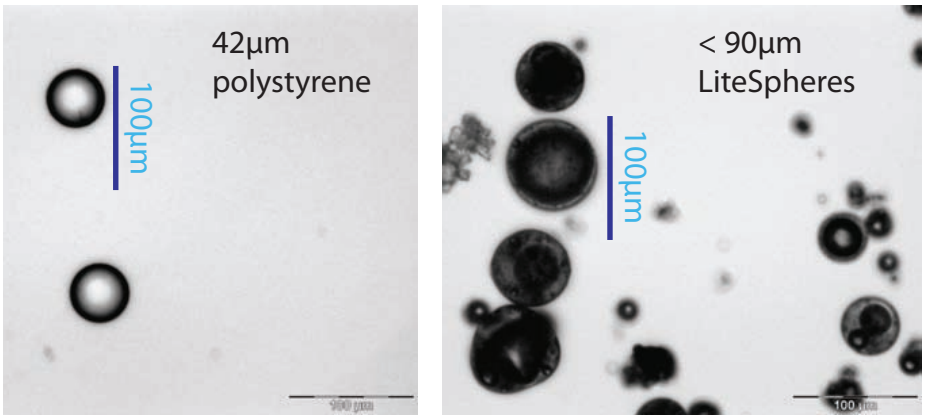

Figure V.13: Used particles seen under a microscope. We found both particle types to be neutrally buoyant in water.

Particles

In order to use PTV, particles need to be added to the flow. The particles, however, should not disturb the flow or bias the measurement. To ensure this, the following properties have to be considered beforehand:

- the amount of light scattered by a particle
- the buoyancy of the particles (= their density compared to the density of the surrounding fluid)
- the shape of the particle
- the response time to forces acting on the particle by the flow
- chemical properties
- price and availability

The time scale, τ_p, in which the particle reacts to changes in the flow, can be expressed in terms of the Stokes number:

$$St \equiv \frac{\tau_p}{\tau_\eta} \tag{V.1}$$

where τ_η is the smallest time scale of a turbulent flow (see section III.6).

In order to estimate τ_p, one can picture a sphere falling through a fluid. From experiments it is known that such a sphere will also move some of the surrounding fluid. In other words, the mass of the sphere is increased. For low Reynolds numbers the particle is decelerated by the viscous Stokes drag force and accelerated by gravitation:

$$St = \frac{\rho_p + \frac{1}{2}\rho_f}{\rho_f} \frac{d^2}{18\,\nu} \frac{1}{\tau_\eta} = \frac{1}{18} \frac{\rho_p + \frac{1}{2}\rho_f}{\rho_f} \left(\frac{d}{\eta}\right)^2 \tag{V.2}$$

where ρ_p and ρ_f are the densities of the particle and the fluid respectively, and d is the diameter of the particle.

For $St \ll 1$, the particles react quickly. According to equation (V.2) the ideal particle would have a density $\rho_p < \rho_f$ and a size $r < \eta$. However, in our experiments it is better to match particle and fluid density to avoid buoyancy forces, and thus a preferred direction of motion for the particles[2]. Apart from that, the intensity of the scattered light depends on the diameter squared. A compromise has to be found between fast reaction time and sufficiently high scattered intensities. In our case, the particles should be passive tracers of the flow.

Two different particles were chosen for the experiments: sieved hollow glass spheres (*LiteSphere*, MO-SCI cooperation) with diameters up to $90\mu m$ and 42 μm polystyrene particles (Duke Scientific). Images of the particles are provided in figure V.13 and a long exposure picture of illuminated particles in a turbulent flow is depicted in figure V.14.

The density of the $42\mu m$ particles is specified by the manufacturer as $1.06\frac{g}{cm^3}$. MO-SCI did not specify the density of the *LiteSpheres* particles. Because we found both particles to be neutrally buoyant in water, we assume both particle types to have the same density. Although, the LiteSphere particles are polydisperse, the PTV system can only detect particles with a diameter $\gtrsim 60\mu m$. Smaller spheres scatter an insufficient amount of light and are thus not detectable. The maximum diameter of 90 μm was used to compute the Stokes number, St.

The used Stokes numbers are shown in table VII.1.

Calibration

For the calibration of the PTV system we exchange the top plate of the LEM (as shown in figure V.17) with the special calibration stage depicted in figure V.16. One or two linear stages can be mounted on the plexiglas plate. The whole system can be rotated, and the height of the mask can be adjusted. We built adaptor pieces to raise and fix the stage.

The masks employed were regular dot patterns with three bigger dots defining the center. They were created with Adobe Illustrator and printed on transparency foils. The foil in turn was either "glued" on to a glass plate[3] with either glycerol, or for smaller areas, high vacuum grease. The inclosure of small air bubbles must be avoided as they would cause additional reflections that distort the calibration images. Water entering the gap between glass surface and foil and thus changing the distance between the two must also be avoided.

Two masks with different dot spacings and sizes were used. One mask had a spacing between dots of 10 mm and 3 mm dot size, for the other mask the spacing was set to 2.5 mm and the dot size to 0.9 mm. Background illumination with a diffusive light source[4] resulted in the best image quality.

[2] It should be noted that the clustering of particles is related to the Stokes number and the densities ρ_p and ρ_f.

[3] trials with two-component glue or silicon failed

[4] For instance, a sheet of paper and a halogen bulb

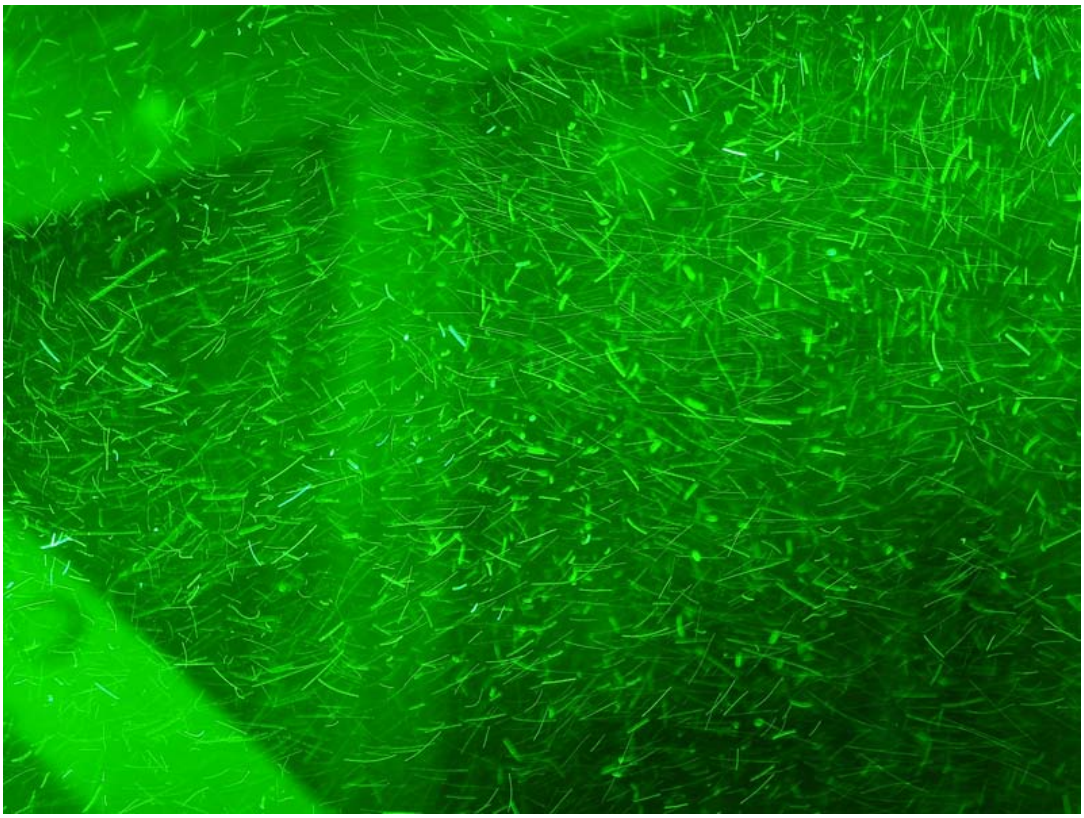

Figure V.14: A long exposure picture of LiteSphere particles (diameter $< 90\ \mu m$) in a medium turbulent flow

For calibration, a mask was moved along one axis within the tank, and short movies of approximately ten frames were recorded for each position of the mask. Figure V.15 provides a simple sketch of this setup. The axis along which the calibration mask is moved, is defined as the x-axis in the experiments. We set $x = 0$ as the center of the LEM.

A Matlab code written by Haitao Xu allows the identification of the dots in the calibration images. Using the three center dots, knowing the dot spacing of the mask, and the position of the mask in the $x-$direction, one can connect a set of 3D points with their projection on the CMOS chip of a camera. The parameters, which relate the picture on the image plane to the 3D lab system (see section IV.5.2), can be obtained using the method described in IV.5.3.

Relaxations of the holding structure would shift the cameras and thus the location of the image planes. For small perturbations it is sufficient to realign the image planes before the stereo matching step. A Matlab code (written by Haitao Xu) is used to obtain the average shift and rotation of each CMOS sensor from a PTV experiment. Before carrying out the real measurements the calibration was refined by storing shift and rotation in the configuration file. Hence a smaller position error was achieved.

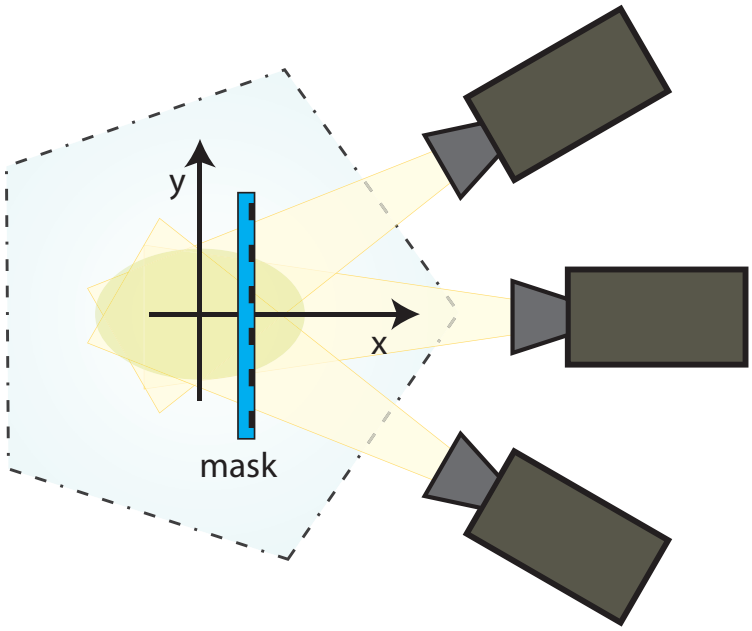

Figure V.15: Schematic top view of the camera arrangement. The three cameras are orientated at di erent angles inside the apparatus, such that they focus on the center of the tank. If the cameras are not arranged perpendicular to each other, the observable region is a stretched sphere as indicated by the ellipse in the drawing.

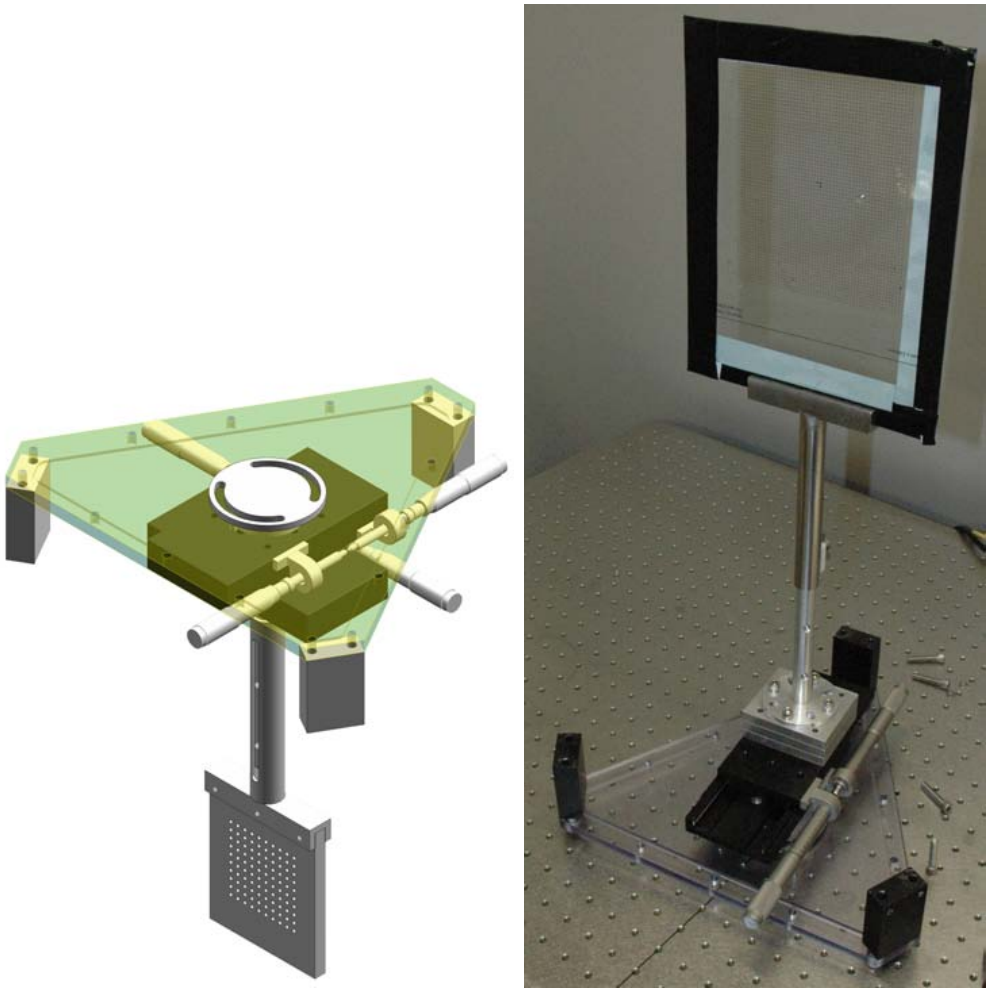

Figure V.16: figure on the left: CAD drawing of the calibration stage with two linear stages;figure on the right: assembled calibration stage before mounting in the LEM.

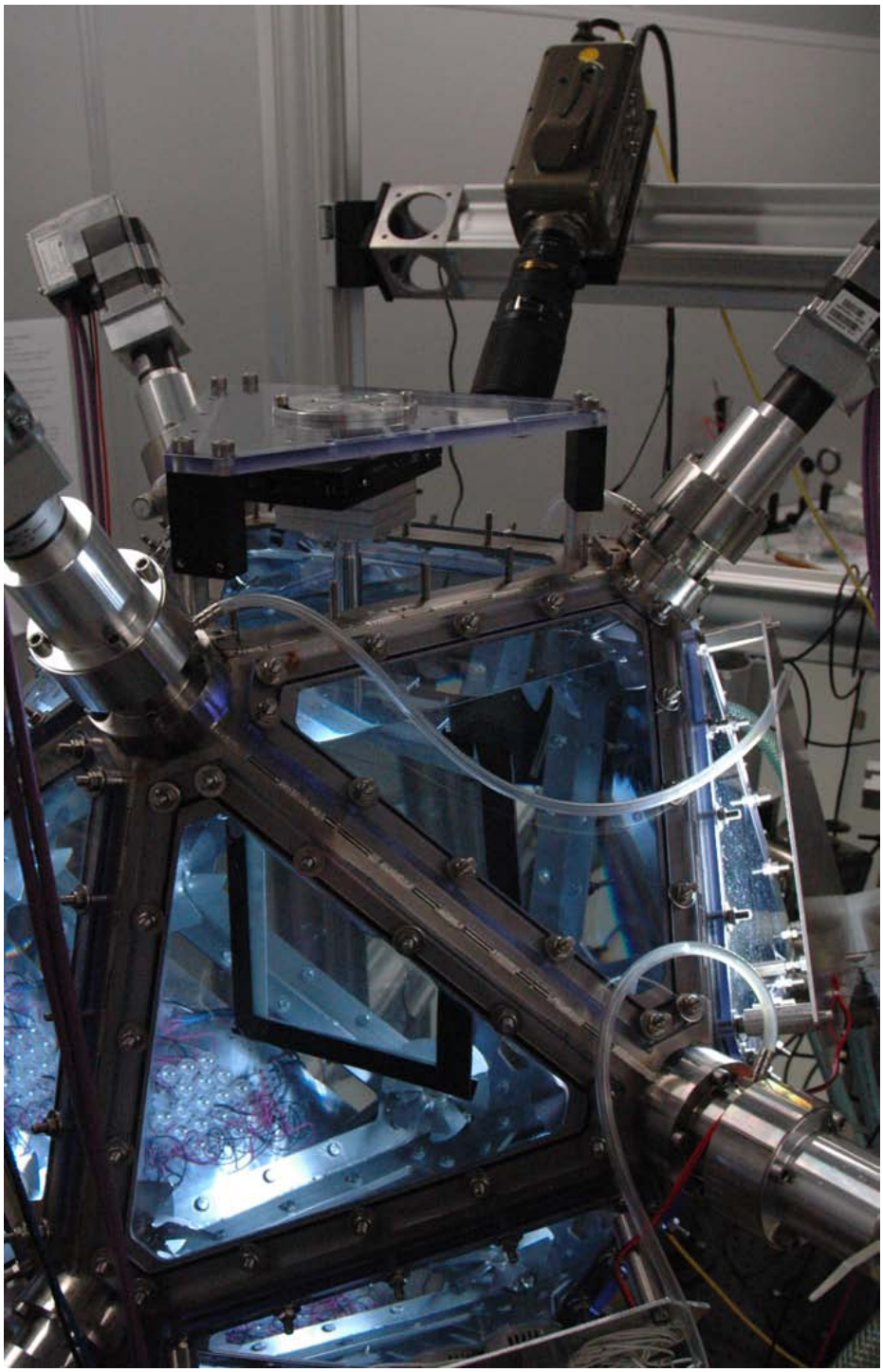

Figure V.17: The calibration stage mounted onto the LEM, note the three aluminum adaptor pieces needed to fix the calibration stage, illumination of the mask can be provided by the LED plates or halogen bulbs

VI Analysis of the Trajectories

VI.1 Calculation of Velocity and Acceleration

Using the PTV technique described in section IV.5 and V.1.6 we get a series of particle trajectories[1].

A trajectory can be represented as the position, $\mathbf{x}(t)$, of a particle at each frame t. The length of a trajectory can range from several ten to a few thousand frames. Noise and measurement errors $\xi(t)$ bias the measured position. The measured position, $\tilde{\mathbf{x}}(t)$, is then

$$\tilde{\mathbf{x}}(t) = \mathbf{x}(t) + \xi(t) \tag{VI.1}$$

Both the velocity, $\mathbf{u}$, and the acceleration, $\mathbf{a}$, are needed to calculate structure functions, correlation functions and other measures. To calculate the velocity $\mathbf{v}(t)$ using the discrete difference between $\tilde{\mathbf{x}}(t)$ and a time Δt later

$$\tilde{\mathbf{u}}(t) = \frac{\tilde{\mathbf{x}}(t+\Delta t) - \tilde{\mathbf{x}}(t)}{\Delta t} = \mathbf{u}(t) + \frac{\xi(t+\Delta t) - \xi(t)}{\Delta t} \tag{VI.2}$$

is sensitive to noise. Consequently, the second derivative is even more sensitive to noise and measurement errors.

To overcome this issue, one can use a convolution (see Mordant *et al* [29]) of the original data, $\tilde{\mathbf{x}}(t)$, with some kernel function, $k(\tau)$, which smoothes the original data. Such a convolution is defined as:

$$k \otimes \tilde{\mathbf{x}}\Big|_t = \int_{-\infty}^{\infty} k(\tau) \cdot \tilde{\mathbf{x}}(\tau + t)\, d\tau \tag{VI.3}$$

In the case of filtering k obeys $k \otimes 1 = 1$ and $k \geq 0$. A useful rule for convolution is that the derivative of a convolution equals the derivative of its parts, i.e.

$$(k \otimes \tilde{\mathbf{x}})' = k' \otimes \tilde{\mathbf{x}} = k \otimes \tilde{\mathbf{x}}' \tag{VI.4}$$

A Gaussian[2] kernel in the form $k(\tau) = \frac{1}{\sqrt{\pi}\omega} \exp -\frac{\tau^2}{\omega^2}$ smoothes data effectively, and combined with rule VI.4 it becomes a powerful tool to evaluating derivatives of noisy data. The velocity is then:

$$\begin{aligned} k \otimes \tilde{\mathbf{u}}\Big|_t = k' \otimes \tilde{\mathbf{x}}\Big|_t &= \int_{-\infty}^{\infty} k_v(\tau) \cdot \tilde{\mathbf{x}}(\tau + t) d\tau \\ \text{with} \quad k_v &= \frac{\partial k(\tau)}{\partial \tau} = -\frac{2\tau}{\sqrt{\pi}\omega^3} \exp\left(-\frac{\tau^2}{\omega^2}\right) \end{aligned} \tag{VI.5}$$

[1] These are stored in several hundred to a few thousand trajectory files.

[2] It is $\omega = \sqrt{2}\,\sigma$.

and the acceleration can be computed using

$$\begin{aligned} k \otimes \tilde{\mathbf{a}}\Big|_t = k'' \otimes \tilde{\mathbf{x}}\Big|_t &= \int_{-\infty}^{\infty} k_a(\tau) \cdot \tilde{\mathbf{x}}(\tau + t) d\tau \\ \text{with} \quad k_a &= \frac{\partial^2 k(\tau)}{\partial \tau^2} = \frac{2}{\sqrt{\pi}\omega^3} \left(\frac{2\tau^2}{\omega^2} - 1 \right) \exp\left(-\frac{\tau^2}{\omega^2} \right) \end{aligned} \tag{VI.6}$$

Since k is known at the beginning, one can precalculate the new kernels k_v and k_a. Furthermore, we can limit the integral to the range $[-T; T]$ since the contribution of values decays with $\exp(-\tau^2)$. Because we have discrete values and not a continuous function, the integral is evaluated as a sum. To calculate the velocity and acceleration at time t, for example, we need to evaluate $\sum_{-T}^{+T} k_v \cdot \tilde{\mathbf{x}}(\tau + t)$ and $\sum_{-T}^{+T} k_a \cdot \tilde{\mathbf{x}}(\tau + t)$. This operation is constant in time and can be done easily by a computer. But, since we are truncating the integral, we have to normalize the kernel functions. The discrete functions are

$$k_v(\tau) = A_v \tau \exp\left(-\frac{\tau^2}{\omega^2} \right) + B_v \quad \text{and} \quad k_a(\tau) = A_a \exp\left(-\frac{\tau^2}{\omega^2} \right) \left[\frac{2\tau^2}{\omega^2} - 1 \right] + B_a$$

The parameters A_v, B_v, A_a and B_a can be determined using the known derivatives

$$k_v \otimes 1 = 0 \qquad k_v \otimes \tau = 1 \tag{VI.7}$$

$$k_a \otimes 1 = 0 \qquad k_a \otimes \tau^2 = 2 \tag{VI.8}$$

VI.1.1 Calculating A_v and B_v

$$\begin{aligned} 1 = \sum_{-T}^{T} k_v(\tau) \cdot (\tau) &= \sum_{-T}^{T} \left(A_v \tau \exp\left(-\frac{\tau^2}{\omega^2} \right) + B_v \right) \cdot \tau \\ &= A_v \sum_{-T}^{T} \tau^2 \exp\left(-\frac{\tau^2}{\omega^2} \right) \end{aligned} \tag{VI.9}$$

$$\Leftrightarrow \quad A_v = \frac{1}{\sum_{-T}^{T} \tau^2 \exp\left(-\frac{\tau^2}{\omega^2} \right)}$$

$$\begin{aligned} 0 = \sum_{-T}^{T} k_v(\tau) &= \sum_{-T}^{T} \left(A_v \tau \exp\left(-\frac{\tau^2}{\omega^2} \right) + B_v \right) \\ &= (2T+1) B_v + A_v \sum_{-T}^{T} \tau \exp\left(-\frac{\tau^2}{\omega^2} \right) \\ &= (2T+1) B_v + 0 \end{aligned} \tag{VI.10}$$

$$\Leftrightarrow \quad B_v = 0$$

The sum $\sum_{-T}^{+T} \tau^2 \exp\left(-\frac{\tau^2}{\omega^2} \right)$ is never negative. However, we know that $A_v \approx -\frac{2\tau}{\sqrt{\pi}\omega^3}$. Therefore, we have to set

$$A_v = -\frac{1}{\sum_{-T}^{+T} \tau^2 \exp\left(-\frac{\tau^2}{\omega^2} \right)} \tag{VI.11}$$

VI.1.2 Calculating A_a and B_a

$$\begin{aligned} 2 &= \sum_{-T}^{T} k_a(\tau) \cdot (\tau^2) = \sum_{-T}^{T} \left[A_a \exp\left(-\frac{\tau^2}{\omega^2}\right) \left(\frac{2\tau^2}{\omega^2} - 1\right) + B_a \right] \cdot \tau^2 \\ &= A_a \sum_{-T}^{T} \left[\tau^2 \left(\frac{2\tau^2}{\omega^2} - 1\right) \exp\left(-\frac{\tau^2}{\omega^2}\right) \right] + B_a \sum_{-T}^{T} \tau^2 \\ &= A_a \sum_{-T}^{T} \left[\tau^2 \left(\frac{2\tau^2}{\omega^2} - 1\right) \exp\left(-\frac{\tau^2}{\omega^2}\right) \right] + B_a \frac{T(T+1)(2T+1)}{3} \end{aligned} \tag{VI.12}$$

$$\begin{aligned} 0 &= \sum_{-T}^{T} k_a(\tau) = \sum_{-T}^{T} \left(A_a \exp\left(-\frac{\tau^2}{\omega^2}\right) \left[\frac{2\tau^2}{\omega^2} - 1\right] + B_a \right) \\ \Leftrightarrow \quad A_a &= \frac{-(2T+1)B_a}{\sum_{-T}^{T} \left[\exp\left(-\frac{\tau^2}{\omega^2}\right) \left(\frac{2\tau^2}{\omega^2} - 1\right) \right]} \end{aligned} \tag{VI.13}$$

Combining equations (VI.12) and (VI.13) one obtains

$$\begin{aligned} 2 &= B_a \left(\frac{-(2T+1) \sum_{-T}^{T} \left(\tau^2 \left(\frac{2\tau^2}{\omega^2} - 1\right) \exp\left(-\frac{\tau^2}{\omega^2}\right) \right)}{\sum_{-T}^{T} \left(\left(\frac{2\tau^2}{\omega^2} - 1\right) \exp\left(-\frac{\tau^2}{\omega^2}\right) \right)} + \frac{T(T+1)(2T+1)}{3} \right) \\ \Leftrightarrow \quad B_a &= 2 \left(\frac{-(2T+1) \sum_{-T}^{T} \left(\tau^2 \left(\frac{2\tau^2}{\omega^2} - 1\right) \exp\left(-\frac{\tau^2}{\omega^2}\right) \right)}{\sum_{-T}^{T} \left(\left(\frac{2\tau^2}{\omega^2} - 1\right) \exp\left(-\frac{\tau^2}{\omega^2}\right) \right)} + \frac{T(T+1)(2T+1)}{3} \right)^{-1} \end{aligned} \tag{VI.14}$$

To find the right values for A_v, A_a and B_a one has to calculate the sums with given values T and ω. Velocity and acceleration are calculated with different filter width. The convolution with vectors, e.g. $k_v \otimes \tilde{\mathbf{x}}\Big|_t$, can be calculated by employing to convolution to each component of the vector. To reduce the uncertainty in the position, we also smooth the measured position, $\tilde{\mathbf{x}}$, with the same T and ω used also for the velocity.

The analysis of the trajectories is implemented in C++ using object orientated-programming and standard libraries like `std::vector` to store trajectories in memory.

VI.1.3 Interpolated points

Due to light intensity fluctuations, particles blocking the line of sight, hardware and software problems the trajectory can break up into smaller pieces. The PTV code is able to extrapolate small gaps up to 3 frames ahead and continue if a real point is close to the extrapolation. The Track Connection method (see section IV.5.7) instead is able to connect tracks with gaps of several tenth or hundreds of missing frames. Since such a long interpolation might bias the evaluation, one has to check the

contribution of interpolated points to the statistics. One attempt is to discard every velocity and acceleration value with interpolated points more than a certain threshold. Although this is computationally cheap the bias introduced by interpolated points to the calculation depends on the shape of the kernel. Thus calculating the contribution to the kernel would allow to use more points. Let

$$I(t) = \begin{cases} 1 & \text{if interpolated} \\ 0 & \text{otherwise} \end{cases}$$

and $i_v = C_v \cdot \|k_v\|$ as well as $i_a = C_a \cdot \|k_a\|$ the test kernel functions. Since they are kernel functions they have to obey $i_v \otimes 1 = i_a \otimes 1 = 1$. The influence of an extrapolation can be limited by discarding calculations with

$$i_v \otimes I \geqslant I_{vel,max} \quad \text{or} \quad i_a \otimes I \geqslant I_{acc,max}$$

For $I(t) = const = 1$ the convolution returns 1, for a trajectory containing no extrapolated points the contribution is 0. Usually experiments are performed with many frames per τ_η hence the extrapolation for small gaps won't introduce big errors and the extrapolated points can be used.

The analysis code written by Haitao Xu in our group discards a computation if more than 3 points at a filter window of 27 frames are interpolated. In the worst case of 3 consequent interpolated points this corresponds to $I_{acc,max} \approx 0.3$ and $I_{vel,max} \approx 0.45$. To feel certain

$$I_{acc,max} = 0.20 \quad \text{and} \quad I_{vel,max} = 0.35$$

will be used.

The test has to be done only for one component and the acceleration can be tested before the velocity to avoid redundant calculations.

VI.2 Probability density functions

The probability P of a statistical property x to be within $a \leqslant x \leqslant b$ is:

$$P\left(a \leqslant x \leqslant b\right) = \int_a^b p(x)dx \quad \text{with} \quad \int_{-\infty}^{\infty} p(x)dx = 1 \quad \text{and} \quad p \geqslant 0 \tag{VI.15}$$

where $p(x)$ is the probability density function (PDF). The k-th moment of a probability function is defined as:

$$M_k \equiv \int_{-\infty}^{\infty} p(x)\, x^k\, dx \tag{VI.16}$$

and the k-th central moment as:

$$C_k \equiv \int_{-\infty}^{\infty} p(x)\, (x-\mu)^k\, dx \tag{VI.17}$$

where μ is the mean value of the pdf and the first moment of p. The second central moment of the PDF is the variance of the distribution. The PDFs of velocity and acceleration can be easily created using binning. For the first file being processed the minimum and maximum value of velocity and acceleration components and particle positions are found. These intervals are divided into N_{bins} bins, which are basically counters. Extra bins are added on both sides so that the statistics are not biased by the rather random choice of the minimum and maximum. For each velocity and acceleration value computed the appropriate bin is calculated and the counter is incremented by 1. Then the probability of measuring a value corresponding to the i-th bin X_i is:

$$P\left(X_i\right) = \frac{n_i}{n_{tot}} \tag{VI.18}$$

where n_i denotes the number of counts in this bin and $n_{tot} = \sum_i n_i$ the total number of counts. Using equations (VI.15) and (VI.18) it is:

$$\begin{aligned} P\left(X_i\right) = \frac{n_i}{n_{tot}} &= \int_{min(X_i)}^{max(X_i)} p(x)\, dx \\ &\approx p\left(x\right)\, \Delta x \\ \Leftrightarrow \quad p(x) &= \frac{n_i}{n_{tot}} \frac{1}{\Delta x} \end{aligned} \tag{VI.19}$$

where $x = \frac{max(X_i)+min(X_i)}{2}$ and $\Delta x = max(X_i) - min(X_i)$.

To compare different PDFs it is useful to normalize them using the statistical z-transform. This is done in 2 steps. First the mean μ and standard deviation σ are calculated using equations (VI.16) and (VI.17). Then the probability density is renormalized as a function of $\frac{x-\mu}{\sigma}$. Thus the renormalised PDF is:

$$p\left(\frac{x-\mu}{\sigma}\right) = \frac{n_i}{n_{tot}\,\frac{\Delta x}{\sigma}} = \frac{n_i\,\sigma}{n_{tot}\,\Delta x} \tag{VI.20}$$

VI.3 Subtracting the mean flow field

To obtain the fluctuating velocity one has to subtract the mean flow field. Therefore the measurement volume is subdivided into $n \times n \times n$ spatial bins. Particles passing through such a spatial bin will allow to calculate the mean and rms values of acceleration and velocity. After processing all movies the mean flow field can be approximated as an interpolation of the obtained mean velocities.

To create a steady mean flow field a trilinear interpolation[3] instead of a nearest neighbor method was chosen as an interpolation method.

It is assumed that only direct neighbors are important. Let $\mathbf{C} = (x, y, z)$ be the point whose value has to be interpolated and $\mathbf{C}_{XYZ}$ the eight vortices of a cuboid around $\mathbf{C}$. The cuboid is rescaled to a cube of edge length one[4]. X, Y and Z denote

[3] A trilinear interpolation is a linear interpolation in 3D.

[4] Therefore it is $x, y, z \in [0, 1]$

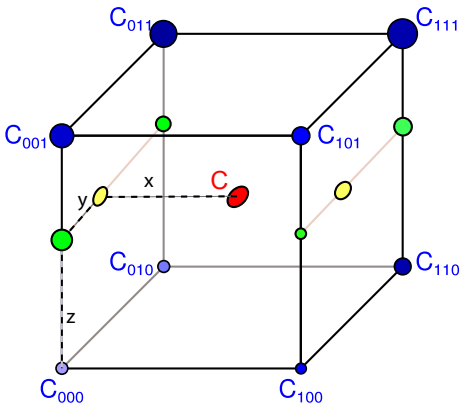

Figure VI.1: Trilinear interpolation for a value at point C. The value at a point is visualised by the size and shape of the circle, green corresponds to the rst interpolation i, yellow to the second step j. The cell is a cube with an edge length of 1.

the coordinates of a corner. Furthermore $v(\mathbf{C})$ denotes the value at position $\mathbf{C}$ and v_{XYZ} the value at a corner $\mathbf{C}_{XYZ}$.

If the number of statistics in bin is not su cient, the mean over the all usable spatial bins will be used.

The interpolation is done by following three linear interpolation steps.

1. Interpolate the values along the z-axis. The four interpolated values are:

$$\begin{aligned} i_1 &= v_{000} + z \quad (v_{001} \quad v_{000}) \\ i_2 &= v_{100} + z \quad (v_{101} \quad v_{100}) \\ i_3 &= v_{010} + z \quad (v_{011} \quad v_{010}) \\ i_4 &= v_{110} + z \quad (v_{111} \quad v_{110}) \end{aligned} \tag{VI.21}$$

   In gure VI.1 this is visualized by the four green dots. The size of the green dots is a size between their upper and bottom neighbor.

2. Interpolating between the interpolated points in y direction

$$\begin{aligned} j_1 &= i_1 + y\,(i_4 \quad i_1) \\ j_2 &= i_2 + y\,(i_3 \quad i_2) \end{aligned} \tag{VI.22}$$

   This corresponds to the two yellow circles in gure VI.1.

3. by interpolating in x -direction we nd

$$\begin{aligned} v(\mathbf{C}) &= j_1 + x\,(j_2 \quad j_1) \\ &= i_1 + y\,(i_4 \quad i_1) + x\,i_2 + x\,y\,(i_3 \quad i_2) \quad x\,i_1 \quad x\,y\,(i_4 \quad i_1) \\ &= i_1\,(1 \quad x \quad y + x\,y) + i_2\,(x \quad x\,y) + i_3\,(x\,y) + i_4\,(y \quad x\,y) \end{aligned} \tag{VI.23}$$

Combining all equations we obtain

$$\begin{aligned} v(\mathbf{C}) = {} & v_{000} + z\,(v_{001} - v_{000}) \\ & + y\,v_{110} + y\,z(v_{111} - v_{110}) \\ & - y\,v_{000} - y\,z\,(v_{001} - v_{000}) \\ & + x\,v_{100} + x\,z(v_{101} - v_{100}) \\ & + x\,y\,v_{010} + x\,y\,z(v_{011} - v_{010}) \\ & - x\,y\,v_{100} - x\,y\,z(v_{101} - v_{100}) \\ & - x\,v_{000} - x\,z(v_{001} - v_{000}) \\ & - x\,y\,v_{110} - x\,y\,z(v_{111} - v_{110}) \\ & + x\,y\,v_{000} + y\,z(v_{001} - v_{000}) \end{aligned} \tag{VI.24}$$

Rearranging (VI.24)

$$\begin{aligned} v(\mathbf{C}) = {} & v_{000}\,(1-x)(1-y)(1-z) \\ & + v_{001}\,(1-x)(1-y)\,z \\ & + v_{010}\,x\,y\,(1-z) \\ & + v_{011}\,x\,y\,z \\ & + v_{100}\,x\,(1-y)\,(1-z) \\ & + v_{101}\,x\,(1-y)\,z \\ & + v_{110}\,y\,(1-x)\,(1-z) \\ & + v_{111}\,y\,(1-x)\,z \end{aligned} \tag{VI.25}$$

Before calculating Eulerian and Lagrangian statistics the mean velocity field and the mean acceleration field were subtracted.

VI.4 Linear approximation of the flow field

The mean flow field $\langle \mathbf{u}(\mathbf{r}) \rangle$ can be approximated as:

$$\mathbf{u} \approx \mathbf{u}(\mathbf{r}_0) + \underline{\underline{\mathbf{M}}}\,(\mathbf{r} - \mathbf{r}_0) \tag{VI.26}$$

where $\underline{\underline{\mathbf{M}}}$ is an approximation of the velocity-gradient, or Jacobian, $\nabla \mathbf{u}(\mathbf{r}_0)$, at the point $\mathbf{r}_0$. In section VII.4.3, the velocity-gradient, $\underline{\underline{\mathbf{M}}}$, will be used to calculate the rate of strain and the local vorticity at $\mathbf{r}_0$.

$\underline{\underline{\mathbf{M}}}$ can be obtained from the mean flow using the following procedure. N velocity vectors $\mathbf{u}_i = \left(u_i^x \mid u_i^y \mid u_i^z \right)$ at their corresponding position $\mathbf{r}_i \equiv \left(x_i \mid y_i \mid z_i \right)$ have been measured. Lets define $\delta_\mathbf{i} = \left(\delta_i^x \mid \delta_i^y \mid \delta_i^z \right) = \left(x_i - r_0^x \mid y_i - r_0^y \mid z_i - r_0^z \right)$ and $\mathbf{u}(\mathbf{r}_0) = \left(u_0^x \mid u_0^y \mid u_0^z \right)$. Applying an arbitrary pair $\mathbf{u}_i, \delta_i$ to equation (VI.26) yields the following three equations

$$u_i^x = u_0^x + M_{11}\,\delta_i^x + M_{12}\,\delta_i^y + M_{13}\,\delta_i^z \tag{VI.27a}$$
$$u_i^y = u_0^y + M_{21}\,\delta_i^x + M_{22}\,\delta_i^y + M_{23}\,\delta_i^z \tag{VI.27b}$$
$$u_i^z = u_0^z + M_{31}\,\delta_i^x + M_{32}\,\delta_i^y + M_{33}\,\delta_i^z \tag{VI.27c}$$

Nevertheless, the continuity equation dictates:

$$M_{11} + M_{22} + M_{33} = 0 \tag{VI.28}$$

Rearranging equation (VI.26) and employing the constraint (VI.28) gives three independent overdetermined systems of linear equations:

$$\begin{pmatrix} \delta_1^x & \delta_1^y & \delta_1^z & 1 \\ \delta_2^x & \delta_2^y & \delta_2^z & 1 \\ & \vdots & & \\ \delta_N^x & \delta_N^y & \delta_N^z & 1 \end{pmatrix} \cdot \begin{pmatrix} M_{11} \\ M_{12} \\ M_{13} \\ u_0^x \end{pmatrix} = \begin{pmatrix} u_1^x \\ u_2^x \\ \vdots \\ u_N^x \end{pmatrix} \tag{VI.29a}$$

$$\begin{pmatrix} \delta_1^x & \delta_1^y & \delta_1^z & 1 \\ \delta_2^x & \delta_2^y & \delta_2^z & 1 \\ & \vdots & & \\ \delta_N^x & \delta_N^y & \delta_N^z & 1 \end{pmatrix} \cdot \begin{pmatrix} M_{21} \\ M_{22} \\ M_{23} \\ u_0^y \end{pmatrix} = \begin{pmatrix} u_1^y \\ u_2^y \\ \vdots \\ u_N^y \end{pmatrix} \tag{VI.29b}$$

$$\begin{pmatrix} \delta_1^x & \delta_1^y & 1 \\ \delta_2^x & \delta_2^y & 1 \\ & \vdots & \\ \delta_N^x & \delta_N^y & 1 \end{pmatrix} \cdot \begin{pmatrix} M_{31} \\ M_{32} \\ u_0^z \end{pmatrix} = \begin{pmatrix} u_1^z + (M_{11} + M_{22})\delta_1^z \\ u_2^z + (M_{11} + M_{22})\delta_2^z \\ \vdots \\ u_N^z + (M_{11} + M_{22})\delta_N^z \end{pmatrix} \tag{VI.29c}$$

where the M_{ij} and u_0^x, u_0^y, u_0^z are unknowns.

For an overdetermined systems of linear equations $\underline{\underline{\mathbf{A}}}\mathbf{x} = \mathbf{b}$, with $\underline{\underline{\mathbf{A}}}$ a $n \times m$, $\mathbf{x}$ a $m \times 1$ and $\mathbf{b}$ a $n \times 1$ matrix/vector, the inverse of $\underline{\underline{\mathbf{A}}}$ does not exist if $n \neq m$. However, one solution of the system is

$$\mathbf{x} = \underline{\underline{\mathbf{A}}}^{+}\,\mathbf{b} \tag{VI.30}$$

where $\underline{\underline{\mathbf{A}}}^{+}$ is the pseudo-inverse of $\underline{\underline{\mathbf{A}}}$, which can be calculated from a singular value decomposition of $\underline{\underline{\mathbf{A}}}$. A second solution is the use of an optimization scheme which finds

$$\min\left(\|A\,x - b\|\right) \tag{VI.31}$$

We are using equation (VI.30) to determine the matrix $\underline{\underline{\mathbf{M}}}$.

VI.5 Calculation of the Eulerian autocorrelation R_{ij} and second-order-structure function D_{ij}

Assuming a locally isotropic flow we can compute Eulerian structure functions and autocorrelation by the following procedure.

Step 1 Subtract the mean velocity field as described in section VI.3.

Step 2 For each frame, f, create a list of all points for which a velocity, $\mathbf{u}'$, was calculated.

Step 3 Pick two velocity vectors from this list: $\mathbf{u}_1$ and $\mathbf{u}_2$. These vectors are separated by r $\mathbf{e}_r$, where $\mathbf{e}_r$ denotes the unit vector of $\mathbf{r}$.

Step 4 As explained in section III.6, the Eulerian structure functions, $D_{ij}(r)$ and $R_{ij}(r)$, depend only on the length, r, of the separation vector, $\mathbf{r}$, in a locally isotropic ow with subtracted mean ow. Thus, one can calculate $D_{LL}(r) = \langle [\mathbf{u}_1 \ \mathbf{e}_r \ \mathbf{u}_2 \ \mathbf{e}_r]^2 \rangle$ and $R_{LL}(r) = \langle [\mathbf{u}_1 \ \mathbf{e}_r] [\mathbf{u}_2 \ \mathbf{e}_r] \rangle$ and average the result employing a binning technique for r.

Step 5 Analogous to the prior step one can gain the transverse structure function and auto correlation by substituting $\mathbf{e}_r$ for a vector $\mathbf{e}_n$ perpendicular to $\mathbf{e}_r$.

Step 6 The ensemble average can be computed by using all possible combinations of points at a time step and doing this for each frame.

A transverse vector $\mathbf{e}_n = \mathbf{e}_a \ \mathbf{e}_r$ with an arbitrarily set vector $\mathbf{e}_a$ can be used to obtain the transverse second order structure function and autocorrelation. A second transverse vector $\mathbf{e}_k$ can be obtained from $\mathbf{e}_k = \mathbf{e}_n \ \mathbf{e}_r$. However, the cross product vanishes for $\mathbf{e}_r = \mathbf{e}_a$. Moreover, in the case both when vectors are close to parallel the measurement error in $\mathbf{e}_r$ results in a bigger uncertainty in $\mathbf{e}_n$.

Nevertheless, we set $\mathbf{e}_a$ to be parallel to the z- axis $\mathbf{e}_z$ to calculate the two normal components. If $\mathbf{e}_r$ and $\mathbf{e}_z$ are close to parallel[5], they were set $\mathbf{e}_n = \mathbf{e}_x$ and $\mathbf{e}_n = \mathbf{e}_y$.

Of course, one can use the same method to compute also higher order structure functions, as well as Eulerian measures based on the acceleration.

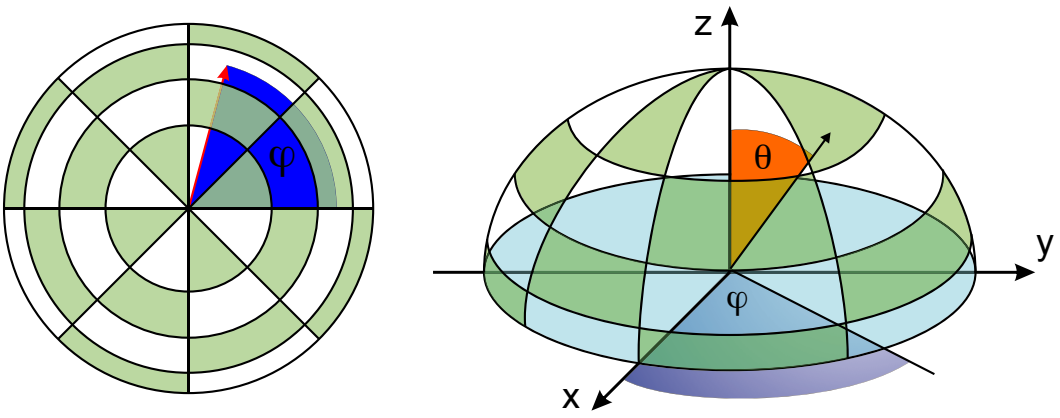

Figure VI.2: Sketch of the angular bins to determine a dependence of the structure functions and autocorrelations on the direction. The direction of the separation vector, $\mathbf{r}$, is expressed with the help of spherical coordinates τ. The structure functions as well as autocorrelations do not depend on the sign of $\mathbf{r}$, it is su cient to map $\mathbf{r}$ on a half sphere. The sketch illustrates 8 bins for and 4 bins for τ. The area of each bin is the same. Thus, in an isotropic ow they will be lled equally. The left gure shows a top view of the sphere.

[5]They are approximately parallel if $z > 100 \ (\ x \ + \ y \ )$

In order to check the angular dependence of D_{ij} and R_{ij} one can bin the both measures according to the spherical coordinates[6] of the unit vector $\mathbf{e}_r(r = 1, \phi, \theta)$. Since the sign of $\mathbf{r}$ is not important, we can map $\mathbf{r}$ on a half sphere. Changing the sign of $\mathbf{r}$ can be done by changing the sign of θ and setting ϕ to $\phi + 180°$.

In order to fill the bins approximately evenly, each bin $A_{\theta,\phi}$ has to have the same area. This is achieved by a constant spacing in ϕ but an adjusted spacing in θ. The area of the i-th slice (limited by θ_i and θ_{i-1}) of an unit- sphere is

$$A_i = 2\pi r(h_i - h_{i-1}) = 2\pi \left(cos(\theta_i) - cos(\theta_{i-1})\right) \tag{VI.32}$$

Each slice has to cover

$$A_i = \frac{A_{total}}{m} = \frac{2\pi}{m}$$

Combining both we get $\theta_i = \arccos\left(\frac{i}{m}\right)$. The number i of the bin corresponding to an (arbitrary) angle θ is the first i with $\theta_{i+1} > \theta$. A sketch of the distribution of the bins in provided in figure VI.2.

[6] It is $\theta = \arccos(\mathbf{e}_r \cdot \mathbf{e}_z)$ and $\phi = \arccos\left(\|\mathbf{e}_r \cdot \mathbf{e}_x\| / \sqrt{(\mathbf{e}_r \cdot \mathbf{e}_x)^2 + (\mathbf{e}_r \cdot \mathbf{e}_y)^2}\right)$

VII Results

VII.1 Experiments performed

Two arrangements of the PTV system have been used to investigate flows with different strengths and types of forcing, in each case using the stainless steel propellers. An overview of the results as well as of the corresponding Stokes numbers is provided in table VII.1 and table VII.2.

As described in section V.1.2, each propeller is driven by a motor through a $5:1$ gear. The user of the apparatus will specify the motor frequency, although the relevant property is the the propeller speed. Therefore, we will use the unit rpm to refer to the motor speed and Hz to indicate the real propeller speed.

VII.1.1 Big measurement volume experiments

Using 60mm Nikon objectives, a relatively big measurement volume of approximately $16 \times 10 \times 10\,[cm^3]$ situated in the center of the LEM could be resolved. *LiteSphere* particles with a diameter $< 90\mu m$ manufactured by MO-SCI cooperation were used as tracers. A picture of the particles is provided in figure V.13 in section V.1.6. The uncertainty of the stereo-matching process was $86 \pm 46\,\mu m$.

Clockwise and Counterclockwise Forcing Experiments with all motors at the same speed were done at $+1\,Hz$ ($+300\,rpm$), $1.66\,Hz$ ($+500\,rpm$), $+675\,rpm$, $+5\,Hz$ ($+1500\,rpm$), $+7.5\,Hz$ ($+2250\,rpm$), $+9.33\,Hz$ ($+2800\,rpm$), $+5000\,rpm$ and $-9.33\,Hz$ ($-2800\,rpm$). The difference in the direction of the rotation will be denoted by clockwise (CW) for positive frequencies and counterclockwise (CCW) in the other case. The motors of the LEM are able to run at up to $+5000\,rpm$. However, due to illumination problems we collected less than 400000 points at $+5000\,rpm$. Therefore, this experimental run is excluded.

Anisotropic Forcing The six motors at the top and at the bottom were pushing with $3.33\,Hz$ ($+1000\,rpm$), the six propellors at the 'equator' were not rotating.

Random Forcing One experiment was performed using randomly picked frequencies f_i for each motor. Every 30 seconds new frequencies were chosen. From previous experiments in a French-Washing machine we knew that $u' \propto f$. Inserting this into equation[1] (III.22) yields $\varepsilon \propto f^3$. Therefore, we enforced $\frac{1}{12}\sum_{i=1}^{12} f_i^3 = f^3 = (500\,rpm)^3$ and $f_i \in [300\,rpm; 700\,rpm]$ to ensure a constant energy injection rate, ε, comparable to clockwise forcing at $1.66\,Hz$ ($+500\,rpm$).

[1] $\varepsilon \sim \frac{\mathcal{U}^3}{\mathcal{L}}$

VII.1.2 Small measurement volume experiments

Using 200 mm Nikon objectives, a smaller measurement volume of approximately $3\times2\times2$ $[cm^3]$ situated in the center of the LEM could be resolved. 42 μm polystyrene particles (Duke Scientific) were used as tracers. A picture of the particles is provided in figure V.13 in section V.1.6. The uncertainty of the stereo-matching process was $19 \pm 6\mu m$.

Clockwise Forcing Experiments with all motors at the same speed were done at $+1$ Hz ($+300$ rpm), 1.66 Hz ($+500$ rpm), $+675$ rpm.

Random Forcing The random forcing described in VII.1.1 was repeated under the same forcing conditions.

In the case of anisotropic and random forcing, the frequencies of the propellers were not uniform, and thus no clear definition of the motor frequency can be given. We estimate the effective frequency of random and anisotropic forcing as $+1.66$ Hz ($+500$ rpm) and $+3.33$ Hz ($+1000$ rpm) respectively.

VII.2 Selection of the Filter Width for the differentiating kernel and the parameters for the track connection code

To use the track connection method [28] described in section IV.5.7, the spatial and temporal search distance as well as the measurement error have to specified. The measurement error σ_p is known from the calibration, and the spatial search distance, d_s, is limited by the average distance between particles. Therefore, we measured the mean, $\langle N_p \rangle$, and the standard deviation $\left\langle (\langle N_p \rangle - N_p)^2 \right\rangle^{1/2}$ of particles per frame, N_p, in the biggest trajectory file. Since the size, V, of the observation volume is known, the spatial search distance d_s was set to

$$d_s \leqslant \frac{\sqrt[3]{V}}{\langle N_p \rangle + \left\langle (\langle N_p \rangle - N_p)^2 \right\rangle^{1/2}} \tag{VII.1}$$

The term $\langle N_p \rangle + \left\langle (\langle N_p \rangle - N_p)^2 \right\rangle^{1/2}$ estimates the maximum number of particles in the volume, whereas $\sqrt[3]{V}$ returns the characteristic length of the observation volume. Equation (VII.1) can be seen as an estimate of the minimum average distance between particles. The temporal search distance, t_s, was varied to determine its optimal value which allows the code to find the maximal number of connection with a negligible number of wrong connections. t_s was set to 150 frames for all experiments.

As described in section VI.1, the derivatives of a gaussian kernel are used to calculate velocity and acceleration. The filter width $W_f = 2T + 1$ and the filter variance ω_f have to be chosen such that the statistics obtained do not depend on the choice of

W_f and ω_f. Also, they should be as small as possible to use the maximum amount of data and to see short time events. Each experiment has been processed with different filter widths and a ratio of W_f to ω_f of approximately 3 to determine the optimal filter widths. The ratio was chosen according to previous experiences of our group with the PTV system (see e.g. [30]).

The measurement errors in position strongly influence the computation of properties based on velocity and acceleration. It can be shown [17] that applying the acceleration convolution filter on pure delta-correlated (white) noise produces an acceleration variance which is

$$\langle a^2 \rangle \propto W_f^{-5} \tag{VII.2}$$

For longer filter windows the noise contribution gets smaller until the curve shows a kink at a certain W_f^{acc}. At this point the contribution of the filter width is such that the contribution of noise is small, and short time events of acceleration can still be measured. Therefore, the r.m.s. of acceleration and the theoretical -2.5 power-law are log-log plotted to determine the optimal filter width W_f^{acc}. Because showing all 14 runs would go beyond the aim of this text, the run at $+9.33\ Hz$ ($+2800\ rpm$) (figures VII.1 and VII.2) has been picked as a representative example.

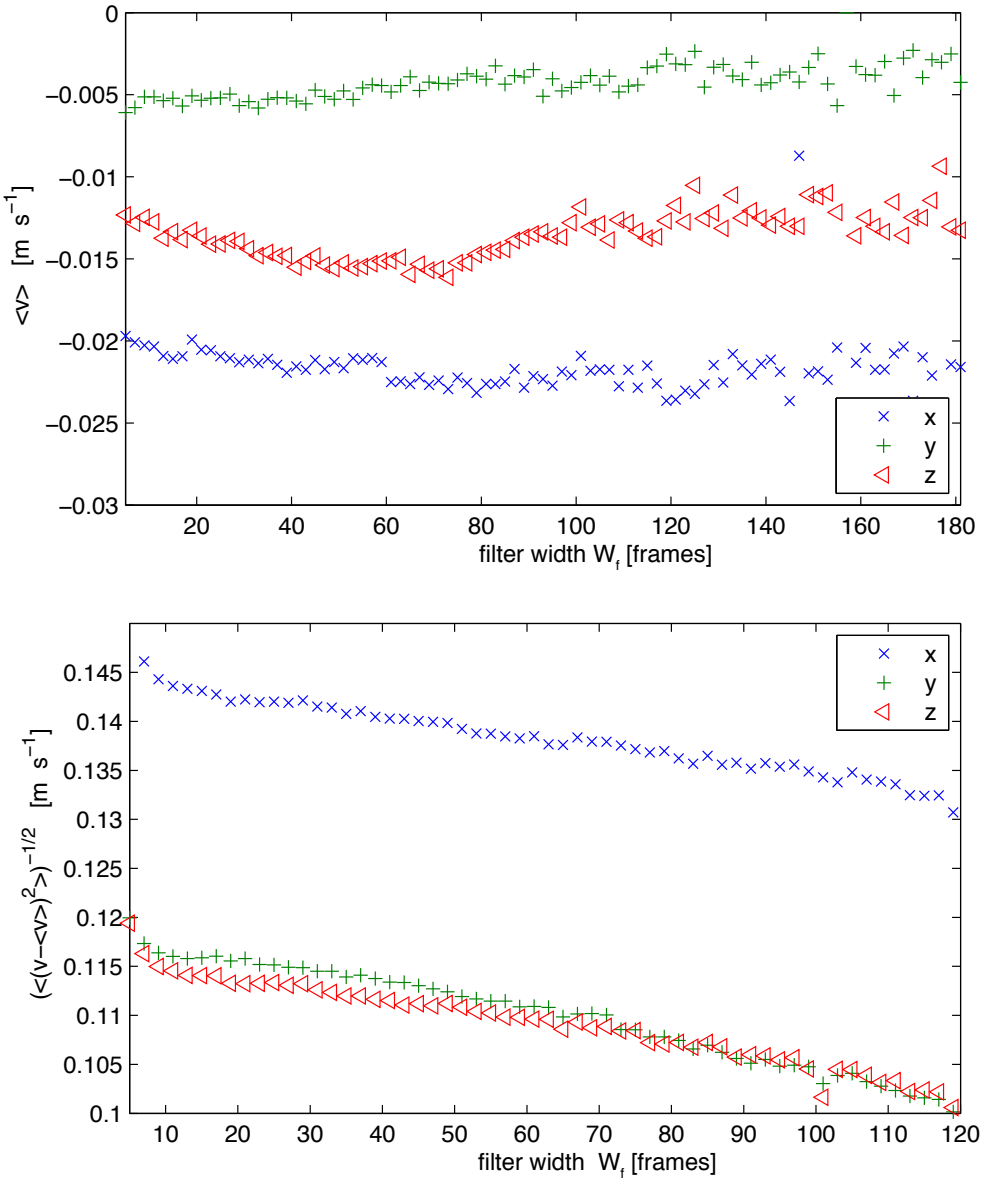

Figure VII.1: Velocity dependence on the filter width, $W_f = 2T+1$, for the $+9.33\ Hz$ ($+2800\ rpm$) run. Velocity statistics are less sensitive to the filter width than acceleration statistics (see figure VII.2).

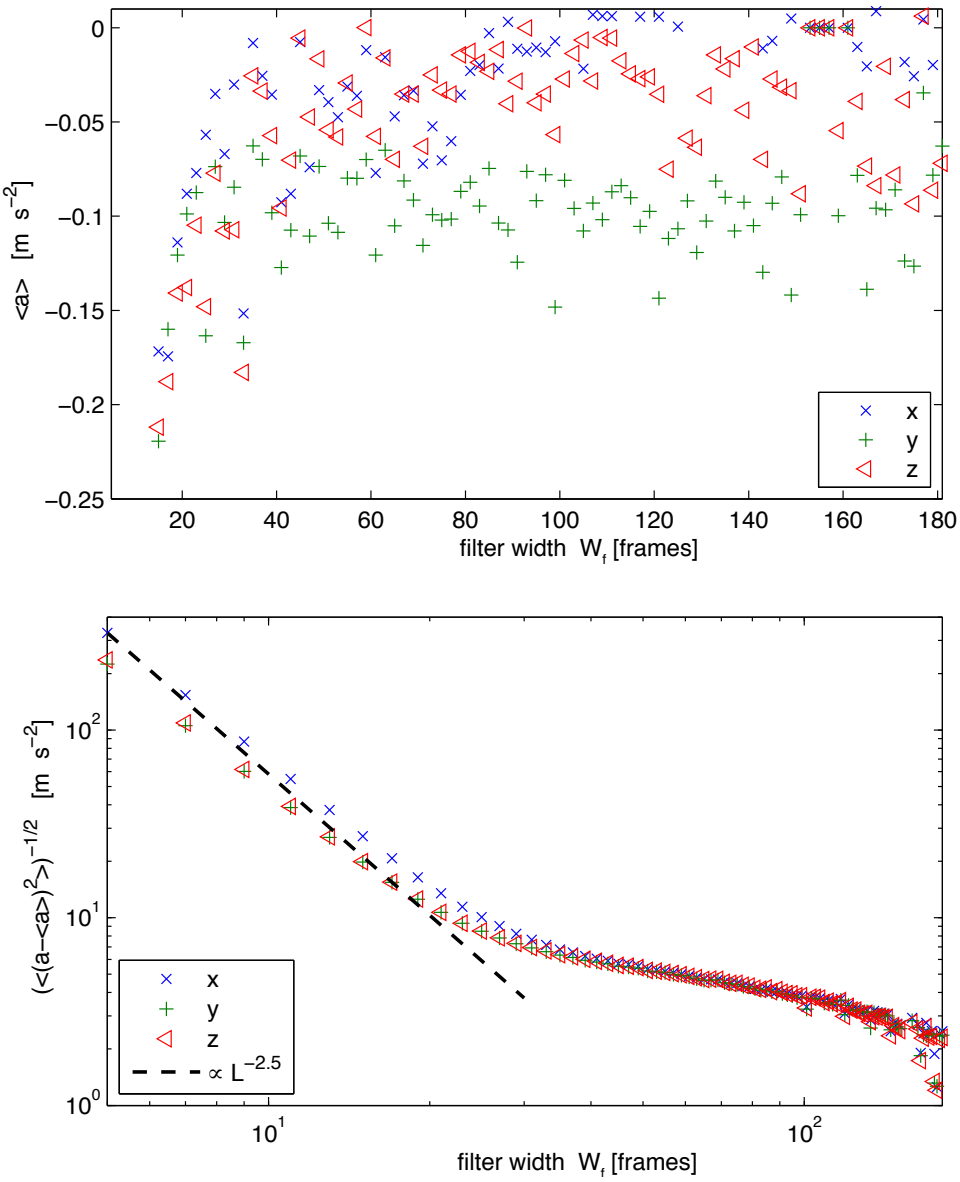

Figure VII.2: Acceleration dependence on the filter width, $W_f = 2T + 1$, for the $+9.33\ Hz$ ($+2800\ rpm$) run. Note the kink in the acceleration rms at a filter width of approximately 40 frames;

VII.3 Basic properties of the apparatus

Before the apparatus can be used to investigate to properties of turbulent flows, it has to be characterized. This section presents basic properties such as the Reynolds number and the Kolmogorov scales for different propeller speeds and different ways of driving the flow.

The observation volume was divided in $n \times n \times n$ sub-volumes. For each sub-volume a PDF of the velocity was built from the trajectories passing through it. Thus, each PDF contains a temporal average of the velocities in the sub-volume. As described in section VI.3, the moments of these PDFs define the Eulerian mean flow field. We chose values of n for each experiment such that the sub-volumes contain sufficient data. A global PDF can then be built by summing the histograms from all sub-volumes. Finally, we chose to consider only those sub-volumes which contained more than 1000 data points. The requirement of a minimum number of data points reduces the contribution of noise in the measurement system to the observations.

To avoid ambiguity in the describing the flow the following definitions will be used:

Mean velocity We define the mean velocity, $\langle \mathbf{u} \rangle$, as the first moment of the global velocity PDF.

Fluctuation velocity The fluctuating velocity, $\mathbf{u}'$, is estimated as the standard deviation (r.m.s.) of the global velocity PDF.

Spatial inhomogeneity Spatial inhomogeneities in the mean flow can result in flows from different sub-volumes canceling each other, and so the full influence of the mean flow may not be evident by considering the (global) mean velocity. Therefore, we define the spatial inhomogeneity, $\mathbf{h}$, as the r.m.s., taken over the different sub-volumes, of the Eulerian mean velocity field.

Characteristic velocities

The dependencies of the fluctuating and mean velocities on the propeller frequency, f, are shown in the figures VII.3 and VII.5. The fluctuating velocity, $\mathbf{u}'$, is on the order of several $\frac{cm}{s}$, whereas the mean velocity is usually less than 20% of the fluctuating velocity. We found that both the mean velocity, $\langle \mathbf{u} \rangle$, and the fluctuating velocity, $\mathbf{u}'$, grow with increasing propeller speed, f. In the case of the fluctuating velocity, and for clockwise forcing, we observe a linear growth with the propeller frequency. In other words

$$\mathbf{u}' \propto f \tag{VII.3}$$

This is in good agreement with results obtained by our group (e.g. [30]) in a French-Washing machine. We observe that counterclockwise forcing creates smaller turbulent fluctuations than clockwise forcing. Furthermore, random forcing is slightly more efficient in creating turbulent fluctuations than clockwise forcing at 1.66 Hz (+500 rpm) although it was designed to inject the same power into the fluid. For clockwise forcing, the propellors create jets directed toward the center of the apparatus, whereas for

counterclockwise forcing, the propellors pull fluid away from the center toward the vertices of the icosahedron.

As depicted in figure VII.4, the spatial inhomogeneity, $\mathbf{h}$, of the flow increases with the propeller speed. However, the fluctuating velocities are 3 to 4 times larger than the corresponding spatial inhomogeneities at all propellor speeds.

As an example, figure VII.7 shows a cut through the Eulerian fields of mean and fluctuating velocities at $+1.66\ Hz$ ($+500\ rpm$). Inside the observed area the magnitude of the fluctuating velocity, $|\mathbf{u}'(x, y \approx 0, z)|$, is uniform. Similar behavior was observed for the Eulerian mean velocity field, $\langle \mathbf{u} \rangle (x, y \approx 0, z)$. We attribute the spatial fluctuations occurring near the borders of the region to insufficient statistics, since the number of trajectories is much lower at the edge of the illuminated region than in the middle.

According to figure VII.6, no pronounced differences in the x, y and z components of $\mathbf{u}'$ are found for low propeller speeds. Furthermore, anisotropic forcing created pronounced anisotropy in the fluctuating velocities as expected. We observed also that the flow tends to become more anisotropic with increasing propeller speeds. This might be because our propellers are self-made. Differences in the angles of the propeller vanes, between propellors, can be understood as being equivalent to the propellors rotating at different frequencies, which leads to an inhomogeneous and anisotropic injection of energy. As explained below, we found that the energy transfer rate is proportional to frequency cubed. Consequently, deviations between propellers will become increasingly pronounced as the propellor frequency is increased.

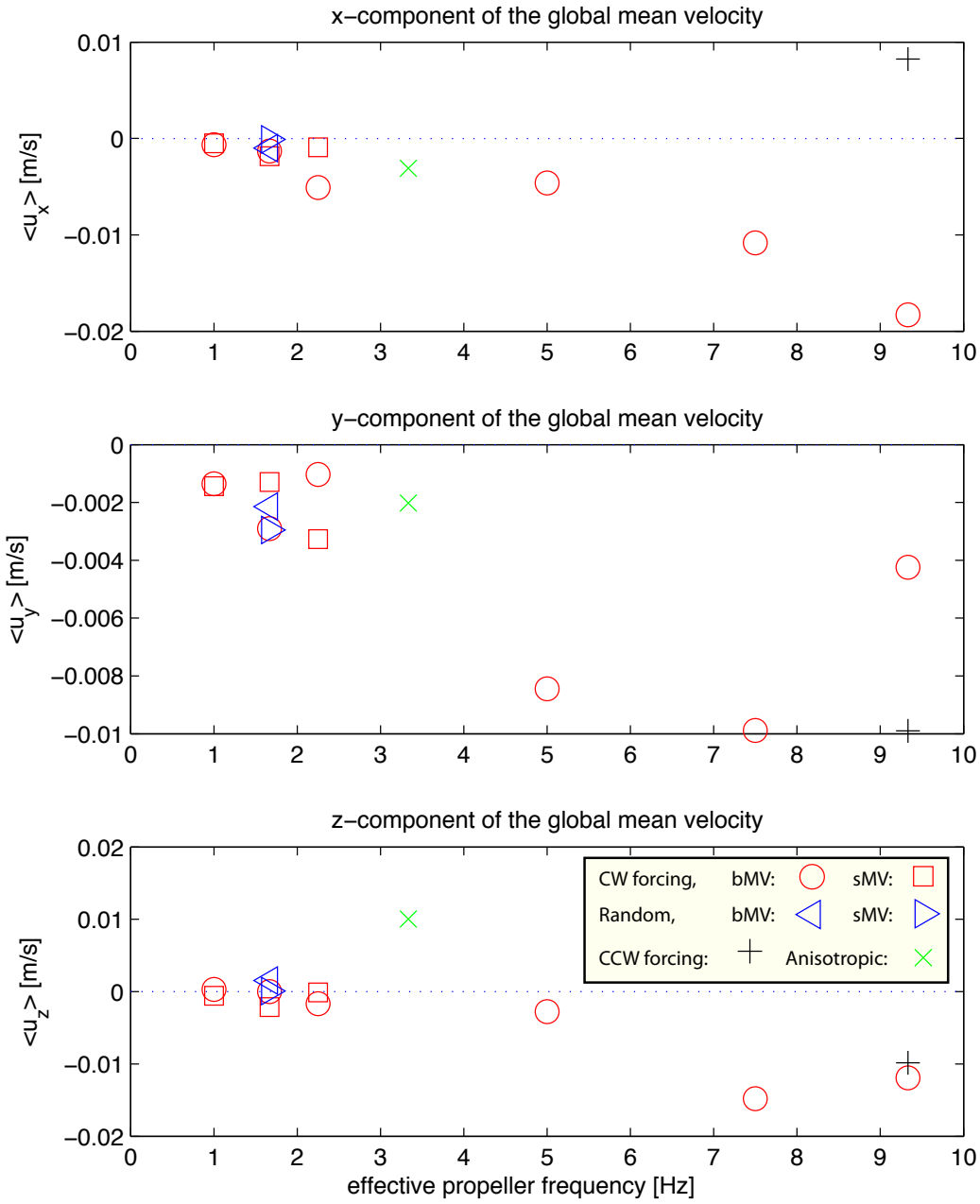

Figure VII.3: Mean velocity versus the propeller frequency. The mean velocity increases with the propeller speed and the difference between the three components of $\langle \mathbf{u} \rangle$ become more distinct. However, the mean flow is less than 20% of the fluctuating velocity.

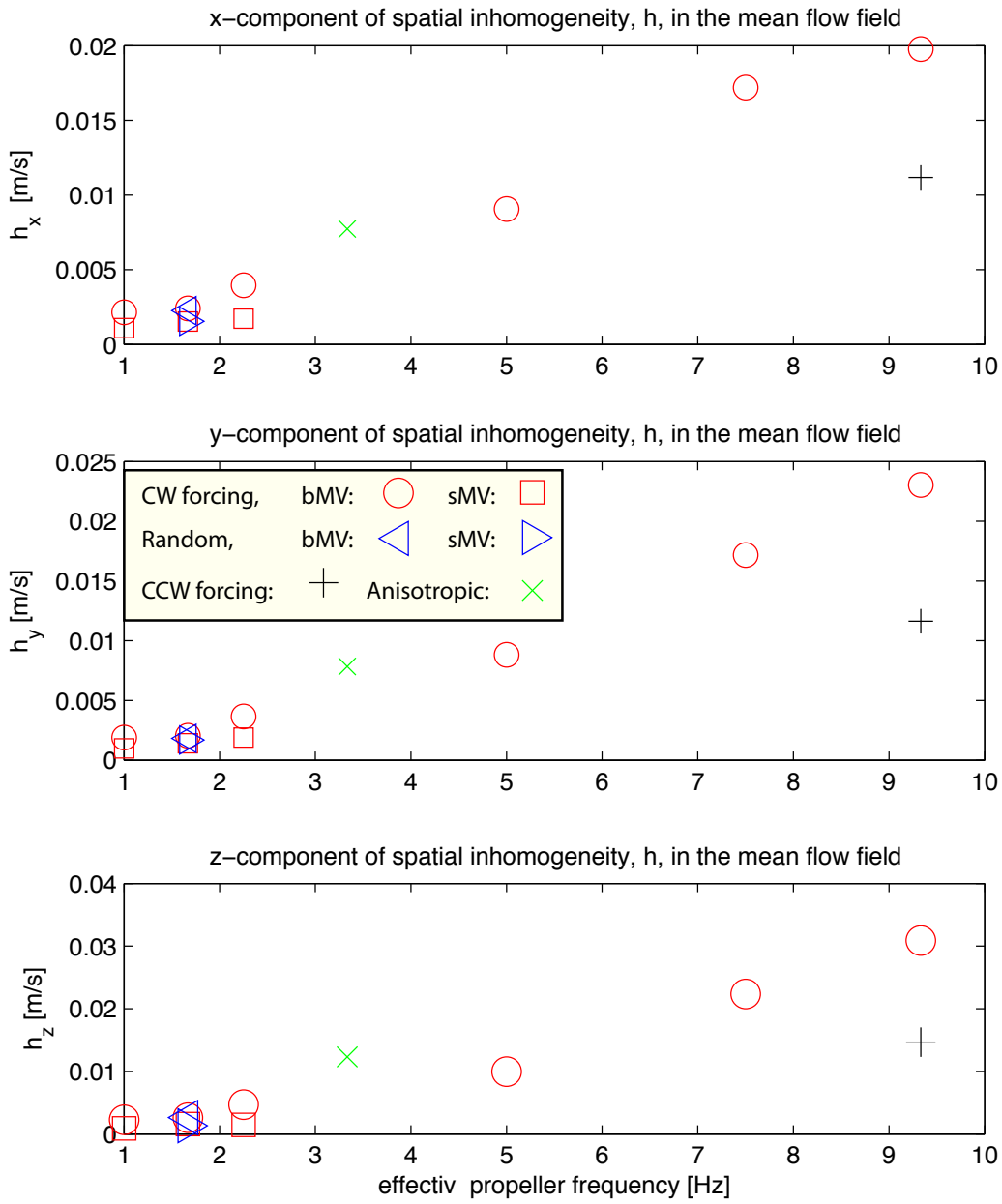

Figure VII.4: Spatial inhomogeneity, **h**, of the mean flow field versus the propeller frequency. The mean flow becomes spatial inhomogeneous with increasing propeller speed. The fluctuating velocities, however, are still 3 to 4−times stronger than the corresponding spatial inhomogeneity of the velocity field.

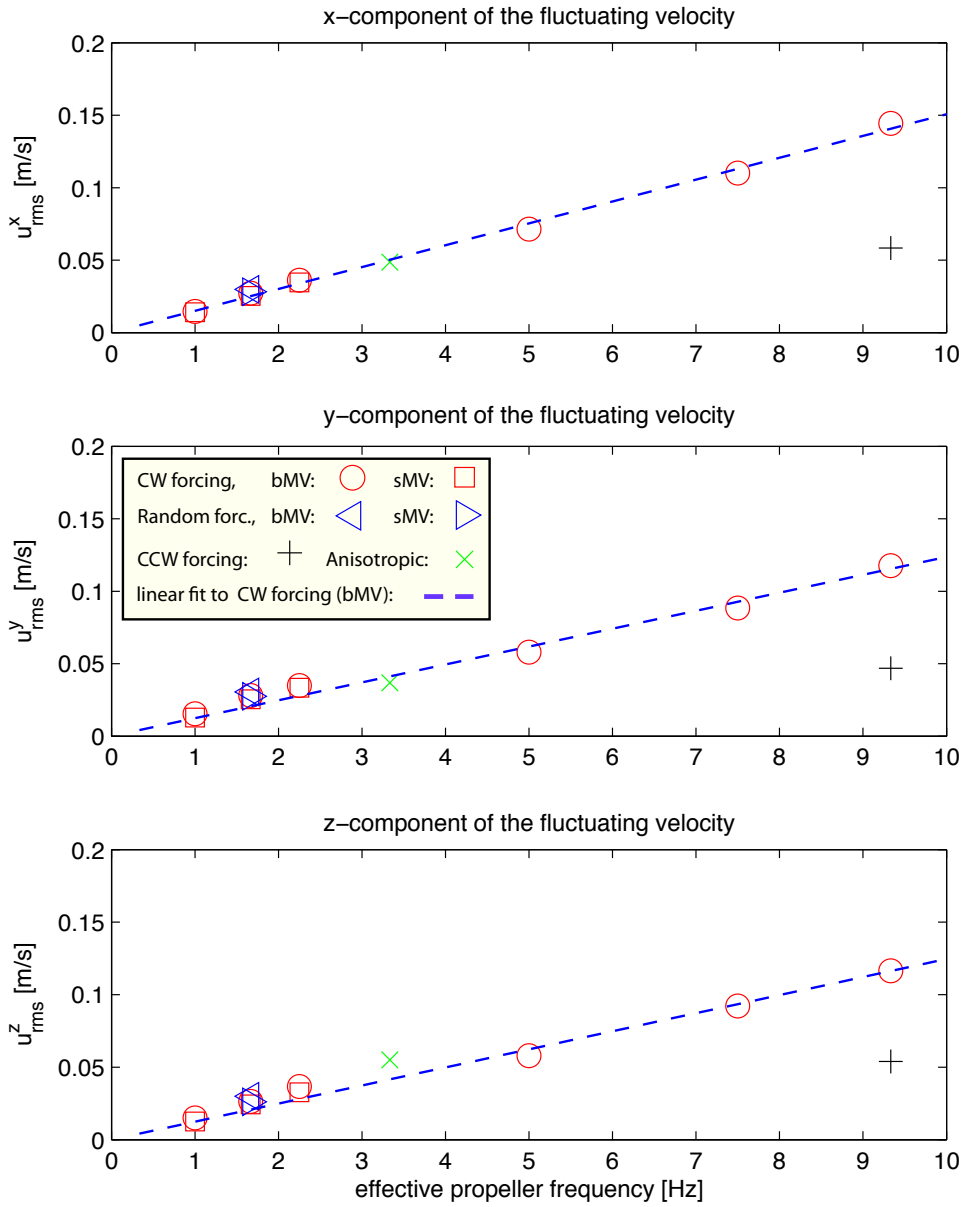

Figure VII.5: Fluctuating velocity versus the propeller frequency. For clockwise and random forcing the r.m.s. of the velocity scales linearly with the propeller frequency. CCW forcing produce a less turbulent flow regime, and anisotropic forcing created a less isotropic fluctuating velocity.

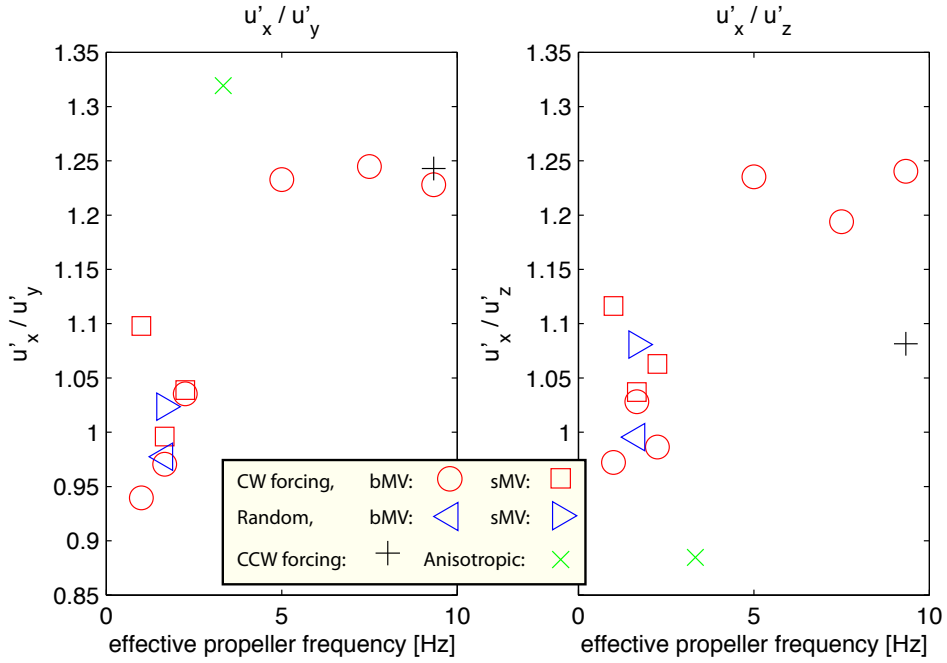

Figure VII.6: Anisotropy of the fluctuating velocity versus the propeller frequency. The ratios $\frac{u'_x}{u'_y}$ and $\frac{u'_x}{u'_y}$ are nearly unity for small propeller frequencies. Thus the turbulent fluctuations are isotropic over the observation volume. With increasing propeller speed, the flow becomes anisotropic. This might be because our propellers are self-made. Differences in the angle of the propeller vanes can be understood as forcing with different frequencies and thus an inhomogeneous and anisotropic injection of energy. As explained later, the energy transfer rate is proportional to frequency cubed. Consequently, deviations between propellers will become detectable at sufficiently high frequencies. As exspected, we observed that anisotropic forcing creates a flow with a pronounced anisotropy.

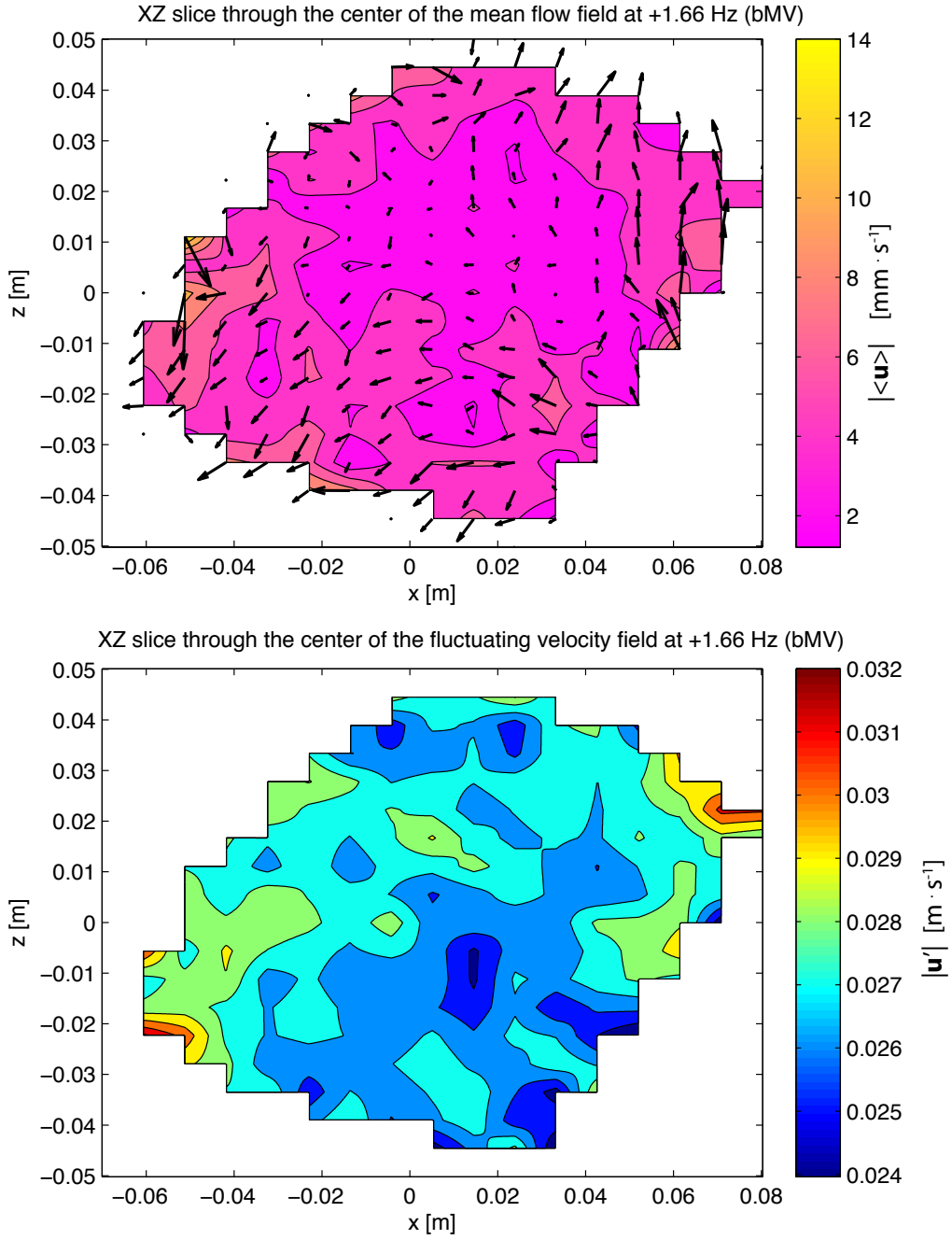

Figure VII.7: $xz-$cut through the Eulerian field of mean and fluctuating velocity at 1.66 Hz (500 rpm). It should noted that the uncertainty at the border is bigger because less data was collected in these regions.

Energy transfer rate

We calculated the Eulerian second and third order structure functions as is described in section VI.5. Taking the Kolmogorov constant $C_2 = 2.1$, together with the equations[2] (III.39), (III.38) and (III.42), enables us to compute three separate estimates of the energy transfer rate, $\varepsilon(r)$, with its corresponding error estimate σ_ε. For that purpose, we determine the inertial range, $r_1 \ldots r_2$, from the width of the plateau of each appropriately compensated structure function. The plateau region is typically only a few tens of η long. Once the inertial range is known we compute

$$\varepsilon \approx \langle \varepsilon(r) \rangle \Big|_{r=r_1 \ldots r_2} \quad \text{and} \quad \sigma_\varepsilon \approx \left\langle \left(\varepsilon(r) - \langle \varepsilon(r) \rangle \right)^2 \right\rangle^{1/2} \Big|_{r=r_1 \ldots r_2}$$

for the second order structure functions, denoted $\varepsilon(D_{LL})$ and $\varepsilon(D_{NN})$, and the third order structure function, denoted $\varepsilon(D_{LLL})$. As an example, the energy transfer rate, $\varepsilon(r)$, with clockwise forcing at 2.25 Hz (+675 rpm), is provided in figure VII.8. It should be noted that $\varepsilon(D_{LLL})$ shows more scattering than $\varepsilon(D_{LL})$ and $\varepsilon(D_{NN})$.

Figure VII.10 shows the energy dissipation rate for the experiments we performed. The energy dissipation rate, ε, computed from the small measurement volumes were approximately 30% of their counterparts acquired using the big observation volume. We found random forcing to be slightly more efficient than clockwise forcing at 1.66 Hz (+500 rpm), and forcing at −9.33 Hz (−2800 rpm) to be less efficient than the propeller speed of +9.33 Hz (+2800 rpm).

To test whether the differences between small and big observation volume runs are not due to the subtraction of the mean flow field, we calculated the Eulerian second and third order structure functions without prior subtraction of the mean flow. As an example, the energy transfer rate, ε, with clockwise forcing at 2.25 Hz (+675 rpm) (bMV) is displayed in figure VII.9. The second order structure functions are in good aggrement, whereas the third order structure function differs for separation distances bigger than approximately 200 η. The fact that the differences are small is additional evidence that the mean velocity field is negligible compared to the turbulent fluctuations, and that the difference in the results between the large and small observation volume runs is not due to the subtraction of the mean flow field.

[2] The equations are $\varepsilon(r) \approx \left(\frac{D_{LL}}{C_2} \right)^{3/2} \frac{1}{r} = \left(\frac{3\, D_{NN}}{4\, C_2} \right)^{3/2} \frac{1}{r}$ and $D_{LLL}(r,t) = -\frac{4}{5} \varepsilon\, r$.

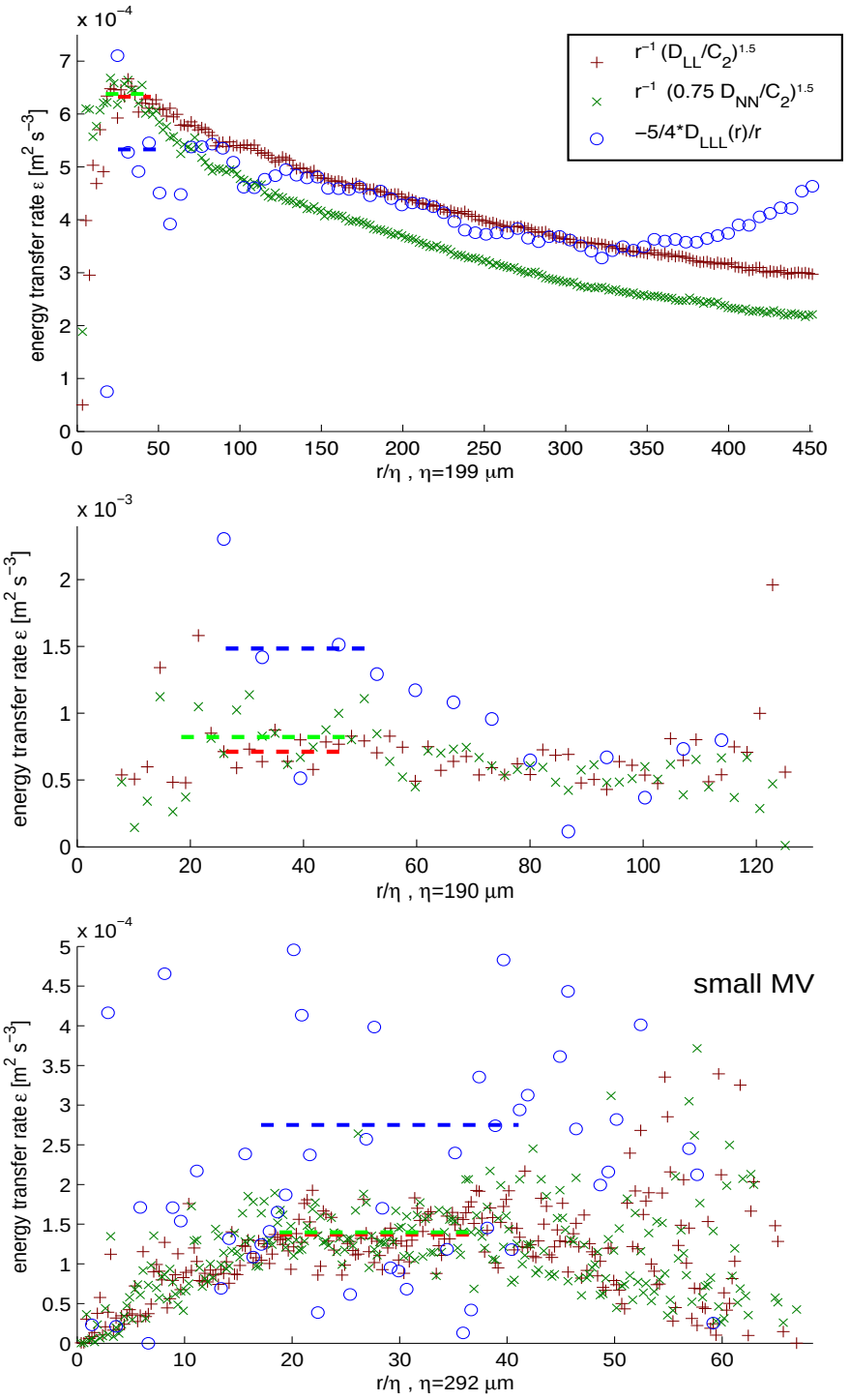

Figure VII.8: Energy transfer rate $\varepsilon(r)$ at forcing with 2.25 Hz (+675 rpm). Figure above: Energy transfer rate ε computed from the Eulerian structure functions at 2.25 Hz (bMV) forcing; figure in the middle: only points falling within a sphere with radius 1.2 cm where used for the calculation; the figure at the bottom: Energy transfer rate ε computed from the Eulerian structure functions for the same forcing but with the small measurement volume. The size of the small measurement volume is comparable to the size of the sphere. Although the forcing is the same, ε in the small measurement volume is approximately 30% of the value in the big measurement volume. However, the conditioned data (figure in the middle) does not show this behavior.

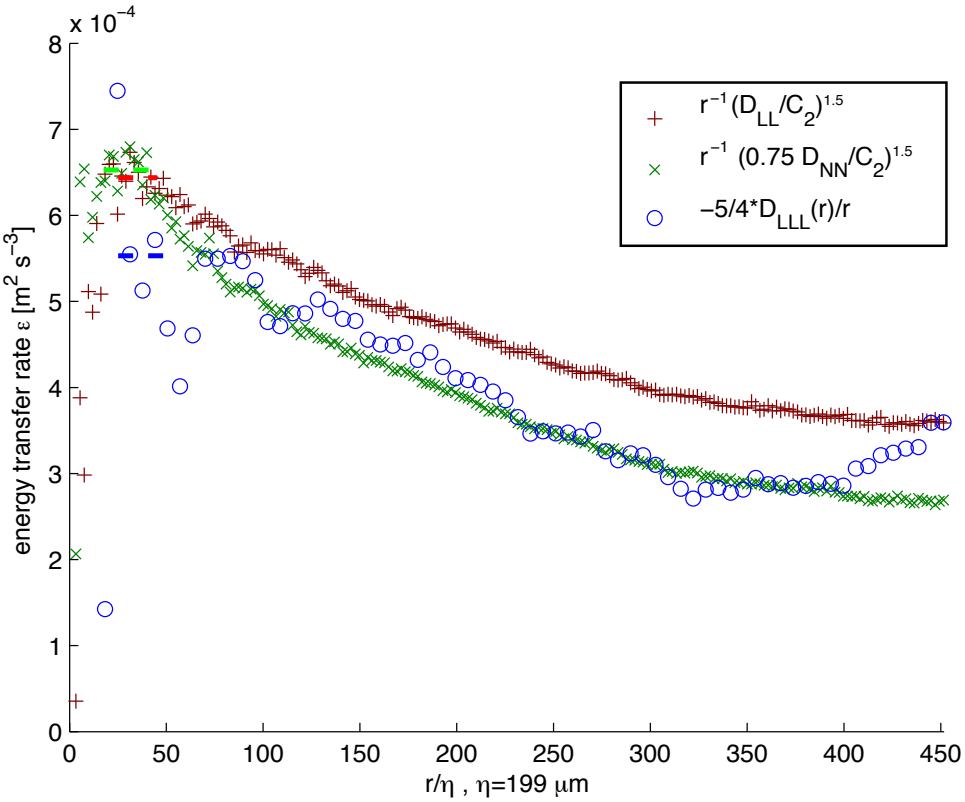

Figure VII.9: $\varepsilon(r)$ at forcing with 2.25 Hz (+675 rpm) without subtracting the mean flow. The energy transfer rate computed from the second order structure function are comparable to the figure VII.8. $\varepsilon(D_{LLL})$ is more affected by the mean flow field, but for separation distances up to 200 η still comparable. Thus, the difference between small measurement volume runs and big measurement volume runs is not due to the subtraction of the mean flow. Furthermore, it shows that the mean flow is small compared to the turbulent fluctuations in velocity.

Scaling of the energy transfer rate and the Kolmogorov scales

In order to verify that the data are reasonable, we consider the scaling of the energy transfer rate and the Kolmogorov scales with the forcing frequency. According to equation[3] (III.22) and the observation that $u' \propto f$,

$$\varepsilon \propto f^3 \tag{VII.4}$$

Therefore, the energy transfer rate should scale with the frequency as a power law with exponent 3. The two dashed lines in figure VII.10 are power law fits to the clockwise forcing data. Both the experiments in the big and the small observation volume show the predicted power law scaling for clockwise forcing. Because the clockwise forcing in both the big and the small observation volumes showed the predicted scaling it is not possible to falsify one. However, we can not explain the

[3] It is $\varepsilon \approx \frac{u'^3}{L}$

difference between the two. It is planned to perform additional experiments to verify to difference between the two observation volume runs.

Figures VII.12 and VII.11 show the Kolmogorov time and length scales. According to the equations (III.25) and (III.23), they scale as

$$\eta \propto \varepsilon^{-1/4} \quad \Rightarrow \quad \eta \propto f^{-3/4} \tag{VII.5}$$

and

$$\tau_\eta \propto \varepsilon^{-1/2} \quad \Rightarrow \quad \tau_\eta \propto f^{-3/2} \tag{VII.6}$$

respectively. In both cases, we found good agreement between our measurements and the prediction.

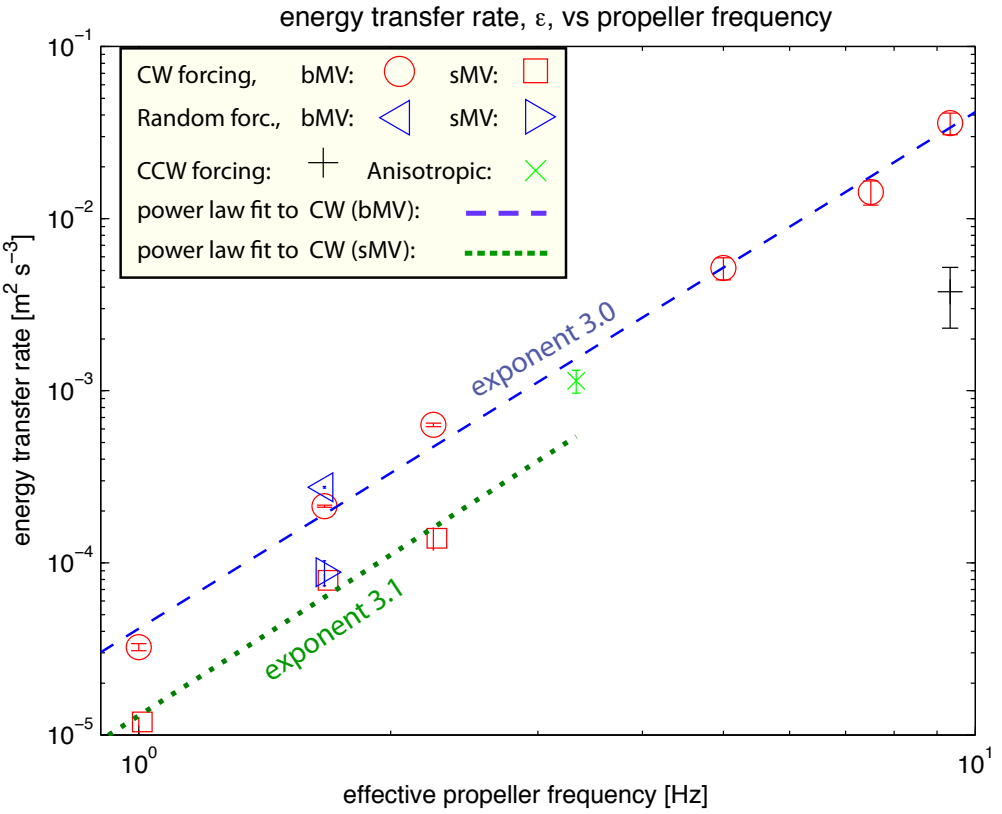

Figure VII.10: Energy transfer rate ε versus motor frequency. ε was independently calculated from D_{LL} , D_{NN} and D_{LLL} using equations (III.39) and (III.42). The two lines show power-law fits to the CW forcing data of the big and the small observation volume runs. In both case we found that $\varepsilon \propto f^3$. That is in good agreement with $f \propto u'$ and $\varepsilon \propto u'^3$. The energy dissipation rate in the small measurement volume experiment is significantly smaller than for the big measurement volume runs.

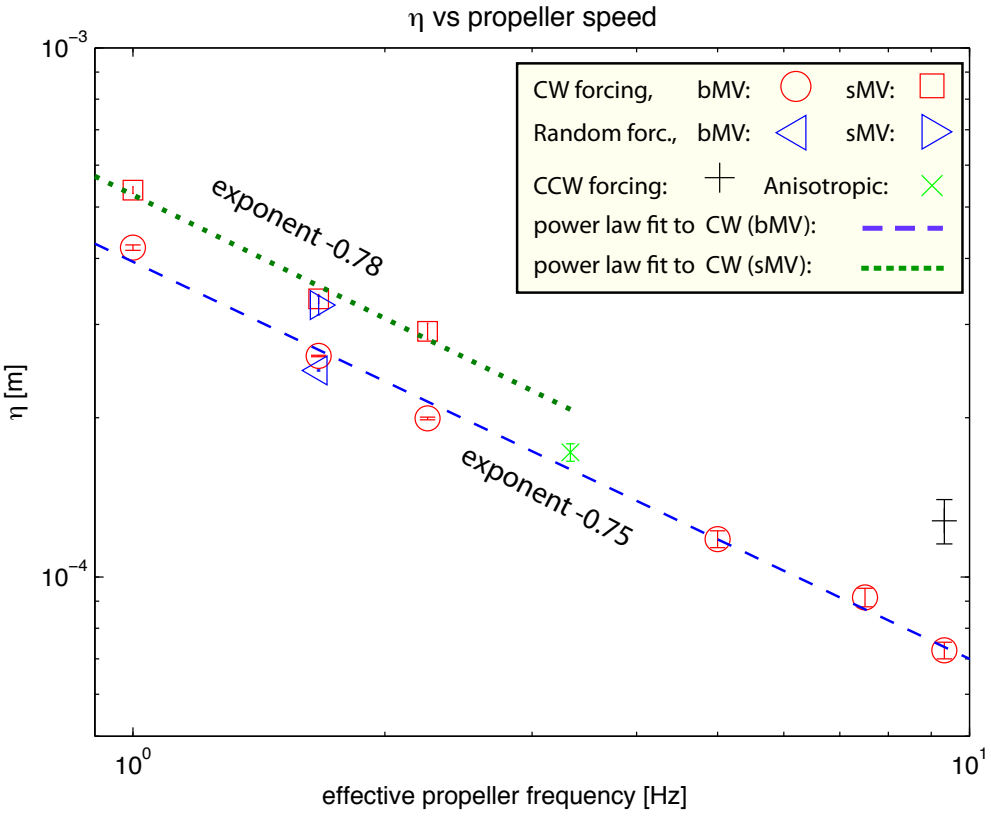

Figure VII.11: Kolmogrov length scale η versus motor frequency. η was calculated from the energy transfer rate ε shown in figure VII.10. Because it is $\eta \propto \varepsilon^{-1/4}$ and $\varepsilon \propto f^3$, η should scale with $f^{-0.75}$. The two dashed lines shows power law fits to the clockwise forcing data. The observed scaling is in good agreement with the prediction.

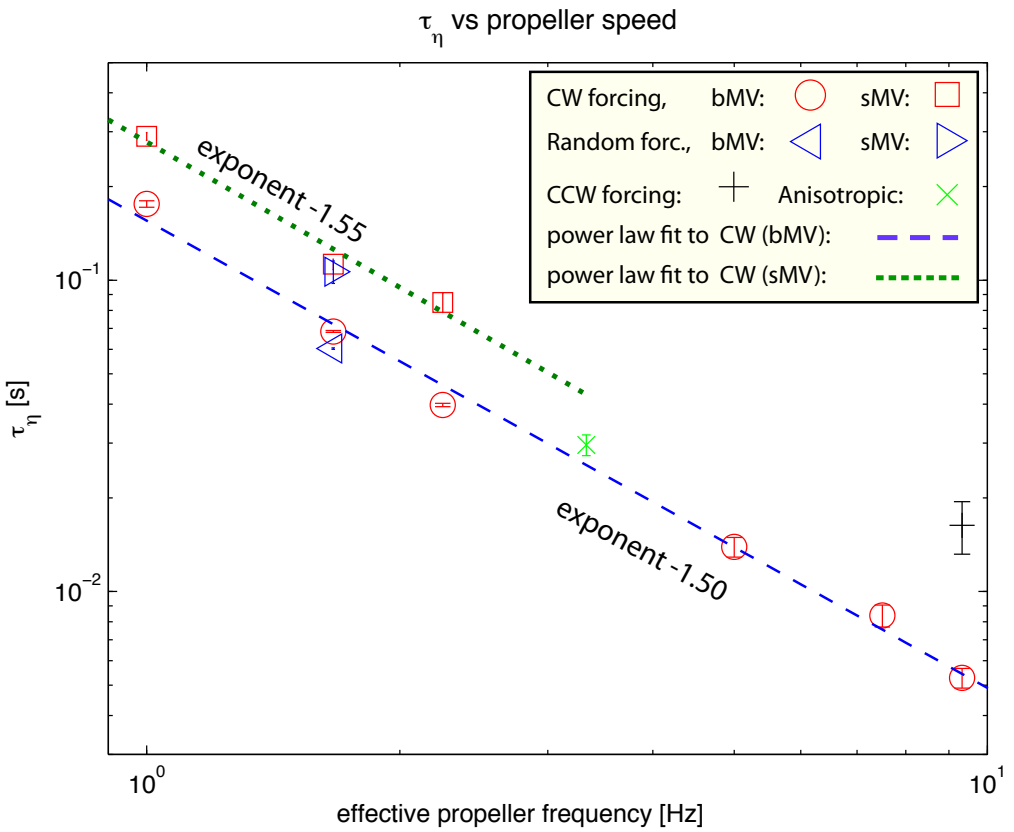

Figure VII.12: Kolmogrov time scale τ_η versus motor frequency. τ_η was calculated from the energy transfer rate ε shown in figure VII.10. Because it is $\tau_\eta \propto \varepsilon^{-1/4}$ and $\varepsilon \propto f^3$, τ_η should scale with $f^{-1.5}$. The two dashed lines shows power law fits to the clockwise forcing data. The observed scaling is in good agreement with the prediction.

Integral length scale and Reynolds number

In principle, it is possible to measure the integral length scale, L, using the Eulerian auto correlation and equation[4] III.47. However, since there is no analytical prediction for the autocorrelation functions, in order to make this measurement accurately, one would need a measurement volume with a size of several integral length scales. Since this condition is not satisfied in our experiment, we produce two estimates of the L. First, we estimate L using equation (III.22):

$$L \approx \frac{u'^3}{\varepsilon} \tag{VII.7}$$

Second, since the longitudinal Eulerian autocorrelation function, $f(r)$, showed an exponential decay over a region of several centimeter, we extrapolated the observed autocorrelation function using an exponential fit. We then estimate the L by integrating the exponential fit. The different values of the integral length scale are displayed in figure VII.13. In the big measurement volume the estimates of L from this second method were approximately 4 cm, and showed only a small dependence on the forcing. In comparison, the values from equation (VII.7) were a few times larger than the values obtained from $f(r)$. Note that the size of the big measurement volume is of the same order of magnitude as the integral length scale.

Equation (III.22) can be used to calculate the Taylor scale Reynolds number, R_λ:

$$R_\lambda = \sqrt{15\frac{u'\,L}{\nu}} = \left(\frac{15}{\nu}\right)^{1/2} \varepsilon^{-1/2}\, u'^2 \tag{VII.8}$$

Figure VII.14 shows the estimates of the Taylor scale Reynolds number. R_λ ranging from approximately 150 to 370 have been achieved. No prediction on the dependence of R_λ on the frequency can be made, unless we assume that the integral length scale is independent of frequency. In this case R_λ should scale with $f^{1/2}$, according to equations (VII.4) and (VII.3).

[4] $L_{LL} \equiv \int_0^\infty f(r,t)dr$

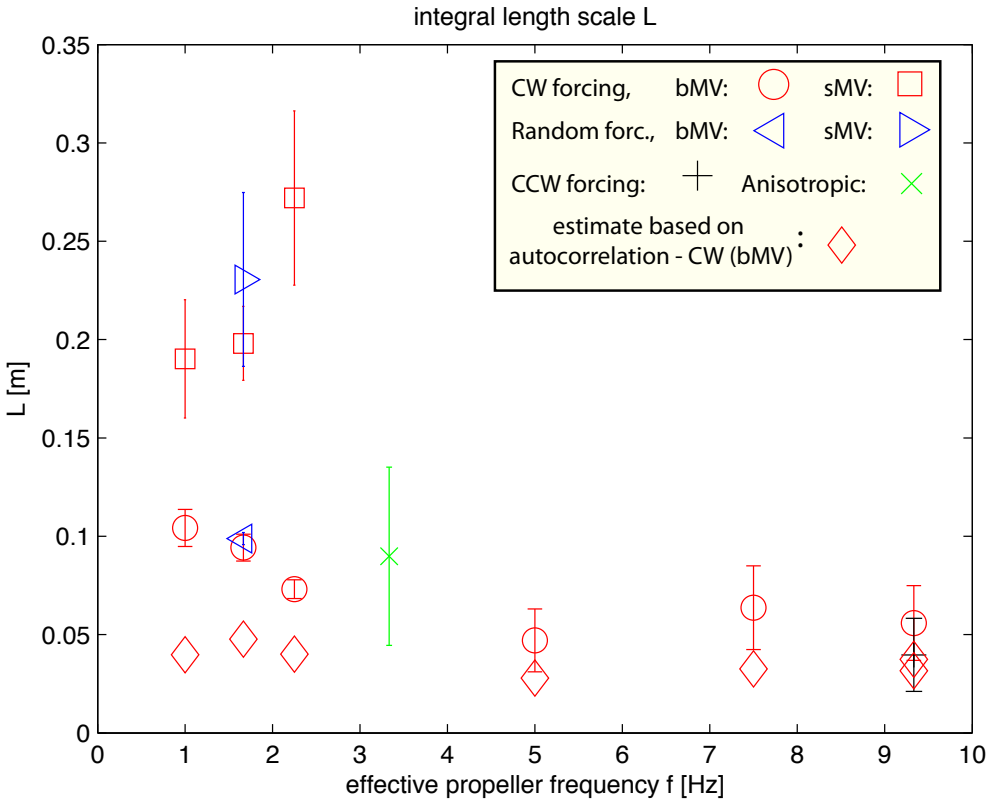

Figure VII.13: Integral length scale, L, versus motor frequency. L was calculated from the energy transfer rate, ε, and the fluctuating velocity, $\mathbf{u}'$. Because $L \propto \varepsilon^{-1}$ and the fact that energy transfer rate is smaller for the small measurement volume runs, the integral length scale of these experiments is bigger. The integral length scale is on the order of magnitude of 10 cm. This is comparable to the size of the big measurement volume.

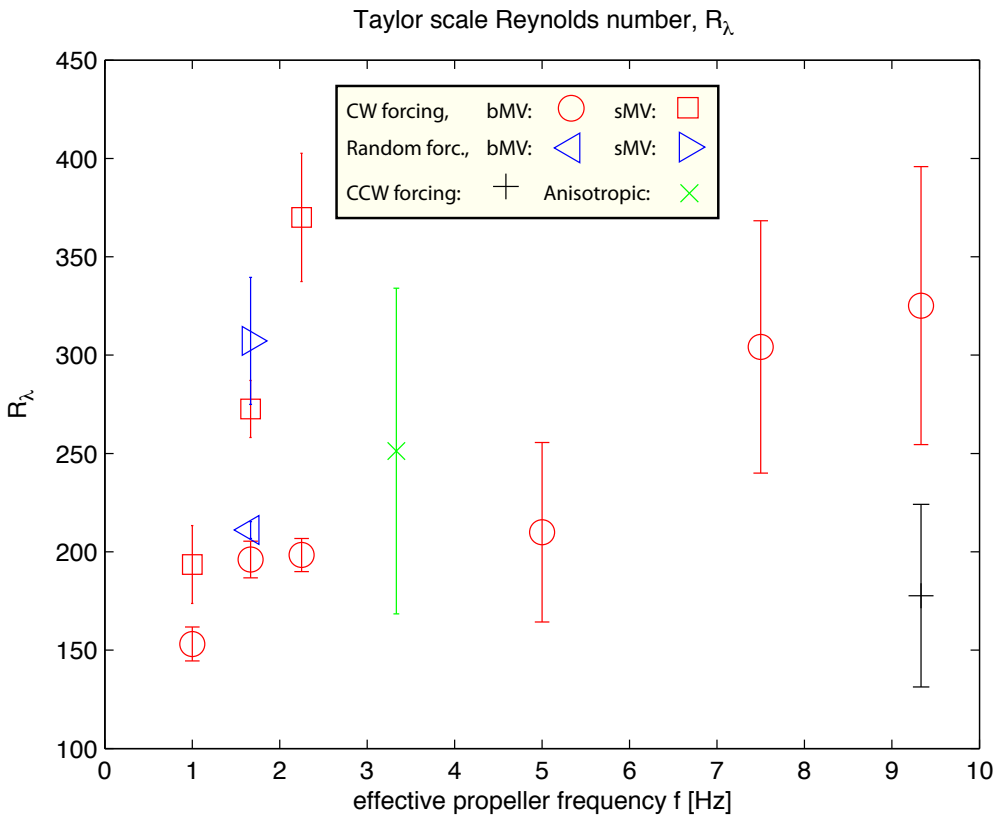

Figure VII.14: Taylor scale Reynolds number, R_λ, versus motor frequency. R_λ was calculated from the energy transfer rate, ε and the fluctuating velocity, $\mathbf{u}'$. The experiments covered a range from $R_\lambda = 150$ to 370. Forcing at higher propeller speed should enable us to reach $R_\lambda \approx 500$.

Summary

Tables VII.1 and VII.2 provide a summary of the basic properties of the apparatus at different forcing frequencies. σ_ε and the standard deviation in the components of $\mathbf{u}'$ were used to estimate the errors of the listed measures.

The flow of the Lagrangian Exploration Module is close to isotropic and the turbulent fluctuations are three to ten times stronger than the mean flow. For propeller frequencies below 9.33 Hz (1000 rpm), the mean velocity field is close to uniform and the mean flow is on the order of a $\frac{mm}{s}$. Thus, the flow is homogenous in this regime. Moreover, the energy transfer rate, as well as the Kolmogorov scales, measured for the big observation volume follow the predicted power laws. In addition, the size of the big measurement volume is comparable to the integral length scale of the flow. However, we observe that the energy transfer rate measured in the small observation volume is significantly smaller than in the big measurement volume. This is problematic since we only changed the method of making measurements, and we could not find a way to invalidatet one data set. Therefore, it is planned to perform additional experiments to explore the difference between the two observation volume runs.

Further investigations of the properties of the apparatus are provided in the following sections.

Table VII.1: Energy transfer rate and Kolmogorov scales of the performed experiments

	speed at propeller $[Hz]$	speed at motor $[rpm]$	ε $[m^2 \cdot s^{-3}]$	η $[\mu m]$	τ_η $[ms]$	R_λ	St
bMV	+1	300	$(3.24 \pm 0.15) \cdot 10^{-5}$	420 ± 5	175 ± 4	150 ± 10	$4 \cdot 10^{-3}$
	+1.66	500	$(2.14 \pm 0.03) \cdot 10^{-4}$	261 ± 1	68 ± 0.5	195 ± 10	$1.0 \cdot 10^{-2}$
	+2.25	675	$(6.3 \pm 0.1) \cdot 10^{-4}$	200 ± 2	40 ± 1	200 ± 10	$1.7 \cdot 10^{-2}$
	+5	1500	$(5.2 \pm 0.75) \cdot 10^{-3}$	120 ± 4	14 ± 1	210 ± 45	$4.9 \cdot 10^{-2}$
	+7.5	2250	$(1.4 \pm 0.2) \cdot 10^{-2}$	91 ± 4	8.4 ± 0.6	300 ± 60	$8.5 \cdot 10^{-2}$
	+9.33	2800	$(3.6 \pm 0.5) \cdot 10^{-2}$	73 ± 3	5.3 ± 0.3	330 ± 70	$13 \cdot 10^{-2}$
	−9.33	−2800	$(3.8 \pm 1.4) \cdot 10^{-3}$	128 ± 13	16 ± 3	170 ± 45	$4.3 \cdot 10^{-2}$
sMV	+1	300	$(1.14 \pm 0.02) \cdot 10^{-5}$	540 ± 8	290 ± 8	190 ± 20	$5 \cdot 10^{-4}$
	+1.66	500	$(7.9 \pm 0.6) \cdot 10^{-5}$	335 ± 6	112 ± 5	270 ± 15	$1.4 \cdot 10^{-3}$
	+2.25	675	$(1.4 \pm 0.2) \cdot 10^{-4}$	290 ± 10	85 ± 6	370 ± 30	$1.8 \cdot 10^{-3}$
Anisotropic			$(1.14 \pm 0.17) \cdot 10^{-3}$	170 ± 7	30 ± 3	250 ± 80	$2.4 \cdot 10^{-2}$
Random (sMV)			$(8.5 \pm 1.5) \cdot 10^{-5}$	325 ± 14	105 ± 8	305 ± 30	$1.4 \cdot 10^{-3}$
Random (bMV)			$(2.74 \pm 0.03) \cdot 10^{-4}$	245 ± 1	60 ± 1	210 ± 5	$1.2 \cdot 10^{-2}$

Table VII.2: Integral length scale, L, and characteristic velocities of the performed experiments.

	speed at propeller $[Hz]$	speed at motor $[rpm]$	$\langle \mathbf{u} \rangle$ $[mm \cdot s^{-1}]$	$\mathbf{u}'$ $[cm \cdot s^{-1}]$	$\mathbf{h}$ $[cm \cdot s^{-1}]$	L $[cm]$
bMV	+1	300	$(-0.6\|-1.1\|+0.3)$	(1.45|1.54|1.50)	(0.2|0.2|0.2)	10 ± 1
	+1.66	500	$(-1.3\|-2.9\|+0.0)$	(2.72|2.80|2.64)	(0.2|0.2|0.2)	9 ± 1
	+2.25	675	$(-5.1\|-1.0\|-1.7)$	(3.61|3.49|3.66)	(0.4|0.4|0.5)	7 ± 1
	+5	1500	$(-4.6\|-8.4\|-2.8)$	(7.15|5.79|5.78)	(0.9|0.9|1.0)	5 ± 1
	+7.5	2250	$(-10.8\|-9.9\|-14.8)$	(11.0|8.8|9.2)	(1.7|1.7|2.2)	6 ± 2
	+9.33	2800	$(-18\|-4.2\|-11.9)$	(14.4|11.8|11.6)	(1.9|2.3|3.1)	6 ± 2
	−9.33	−2800	$(+8.2\|-9.9\|-9.8)$	(5.83|4.69|5.39)	(1.1|1.2|1.5)	4 ± 2
sMV	+1	300	$(-0.5\|-1.4\|-0.6)$	(1.40|1.27|1.26)	(0.1|0.1|0.1)	19 ± 3
	+1.66	500	$(-1.8\|-1.3\|-2.1)$	(2.53|2.54|2.44)	(0.1|0.2|0.1)	20 ± 2
	+2.25	675	$(-0.9\|-3.3\|-0.1)$	(3.47|3.33|3.26)	(0.2|0.2|0.1)	27 ± 5
Anisotropic			$(-3.1\|-2.0\|10)$	(4.86|3.69|5.50)	(0.8|0.8|1.2)	9 ± 5
Random (sMV)			$(\ 0.0\|-3.0\|\ 0.0)$	(2.82|2.76|2.61)	(0.2|0.2|0.1)	23 ± 5
Random (bMV)			$(-1.0\|-2.1\|+1.5)$	(2.98|3.05|2.99)	(0.2|0.2|0.3)	10 ± 1

VII.4 Influence of the forcing

The LEM provides twelve propellers which can be controlled independently. It is worthwhile to investigate the influence of the forcing on the flow. As discussed in section VII.1 four types forcing were chosen to be tested. However, the quality of the data obtained only allows a detailed comparison between forcing at 1.66 Hz (+500 rpm) and random forcing in the big observation volume.

The random forcing was designed to ensure a constant energy injection rate. Since $u' \propto f$ (equation (VII.3)) and $\varepsilon \propto u'^3$ (equation (VII.4)), we enforced

$$\frac{1}{12}\sum_{i=1}^{12} f_i^3 = f^3 = (500\ rpm)^3 \quad \text{with } f_i \in [300\ rpm; 700\ rpm] \tag{VII.9}$$

where f_i is the frequency of the $i-$th motor. Every 30 seconds new frequencies were randomly chosen. This time step is of the order of ten eddy turnover times.

VII.4.1 Isotropy and homogeneity

One way to test the isotropy and homogeneity of the flow is provided by the Eulerian autocorrelation. Equation[5] (III.46) had been derived assuming an isotropic and

[5] $g(r) = f(r) + \frac{r}{2}\left(\frac{\partial}{\partial r} f(r)\right)$

homogeneous flow.

$$\begin{aligned} & g(r) = f(r) + \frac{r}{2}\left(\frac{\partial}{\partial r} f(r)\right) = \frac{1}{2\,r}\frac{\partial}{\partial r}\left(r^2\, f(r)\right) \\ \Leftrightarrow \quad & f(r) = \frac{2}{r^2}\int_0^r x\, g(x) dx \end{aligned} \tag{VII.10}$$

The rearranged equation enables us to compute a prediction of f from the measured g. With the help of a discrete differentiation of f, a prediction of g is also possible. However, the prediction of g is more effected by noise than the prediction of f. For easier reading the predictions are denoted f_{th} and g_{th}, whereas the measured functions are called f_{exp} and g_{exp}.

We did observe that both $\left|\frac{f_{th}-f_{exp}}{f_{exp}}\right|$ and $\left|\frac{g_{th}-g_{exp}}{g_{exp}}\right|$ differ less than 15% for separation distances smaller between 3 cm to 5 cm for clockwise forcing. As an example, the Eulerian autocorrelation at forcing with 2.25 Hz (+675 rpm) (bMV) is depicted in figure VII.15. Furthermore, figure VII.15 shows that f seems to follow an exponential decay law for $r < 9$ cm.

For further investigation on the isotropy, we plotted the dependence of the autocorrelation on the direction of the separation vector. With the help of spherical coordinates the direction, $\mathbf{e}_r$, was expressed as $\mathbf{e}_r = \begin{pmatrix} \phi \\ \theta \\ r = 1 \end{pmatrix}$. Figure VII.16 shows f and g for random forcing (bMV) conditioned on different values of ϕ and θ. Since the conditioned autocorrelation used less data than the total average, the first is more affected by measurement errors. However, both showed to be independent of the direction of the separation vector.

Thus, the flow shows good isotropy over ranges up to 8 cm. Again, this is on the order of the big measurement volume and also comparable to the integral length scale of the flow.

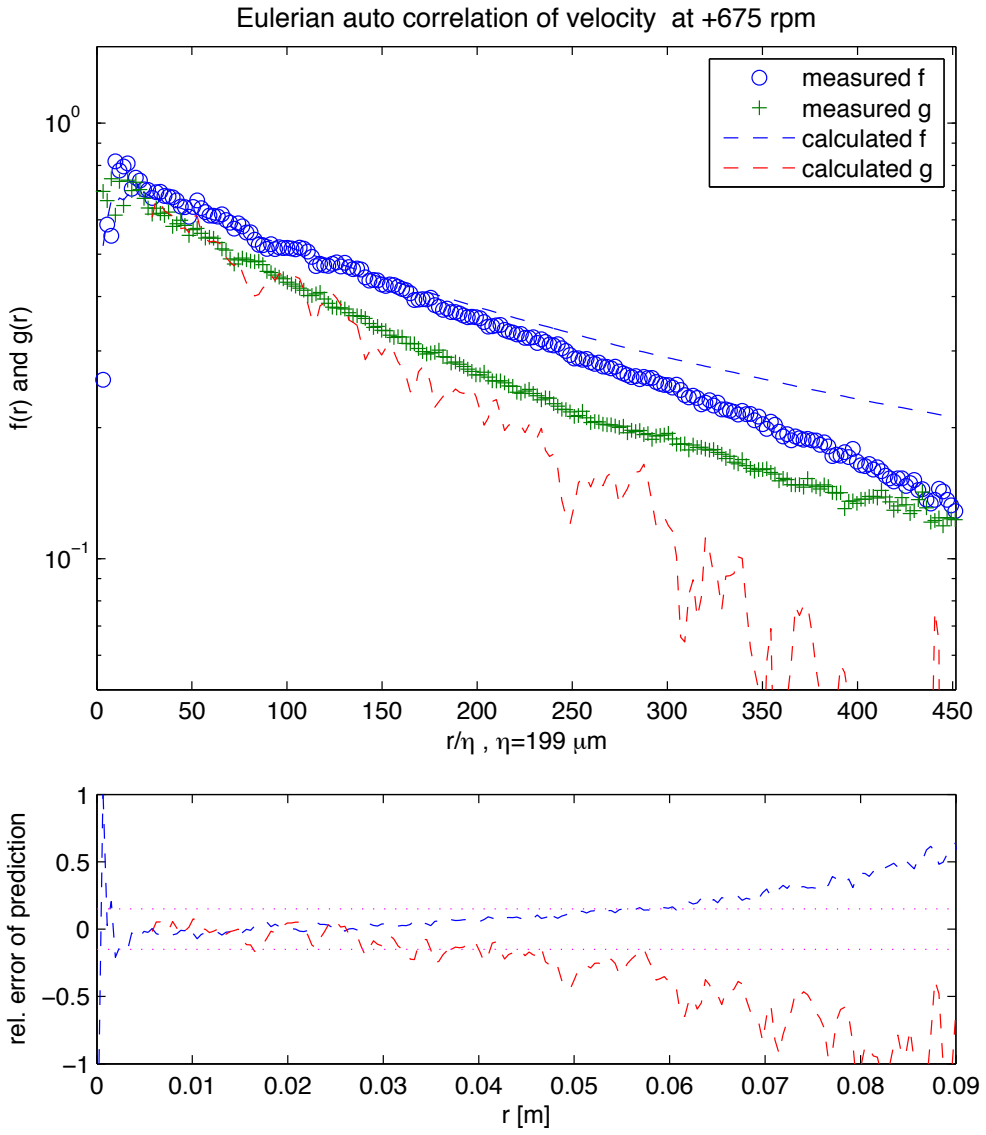

Figure VII.15: Eulerian autocorrelation at 2.25 Hz (+675 rpm) (bMV) forcing. The top figure shows the calculated and the measured autocorrelation curves f and g, whereas the figure at the bottom displays the relative deviation to the measured curves. The two dotted lines mark a region of $\pm 15\%$ deviation. Because the curves fall within these bounds up to separations distances of approximately 4 cm, the flow in this regime can be considered locally isotropic.

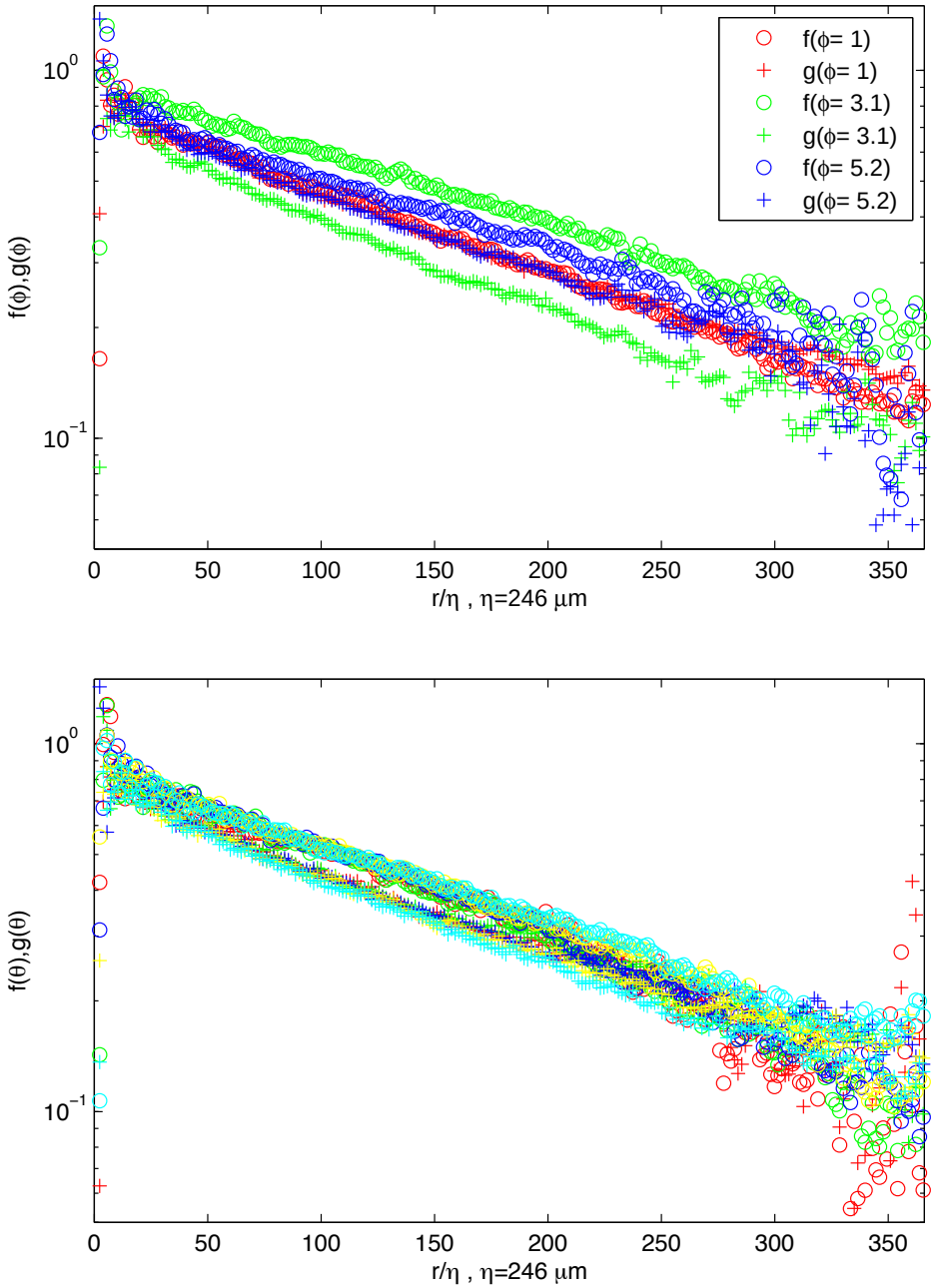

Figure VII.16: Eulerian autocorrelation conditioned on direction at random (bMV) forcing. The Eulerian autocorrelation was conditioned on the direction of the separation vector $\mathbf{r}$ in spherical coordinates (ϕ, θ). The top figure shows the dependence of f and g on ϕ, and the bottom figure plots the dependence of f and g on θ. In the latter figure, five bins for θ were used and the colors denote red: $\theta \in [1.37|1.57]$, green: $\theta \in [1.16|1.37]$, blue: $\theta \in [0.92|1.16]$, yellow: $\theta \in [0.64|0.92]$, cyan: $\theta \in [0|0.64]$. Differences between the curves are probably due to the reduced amount of used data points per curve. However, the Eulerian autocorrelation functions f and g are independent of the direction. Thus, the Lagrangian exploration module creates isotropic turbulence.

VII.4.2 Probability density functions

PDFs of velocity and acceleration were measured and compared. In good agreement with [29], the measured acceleration PDF from the big observation volume show the same shape as the acceleration PDF measured with the silicon strip detector experiment [31] in their French-Washing-Machine. Furthermore, we noticed that for the big measurement volume the shape of the acceleration PDF did not depend on the forcing. As an example, the acceleration PDF of +500 *rpm* in the big measurement volume is provided in gure VII.17.

However, the PDFs of velocity were not gaussian. Their shape is comparable to the axial velocity PDF obtained in a French-Washing machine [30]. Furthermore, we noted minor changes in the velocity PDF due to the forcing. Figure VII.19 and VII.18 display the velocity PDF of anisotropic forcing and 1 66 *Hz* (+500 *rpm*) forcing (bMV). In the anisotropic case, y and z component of the velocity distribution seem to follow PDF $(u \quad u) \sim \exp(\quad u \quad u \quad)$. The curves of the 1 66 *Hz* (+500 *rpm*) run are smoother.

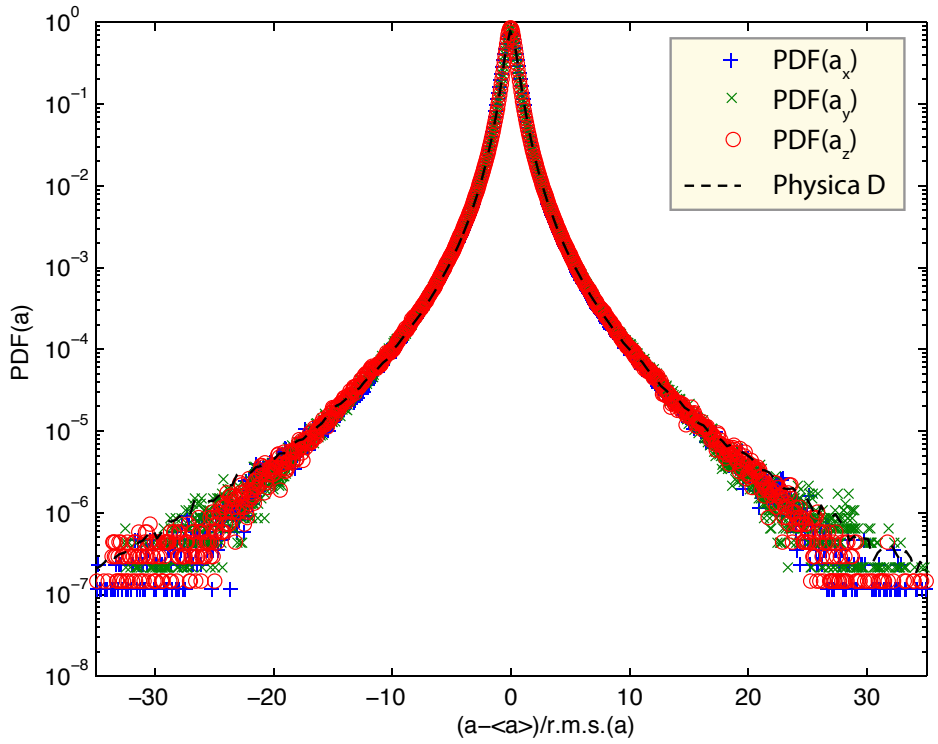

Figure VII.17: Probability density function of the acceleration at R 200. The curve was computed from data of the +1 66 *Hz* (+500 *rpm*) (bMV) run. The dashed curve is the acceleration PDF (R = 690) published in [29]. The less distinct tails of the acceleration in the LEM are probably due to the smaller temporal resolution used and the less intense turbulence level.

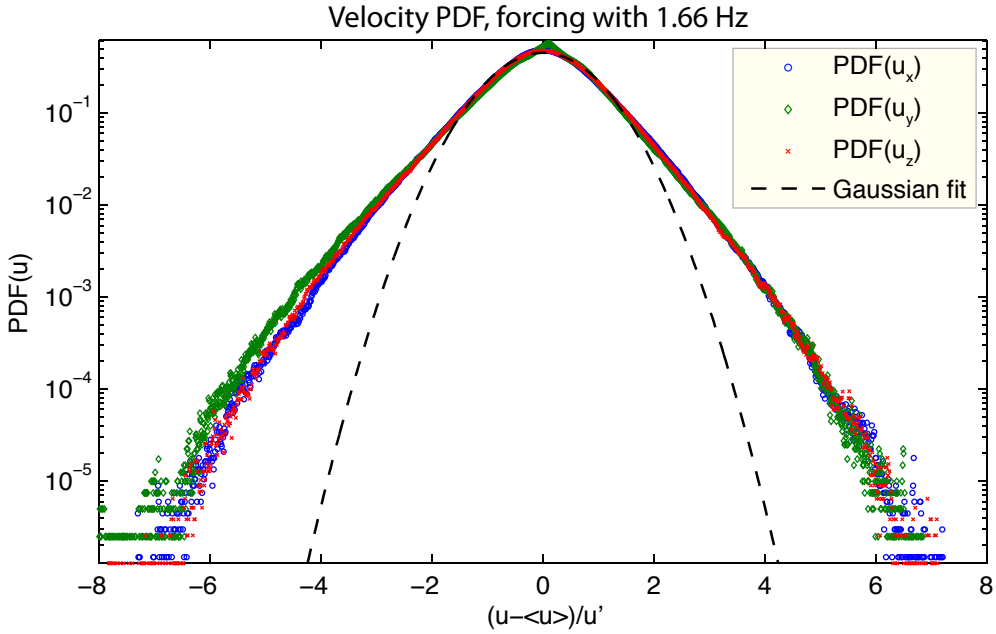

Figure VII.18: Probability density function of the velocity for the +500 *rpm* (bMV) run. The PDF of velocity is clearly not Gaussian. Unlike the velocity PDF of anisotropic forcing (see gure VII.19), the distribution at u u is smooth.

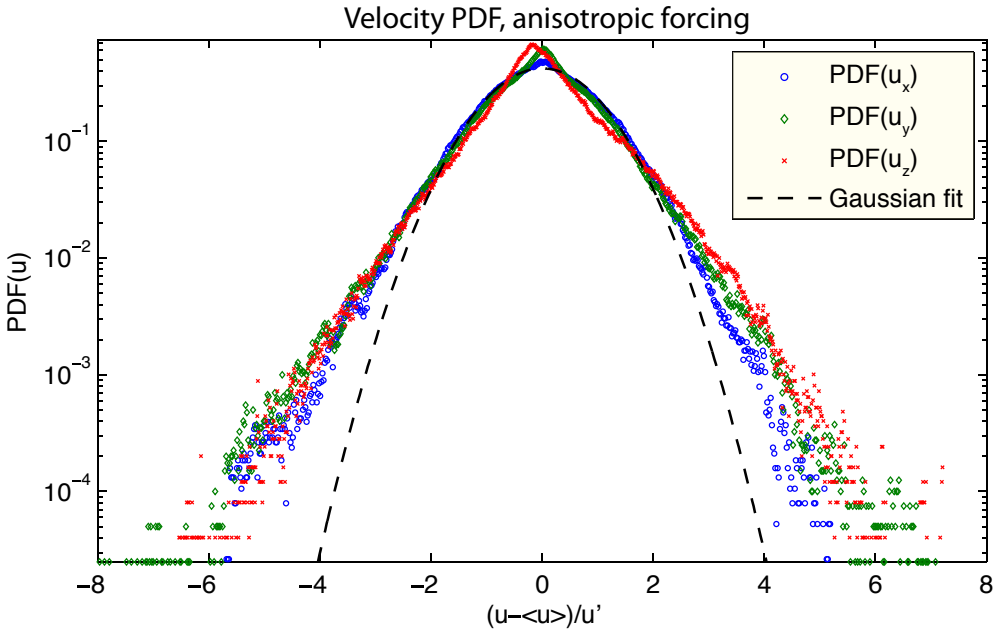

Figure VII.19: Probability density function of the velocity for the anisotropic run. No Gaussian velocity distribution was observed, the PDF of each velocity component shows a kink at the u . Moreover, y and z component of the velocity distribution seem to be proportional to exp(u u).

VII.4.3 Mean-flow field

The Eulerian mean velocity field has been measured as described in section VI.3. For small distances between $\mathbf{r}_0$ and $\mathbf{r}$ we can approximate the mean flow, $\mathbf{u}(\mathbf{r})$, as

$$\mathbf{u}(\mathbf{r}) \approx \mathbf{u}_0 + \underline{\underline{\mathbf{M}}}\,(\mathbf{r} - \mathbf{r}_0) \tag{VII.11}$$

where $\mathbf{u}_0$ is the zeroth order of the Taylor expansion[6] and $\underline{\underline{\mathbf{M}}}$ is the Jacobian[7], $\nabla\mathbf{u}(\mathbf{r}_0)$, of the velocity field at $\mathbf{r}_0$. The fitting procedure described in section VI.4 allows us to compute the Jacobian $\underline{\underline{\mathbf{M}}}$ and $\mathbf{u}_0$. All points lying within a sphere of radius 5 *cm*, which was located at the center of the measurement volume, were included in the fitting process.

The Jacobian contains two physical properties: the symmetric part of $\underline{\underline{\mathbf{M}}}$ is the rate of strain tensor

$$S_{ij} = \frac{1}{2}\left(\frac{\partial u_i}{\partial x_j} + \frac{\partial u_j}{\partial x_i}\right) \tag{VII.12}$$

whereas the antisymmetric part contains the rotation tensor

$$\Omega_{ij} = \frac{1}{2}\left(\frac{\partial u_i}{\partial x_j} - \frac{\partial u_j}{\partial x_i}\right) \tag{VII.13}$$

of the fluid.
$\sigma = \left(\ \sigma_1 \,\middle|\, \sigma_2 \,\middle|\, \sigma_3\ \right)$ denotes the three eigenvalues[8] of the rate of strain tensor $\underline{\underline{\mathbf{S}}}$. The continuity equation dictates

$$\sigma_1 + \sigma_2 + \sigma_3 = 0 \tag{VII.14}$$

Consequently, the rate of strain is fully described by two of its eigenvalues and their corresponding eigenvectors. We will use sorted eigenvalues, i.e.

$$\sigma_1 \geqslant \sigma_2 \geqslant \sigma_3 \tag{VII.15}$$

The local vorticity of the flow is defined as:

$$\omega = \begin{pmatrix} \omega_1 \\ \omega_2 \\ \omega_3 \end{pmatrix} = \nabla \times \mathbf{u} \tag{VII.16}$$

Expressing ω in terms of Ω_{ij} it is

$$\omega_1 = 2\,\Omega_{32}\ , \quad \omega_2 = 2\,\Omega_{13} \quad \text{and} \quad \omega_3 = 2\,\Omega_{21} \tag{VII.17}$$

A visualization of the mean flow field is provided in section VII.3 in figure VII.7.

[6] It is $\mathbf{u}_0 \approx \langle\mathbf{u}\rangle(\mathbf{r}_0)$.
[7] or velocity-gradient tensor
[8] In order to avoid confusion with the Taylor micro scale, σ instead of λ will be used to denote the eigenvalues of the rate of strain tensor.

Comparison between random and clockwise forcing

For the forcing at 1.66 Hz (+500 rpm) and random forcing (both big observation volume runs), we stored the mean flow field for each trajectory file. This enables us to investigate the rate of strain (σ_1 and σ_2), the local vorticity (ω_1, ω_2, ω_3) and $\mathbf{u}_0$ with respect to their evolution with increasing number of collected data points. Because the observation time is only a few seconds but the time to download (and process) the raw movies is several minutes, it is not meaningful to use the real time for investigating the evolution. Therefore and also because the averaging process depends only on the number of data points but not on real time, the number data points collected was chosen as a measure of time.

Figures VII.20, VII.21 and VII.22 show the convergence of the investigated properties for an increasing amount of collected data. The three plots show that all of the properties approach their mean value after approximately $2 \cdot 10^7$ data points. This corresponds to approximately 1 GB to 3 GB of raw data. After reaching this first point, they change much slower or settle.

In both experiments $\mathbf{u}_0$ differed from $\langle \mathbf{u} \rangle$[9] by less than $1 \frac{mm}{s}$ in each component. This corresponds to a spatial homogeneous flow within the sphere used in the fitting procedure.

We observe, that all the three eigenvalues of the rate of strain tensor are non-negliglibe. If one eigenvalue is negligible, this corresponds to a flow which is stretched in (exactly) one direction and contracted along (exactly) one direction perpendicular to the first. Thus, we observe a three-dimensional mean flow field and no two-dimensional flow pattern. Furthermore, we find that σ_2 and σ_3 are negative with both forcings.

The magnitude of the rate of strain VII.21 and the local vorticity VII.22 are both on the order of several $\frac{1}{100}\frac{1}{s}$; whereas random forcing results in a less rotating mean flow. Also we note that $\sigma_1(Random\ forcing) < \sigma_1(+500\ rpm\ forcing)$. However, the difference between the two is small.

It is also possible to measure the rate of strain, rotation and velocity by using the fitting method to determine the velocity gradient and $\mathbf{u}_0$ on a small subset of the data. We divided the time measured (characterized by the number of data points) into 50 consequent subsets which contain approximately the same amount of data points. Each subset corresponds to 1 to 2 hours of measurement time. They enable us to compare snapshots of the mean flow to the long time averaged flow field.

Figure VII.23 displays the short-time-averaged $|\mathbf{u}_0|$ for forcing with 1.66 Hz (+500 rpm) and random forcing. In both cases, $|\mathbf{u}_0|$ ranges from 2 to 10 $\frac{mm}{s}$, which is several times bigger than its corresponding value obtained from the long time averaged velocity field. The magnitude observed was the same for the two forcings.

The magnitude of the local vorticity, $|\omega|$, calculated from the short-time averaged velocity field, is provided in figure VII.24. The vorticity is between 0.05 and 0.25 $\frac{1}{s}$. That value, however, is several times bigger than $|\omega|$ obtained from the long time average of the Eulerian velocity field. The magnitude of the vorticity was

[9] calculated form the velocity PDFs

approximately the same for both ways of driving the flow. Thus, the behavior of $|\omega|$ is comparable to $|\mathbf{u}_0|$.

The short-time averaged eigenvalues of the rate of strain tensor are depicted in figure VII.25. The magnitude of the rate of strain is approximately two to three times bigger than the corresponding value of the long time averaged mean field. Surprisingly, the second eigenvalue[10], σ_2, of the rate of strain tensor fluctuates from close to zero to positive values. The σ_2 computed from the long time average velocity field showed $\sigma_2 < 0$. If σ_1 and σ_2 are positive then one can picture a sphere which is stretched to a pancake-like shape. Its volume does not change due to the continuity equation. If σ_2 and σ_3 are both negative, the sphere mentioned before would be deformed to cigar shaped body. It is worthwhile to note that Xu *et al* [32] observed that the instantaneous rate of strain tensor in intense turbulence shows to two positive eigenvalues.

For a better comparison, we provide $\frac{\sigma_2}{\sigma_1}$ and $\frac{\sigma_3}{\sigma_1}$ in figure VII.25. Although we observed that random forcing shows $\frac{\sigma_2}{\sigma_1} \approx \frac{\sigma_3}{\sigma_1}$ for the long time averaged mean flow field, we found $\left|\frac{\sigma_2}{\sigma_1}\right| \approx 0$ and consequently $\frac{\sigma_3}{\sigma_1} \approx -1$ in the case of short-time averaged measurements.

The short-time averaged velocity field shows no difference between forcing with $+1.66\ Hz$ ($+500\ rpm$) and random forcing. Thus, it is either not possible to determine differences between both forcings with the measurement techniques employed or the mean flow does not change for small perturbations to its creation. The latter would coincide with Kolmogorov idea that the turbulence is independent of the forcing and only depending on the energy transfer rate for small regions far away from the boundaries and singularities of the flow.

However, the long-time averaged velocity field reveals that random forcing creates a less rotating mean flow field. It could be that forcing with $+1.66\ Hz$ ($+500\ rpm$) creates a big, slowly rotating whirl in the LEM which is less pronounced with random forcing. For a further investigation of the Eulerian flow field, either particle tracking velocimetry with much higher seeding densities or tomo-PIV should be considered as possible measurement techniques. The use of tomo-PIV would enable us to measure the rate of strain and the vorticity with better accuracy at time intervals much shorter than the eddy-turn-over time, thus deeper insight in the difference between the two ways of driving the flow.

[10]The eigenvalues are sorted, i.e. $\sigma_1 \geqslant \sigma_2 \geqslant \sigma_3$. Thus, $\sigma_1 > 0$

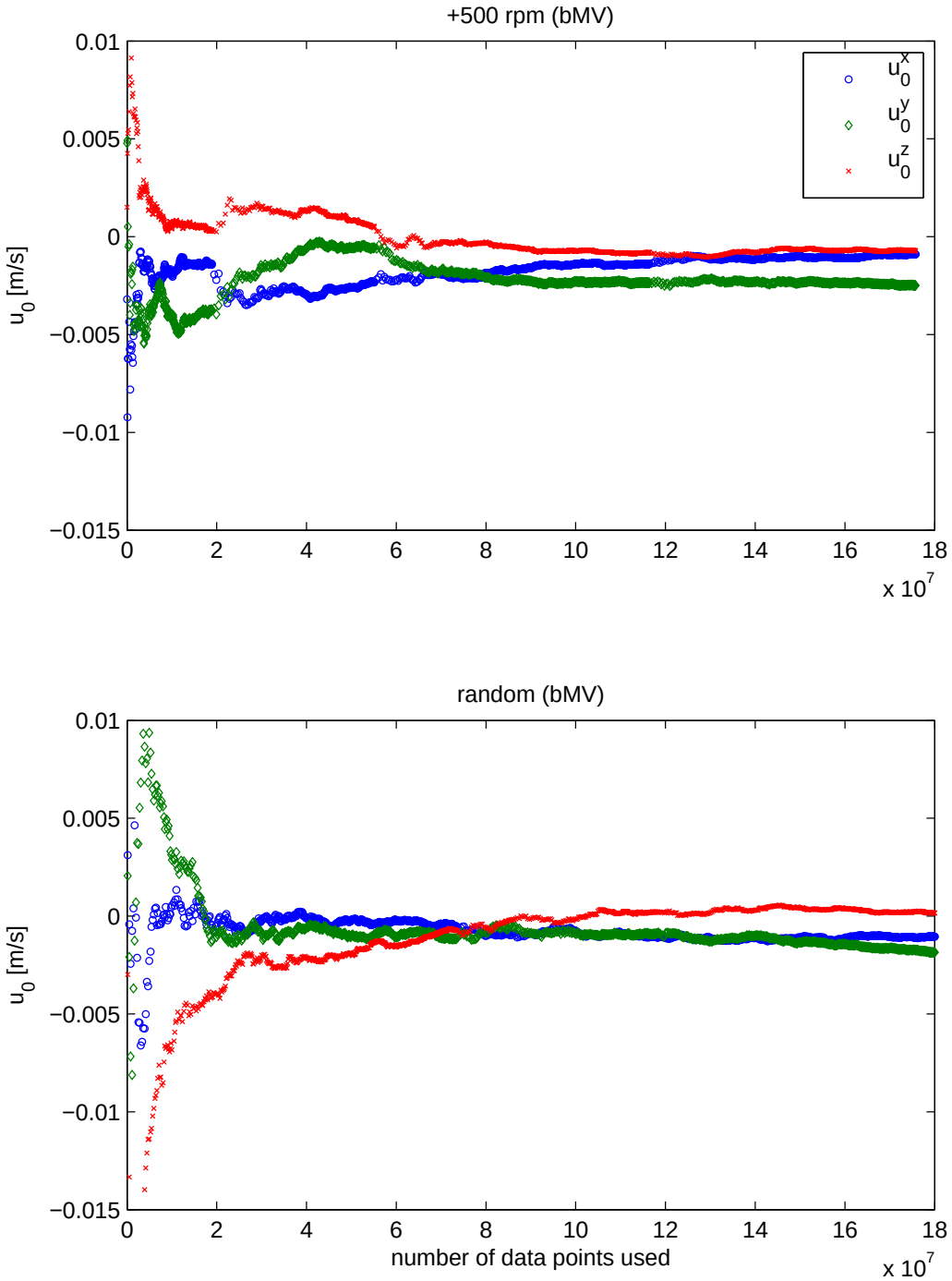

Figure VII.20: Evolution of $\mathbf{u}_0$ with the number data points measured. The velocity, $\mathbf{u}_0$, approaches its mean value after approximately $2 \cdot 10^7$ data points used. This corresponds to approximately 1 GB to 3 GB of raw data. After reaching this first point $\mathbf{u}_0$ changes much slower to a final velocity on the order of a $\frac{mm}{s}$. That value agrees well with the mean velocity obtained from the PDF of $\mathbf{u}$ (see section VII.3).

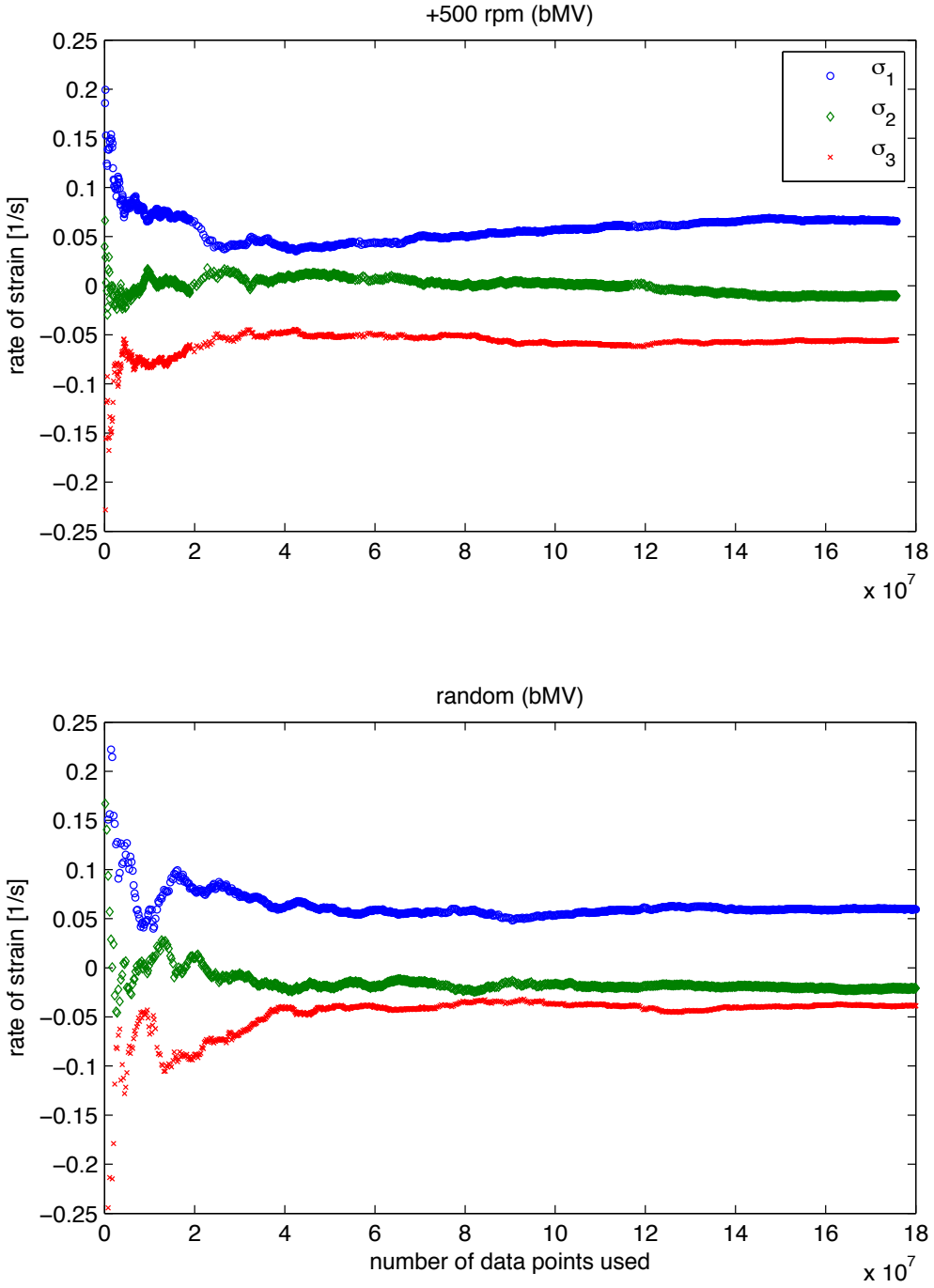

Figure VII.21: Evolution of rate of strain with the number data points measured. The rate of strain characterized by its eigenvalues $\sigma_1, \sigma_2, \sigma_3$, is approaching a value on the order a $\frac{1}{20\,s}$ for both random forcing and forcing with 1.66 Hz (+500 rpm). Also, σ_2 and σ_3 are both negative. However, random forcing creates a rate of strain tensor whose $\frac{\sigma_2}{\sigma_1}$ is comparable to $\frac{\sigma_3}{\sigma_1}$. In the case of forcing with 1.66 Hz (+500 rpm), $\left|\frac{\sigma_2}{\sigma_1}\right|$ is small compared to $\left|\frac{\sigma_3}{\sigma_1}\right|$. Thus, random forcing creates flow which stretched and compressed along three directions, whereas forcing with 1.66 Hz (+500 rpm) results in a flow which is stretched and compressed mainly along two directions. It should also be noted, that the curve change slower after approximately $3 \cdot 10^7$ data points used, which is in agreement with figure VII.20.

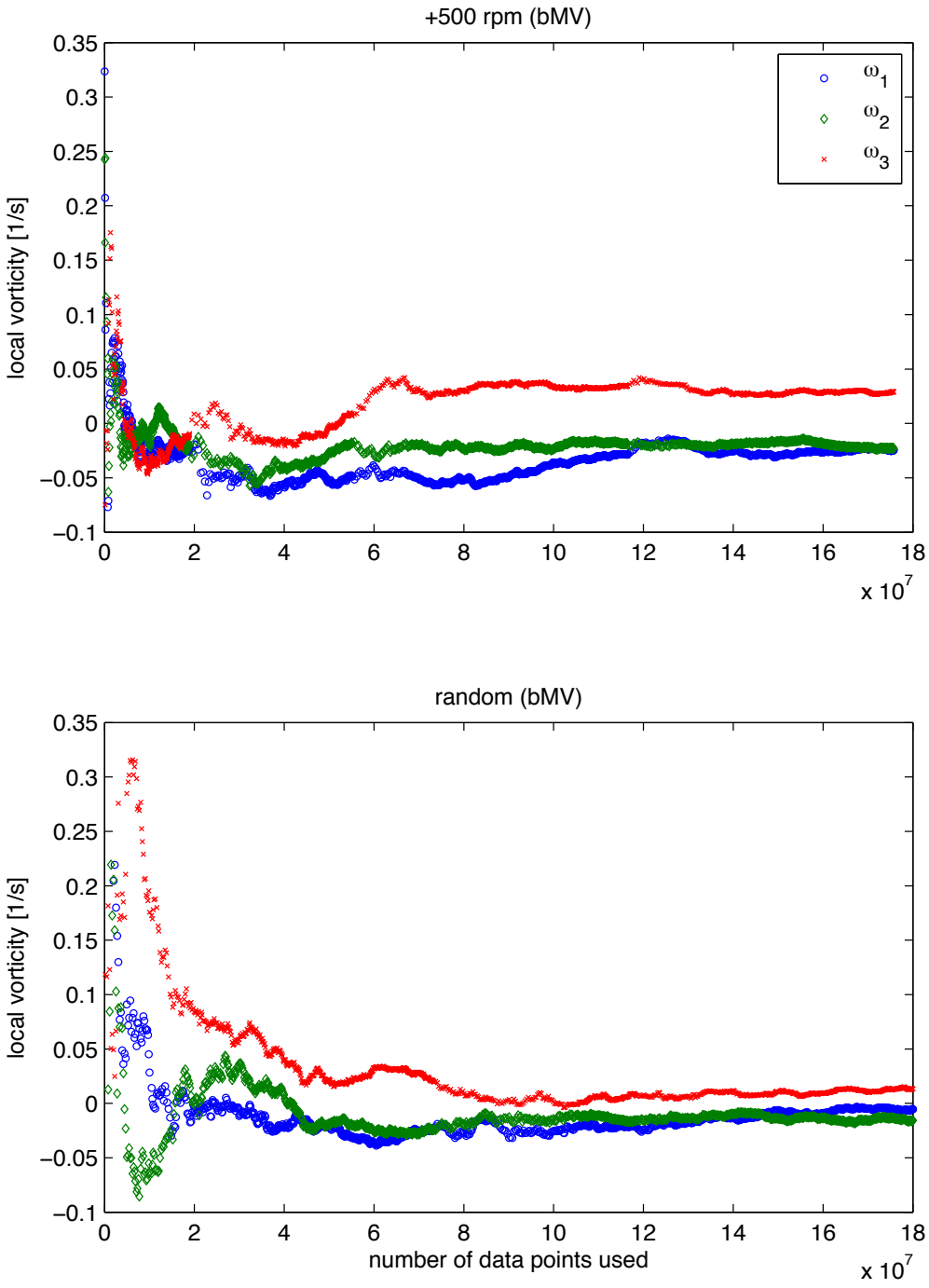

Figure VII.22: Evolution of the local vorticity with the number data points measured. The local vorticity, ω, is approaching a frequency on the order a few $\frac{1}{100}$Hz. Random forcing shows to produce more fluctuations in the local vorticity than forcing with 1.66 Hz (+500 rpm) if less than $8 \cdot 10^7$ data points were used. However, the average local vorticity is bigger for forcing with 1.66 Hz (+500 rpm). In other words, forcing at 1.66 Hz (+500 rpm) creates a more stable and pronounced rotating mean flow than random forcing.

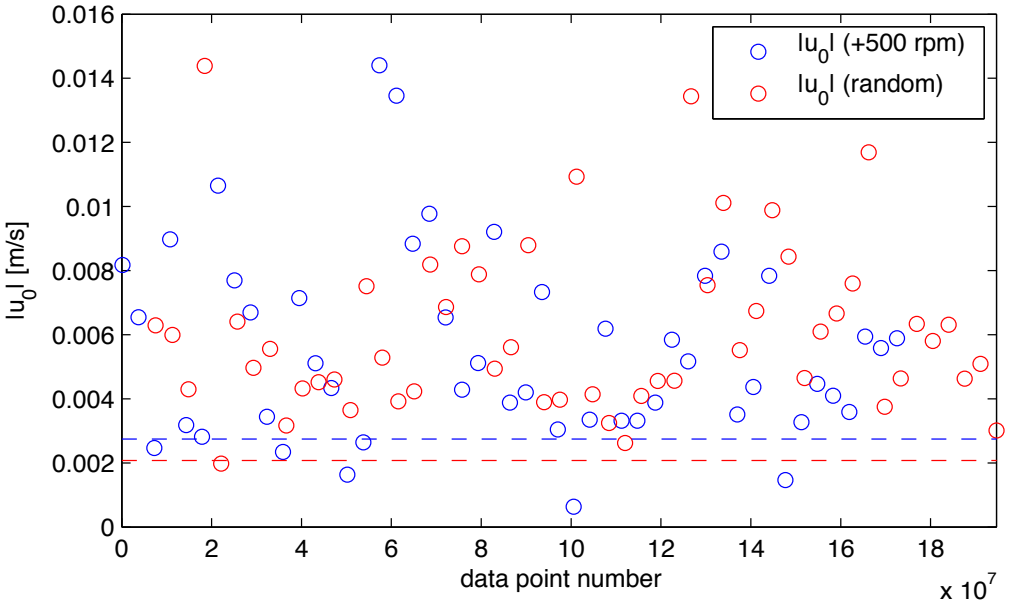

Figure VII.23: Magnitude of $\mathbf{u}_0$ obtained from the short-time averaged velocity field. The magnitude, $\|\mathbf{u}_0\|$, of the velocity computed from short-time averaged (or pseudo-instantaneous) Eulerian velocity field, is several times bigger than the corresponding value calculated from the long-time averaged flow field (see figure VII.20). The value of the long-time averaged flow field is indicated with the blue (forcing with 1.66 Hz (+500 rpm)) and red (random forcing) dashed lines. For both forcings, $\|\mathbf{u}_0\|$ is fluctuating between 2 and 10 $\frac{mm}{s}$, Also, no clear trend can be observed. That agrees with figure VII.24.

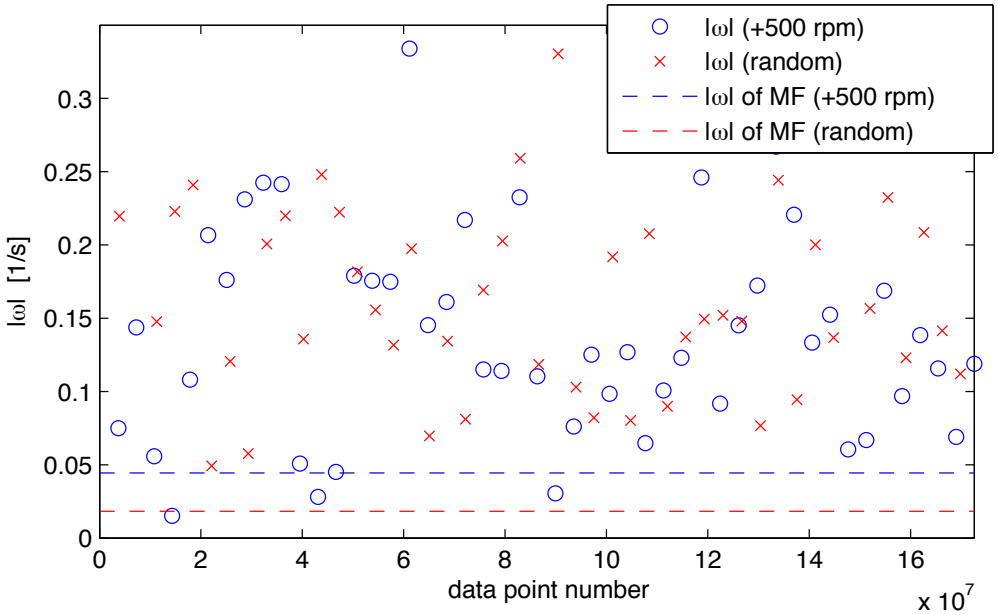

Figure VII.24: Magnitude of the local vorticity computed from the short-time averaged velocity field. The magnitude of the local vorticity, $\|\omega\|$, computed from short-time averaged Eulerian velocity field, is several times bigger than the corresponding value calculated from the long-time averaged flow field (see figure VII.22). The value of the long-time averaged flow field is indicated with the blue (forcing with 1.66 Hz (+500 rpm)) and red (random forcing) dashed lines. For both, random forcing and forcing with 1.66 Hz (+500 rpm), $\|\omega\|$ is fluctuating between 0.05 and 0.25 $\frac{1}{s}$. Moreover, no clear trend can be observed.

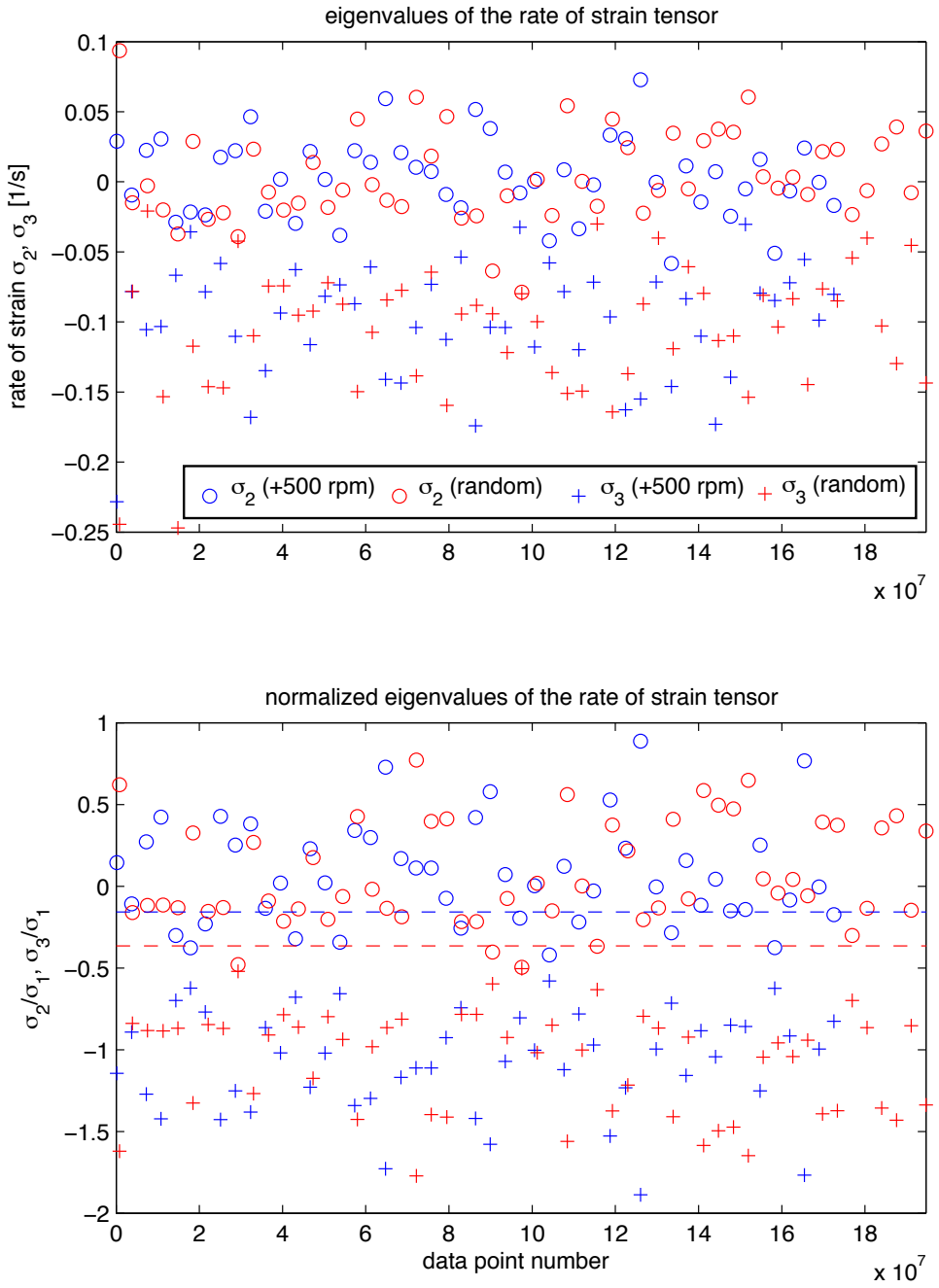

Figure VII.25: σ_2 and σ_3 of the rate of strain tensor computed from the short-time averaged velocity field. The top figure display the eigenvalues σ_2 and σ_3 of the rate of strain tensor computed from short-time averages of the Eulerian velocity field. Surprisingly, it is $\frac{\sigma_2}{\sigma_1} \gtrsim 0$ for both forcings. The long-time average did not show this (figure VII.21). The figure at the bottom displays σ_2 (◯) and σ_3 (+) normalized by σ_1 at random forcing (red) and forcing with 1.66 Hz (+500 rpm) (blue). The two dashed lines are the ratio of σ_2/σ_1 computed for the long-time averaged flow field. Clearly, the values of the short-time averaged mean flow deviate from their long-time average.

Timescale of the flow

Six dimensionless numbers quantities can be build with the rate of strain and the vorticity, which relate the change of the mean flow to the Kolmogorov time scale, the frequency of the propellers or the eddy turn over time[11], T:

$$A_{\tau,\sigma} \equiv \tau_\eta \cdot \max\left(\|\sigma_1\|, \|\sigma_3\|\right) \tag{VII.18a}$$
$$A_{\tau,\omega} \equiv \tau_\eta \cdot \|\langle\omega\rangle\| \tag{VII.18b}$$
$$A_{f,\sigma} \equiv f^{-1} \cdot \max\left(\|\sigma_1\|, \|\sigma_3\|\right) \tag{VII.18c}$$
$$A_{f,\omega} \equiv f^{-1} \cdot \|\langle\omega\rangle\| \tag{VII.18d}$$
$$A_{T,\sigma} \equiv T \cdot \max\left(\|\sigma_1\|, \|\sigma_3\|\right) \tag{VII.18e}$$
$$A_{T,\omega} \equiv T \cdot \|\langle\omega\rangle\| \tag{VII.18f}$$

where f is the effective frequency of the propellers. If the mean flow is stationary, i.e. changing much slower than the characteristic time scale of the turbulent fluctuations, $A_{\tau,\omega}$ and $A_{\tau,\sigma}$ are much smaller than unity. Furthermore, the idea of scale separation yields that A_ω and A_σ should decrease with higher Reynolds numbers.

If $A_{T,\sigma}$ and $A_{T,\omega}$ are much smaller than 1, then the mean-flow changes slowly compared to the time scale of the biggest eddies.

The dimensionless numbers, $A_{f,\sigma}$ and $A_{f,\omega}$, test if the time scale of the flow field is related to the propeller speed.

Figure VII.26 and table VII.3 show these six properties for the experiments performed. To determine the local vorticity and the rate of strain for the small measurement runs, the size of the fitting volume was set to 1.5 cm.

The mean flow charaterized by rate of strain, σ, and local vorticity, ω, changes 5 to 10 times slower than the eddy turn over time. Consequently, $A_{\tau,\sigma}$ and $A_{\tau,\omega}$, are ranging from 10^{-3} to 10^{-2}. In other words, the mean flow is changing a few hundred to one thousand times slower than the turbulent fluctuations characterized by the Kolmogorov time scale. We observe that the dimensionless numbers based on the Kolmogorov time scale decrease with an increase in motor speed (and thus also R_λ). This supports Kolmogorov's idea of scale separation, i.e. with intenser turbulence smaller Kolmogorov scales will be reached, whereas the big scales remain unchanged. However, this trend is small and probably within the uncertainty of $A_{\tau,\sigma}$ and $A_{\tau,\omega}$.

The parameters based on propeller speed and rate of strain and vorticity are approximately $\frac{1}{10}$ but not unity. Therefore, the timescale of the mean flow is not on the order of the propeller speed. Moreover, $A_{f,\sigma}$ and $A_{f,\omega}$, change only little with the frequency of the propellers. More measurements with a higher accuracy would be needed to provide a better description.

In general, we noted that random forcing (bMV) creates a less rotating flow than the other forcings investigated.

[11] The eddy turn over time is the characteristic time scale of the biggest eddies, and defined as $T \equiv \frac{L}{u'}$

Table VII.3: Time scales of the mean flow compared to the Kolmogorov time scale τ_η, the eddy-turn-over time T and the effective propeller frequency, f.

	speed at propeller $[Hz]$	motor $[rpm]$	$A_{\tau,\sigma}$	$A_{\tau,\omega}$	$A_{f,\sigma}$	$A_{f,\omega}$	$A_{T,\sigma}$	$A_{T,\omega}$
bMV	+1	300	$1 \cdot 10^{-2}$	$7 \cdot 10^{-3}$	$6.5 \cdot 10^{-2}$	$4.4 \cdot 10^{-2}$	0.46	0.30
	+1.66	500	$5 \cdot 10^{-3}$	$2 \cdot 10^{-3}$	$4.2 \cdot 10^{-2}$	$1.8 \cdot 10^{-2}$	0.24	0.10
	+2.25	675	$4 \cdot 10^{-3}$	$4 \cdot 10^{-3}$	$4.6 \cdot 10^{-2}$	$5.0 \cdot 10^{-2}$	0.21	0.23
	+5	1500	$3 \cdot 10^{-3}$	$4 \cdot 10^{-3}$	$4.4 \cdot 10^{-2}$	$6.2 \cdot 10^{-2}$	0.17	0.23
	+7.5	2250	$4 \cdot 10^{-3}$	$3 \cdot 10^{-3}$	$7.5 \cdot 10^{-2}$	$5.7 \cdot 10^{-2}$	0.37	0.28
	+9.33	2800	$4 \cdot 10^{-3}$	$3 \cdot 10^{-3}$	$9.0 \cdot 10^{-2}$	$5.9 \cdot 10^{-2}$	0.37	0.25
	−9.33	−2800	$1 \cdot 10^{-2}$	$3 \cdot 10^{-3}$	$7.7 \cdot 10^{-2}$	$2.2 \cdot 10^{-2}$	0.54	0.16
sMV	+1	300	$2 \cdot 10^{-2}$	$3 \cdot 10^{-2}$	$8.3 \cdot 10^{-2}$	$11 \cdot 10^{-2}$	1.2	1.7
	+1.66	500	$1 \cdot 10^{-2}$	$1 \cdot 10^{-2}$	$7.0 \cdot 10^{-2}$	$5.8 \cdot 10^{-2}$	0.9	0.8
	+2.25	675	$1 \cdot 10^{-2}$	$1 \cdot 10^{-2}$	$6.0 \cdot 10^{-2}$	$7.7 \cdot 10^{-2}$	1.1	1.4
Anisotropic			$2 \cdot 10^{-2}$	$8 \cdot 10^{-3}$	$1.8 \cdot 10^{-1}$	$8.0 \cdot 10^{-2}$	1.14	0.51
Random (sMV)			$1 \cdot 10^{-2}$	$1.1 \cdot 10^{-2}$	$8.8 \cdot 10^{-2}$	$7.8 \cdot 10^{-2}$	1.2	1.1
Random (bMV)			$3.7 \cdot 10^{-3}$	$1.2 \cdot 10^{-2}$	$4.9 \cdot 10^{-2}$	$0.9 \cdot 10^{-2}$	0.27	0.05

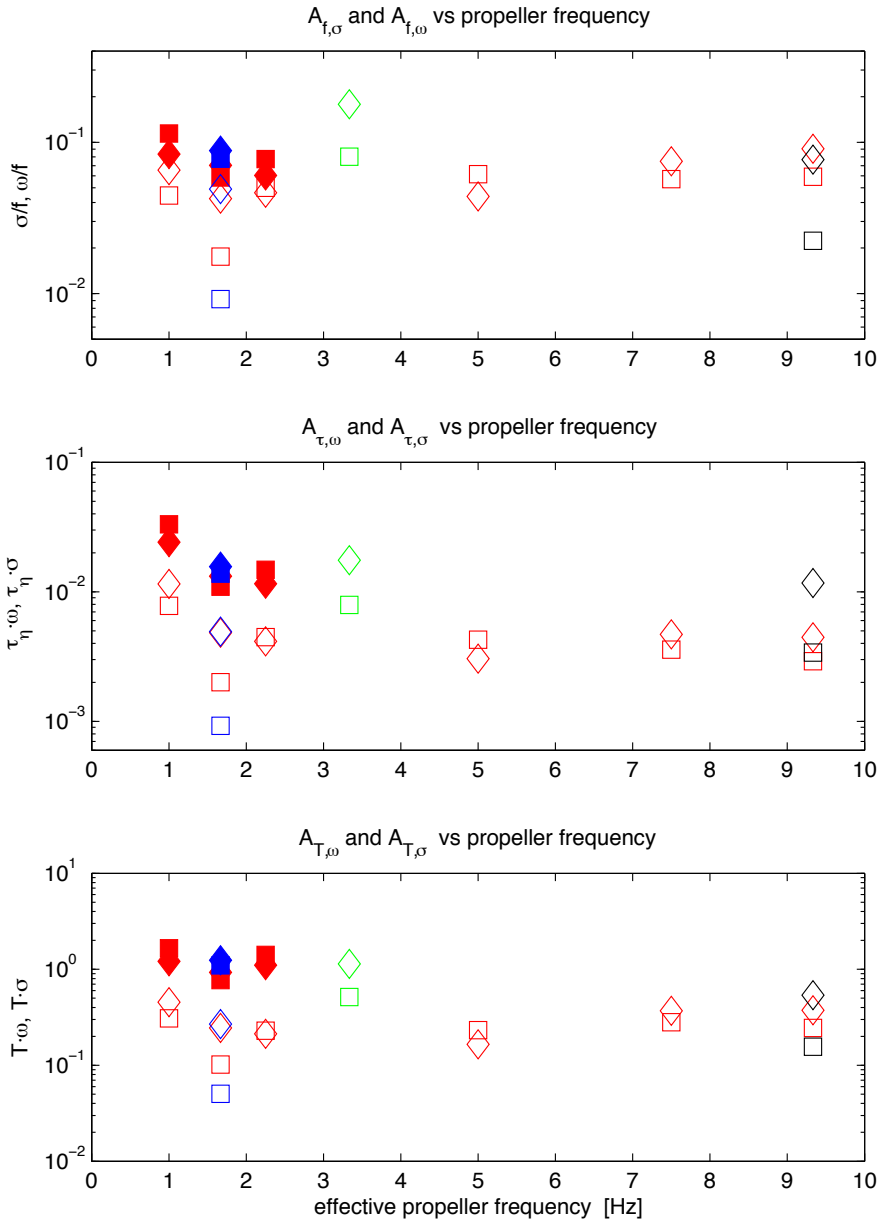

Figure VII.26: Dimensionless parameters $A_{\tau,\sigma}$, $A_{\tau,\omega}$, $A_{f,\sigma}$, $A_{f,\omega}$, $A_{T,\sigma}$, $A_{T,\omega}$ as a function of the propeller speed, f. The ♢ symbol refers to the dimensional parameter based on σ ($A_{\tau,\sigma}$, $A_{f,\sigma}$, $A_{T,\sigma}$), whereas □ denotes parameters based on ω ($A_{\tau,\omega}$, $A_{f,\omega}$, $A_{T,\omega}$). The colors denote: red: *CW* forcing, green: *anisotropic* forcing, blue: *random* forcing and black: *CCW* forcing. The small observation volume runs are marked with filled symbols.

The mean flow characterized by rate of strain, σ, and local vorticity, ω, changes 5 to 10 times slower than the eddy turn over time for the big observation runs. Consequently, it changes a few hundred times slower than the Kolmogorov time scale. Dimensionless numbers based on the Kolmogorov time scale decrease with an increase in propeller speed. This supports Kolmogorov's idea of scale separation. The parameters based on propeller speed and rate of strain or vorticity are constant at approximately $\frac{1}{100}$ but not unity. Therefore, the timescale of the mean flow is not on the order of the propeller speed. Random forcing creates a less rotating flow than the other forcing investigated.

VII.5 Lagrangian structure functions of position and velocity

The Lagrangian framework enables to obtain auto correlations and structure functions along a trajectory. Moreover, it is possible to investigate models which require precise data in this framework. This section will test predictions by Zybin *et al* in [1] and [33]. Reference [1] was later published in Physical Review Letters [34]. It should be noted, that the prediction on the scaling of the Lagrangian structure functions of position is not included in the P.R.L. publication.

Zybin and his group derived the shape of the PDF of vorticity inside a cylindrical vortex filament[12] in fully developed hydrodynamical turbulence [33]. They restricted the derivation to the inertial range of an incompressible fluid. Moreover, they assumed that the Euler equation (III.7) is sufficient to describe a trajectory in this regime.

A fluid segment or a particle will experience only small changes to its velocity in regions of low vorticity. Whereas, passing a vortex filament leads to fast oscillations of the position of the observed test particle. They claim that the latter contributes most to

$$K_n(\tau) = \langle |\mathbf{u}(t+\tau) - \mathbf{u}(t)|^n \rangle \tag{VII.19}$$

which is the n-th order Lagrangian structure function of velocity of a time difference τ. Assuming that the structure function follows a power law, one can define the (Lagrangian) scaling exponent ξ_n^L:

$$K_n \propto \tau^{\xi_n^L} \tag{VII.20}$$

Using the shape of the PDF of vorticity in such a filament, they were able to compute the scaling exponents, ξ_n^L, in the inertial range from a set of differential equations [34]. They compared these to results published by our group [35]. It should be noted, that K41 also predicts the behavior of the scaling exponents. The energy transfer rate has the unit $[m^2\, s^{-3}]$, thus K41 and dimensional arguments yield

$$K_n \propto (\varepsilon\, \tau)^{n/2} \quad \Rightarrow \quad \xi_n = \frac{n}{2} \tag{VII.21}$$

We measured the K_n up to the sixth order in the LEM for clockwise forcing at 1.66 Hz (+500 rpm) (bMV). They are displayed in figure VII.28.

Ouellette [30] proposed to define the Lagrangian inertial range as the region where K_2 scales linear with time. The definition becomes clear when focusing on the averaged Lagrangian structure function, K_n^{avg}, and their corresponding averaged energy transfer rate ε^{avg}:

$$K_n^{avg} = \frac{1}{N} \sum_{i=1}^{N} K_i \tag{VII.22a}$$

$$\varepsilon^{avg} = \frac{1}{N} \sum_{i=1}^{N} \varepsilon_i \tag{VII.22b}$$

[12] Vortex filaments are regions of high vorticity, they arise as eddies become stretched and advected from bigger eddies (see section III.4).

This definition is similar to equations[13] (III.59) and (III.60). Analogous to equation[14] (III.61) it is

$$\left(\frac{1}{N}\sum_{i=1}^{N}\varepsilon\right)^{n/2} = \frac{1}{N}\sum_{i=1}^{N}(\varepsilon_i)^{n/2} \tag{VII.23}$$

which holds only for the Lagrangian second order structure function. Although, $K_2(\tau)$ has yet not been derived from the Navier–Stokes equation, this definition is similar to the definition of the Eulerian inertial range. However, it is common to use $\frac{\xi_n^L}{\xi_2^L}$. This enforces $\xi_2^L = 1$.

The compensated function $\frac{K_2(\tau)}{\varepsilon\,\tau}$ is plotted in figure VII.27. The calculated inertial range is ranging from 1.1 τ_η to 5.7 τ_η. Power law functions were fit with Gnuplot to the inertial range to obtain the ξ_n^L. The results are shown in figure VII.29 and table VII.5. Our values are in very good agreement to a measurement at the same $R_\lambda \approx 200$ [30, 35]. Although the predicted values are bigger than our measured scaling exponents, [35] indicates that this difference mainly due to the low Reynolds number.

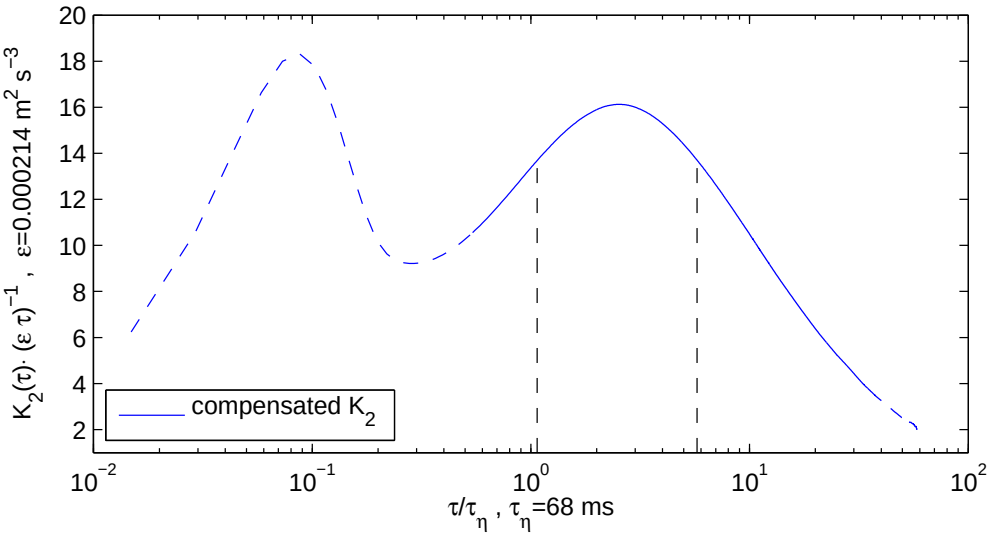

Figure VII.27: Compensated Lagrangian second order structure function of velocity at 1.66 Hz (+500 rpm) (bMV). $\frac{K_2(\tau)}{\varepsilon\,\tau}$ was measured at a propeller speed of 1.66 Hz (+500 rpm) (bMV). The dashed regions in $K_2(\tau)$ denote regions of high uncertainty. The inertial range is set to be between the two dashed lines. The latter were chosen such that the value of the compensated K_2 is 85% of the enclosed maximum of K_2. Thus, the inertial range is between 1.1 τ_η and 5.7 τ_η.

[13] $\varepsilon^{avg} = \frac{1}{N}\sum_{i=1}^{N}$ and $D_p^{avg} = \frac{1}{N}\sum_{i=1}^{N} D_i$

[14] $\left(\frac{1}{N}\sum_{i=1}^{N}\varepsilon\right)^{p/3} = \frac{1}{N}\sum_{i=1}^{N}(\varepsilon_i)^{p/3}$

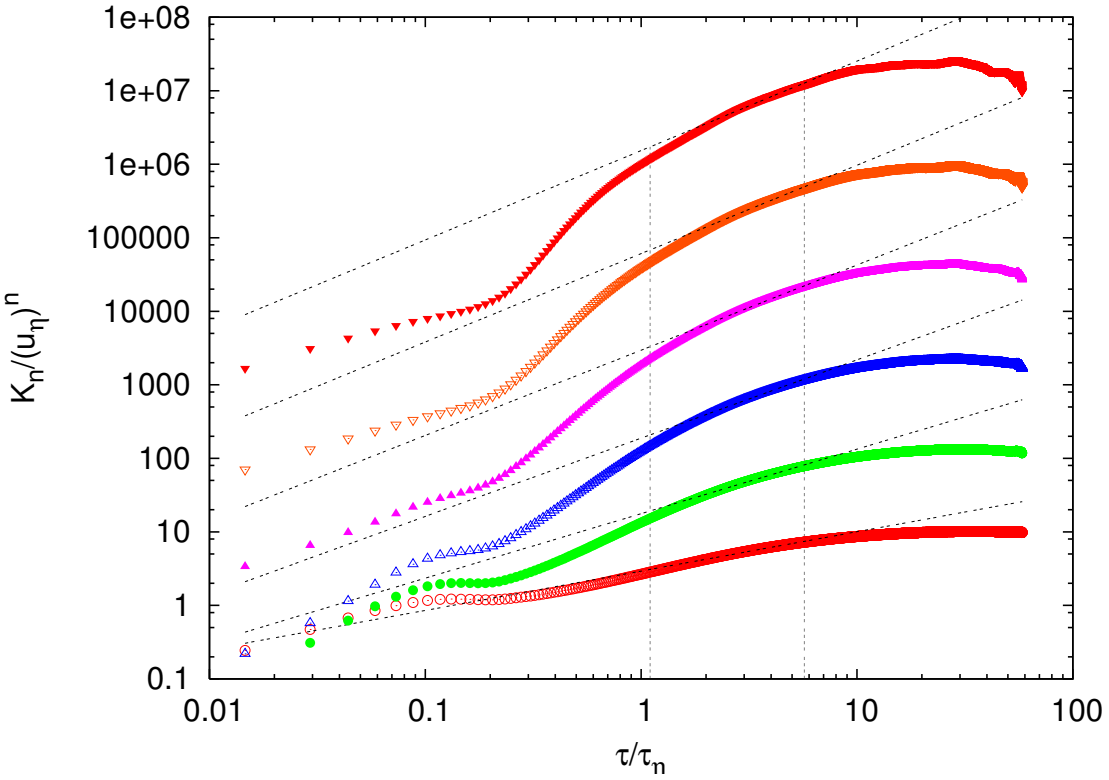

Figure VII.28: Dimensionless Lagrangian $n-$order structure function of velocity at 1.66 Hz (+500 rpm) (bMV). K_n was normalized by u_η^n to make the function dimensionless. This scaling introduces only a shift to the K_n. It does not change the scaling. The order starts from 1 and increases from the bottom to the top. The dashed lines show power laws which were fitted to the inertial rage (see figure VII.27). The inertial range is indicated though the two dashed vertical lines.

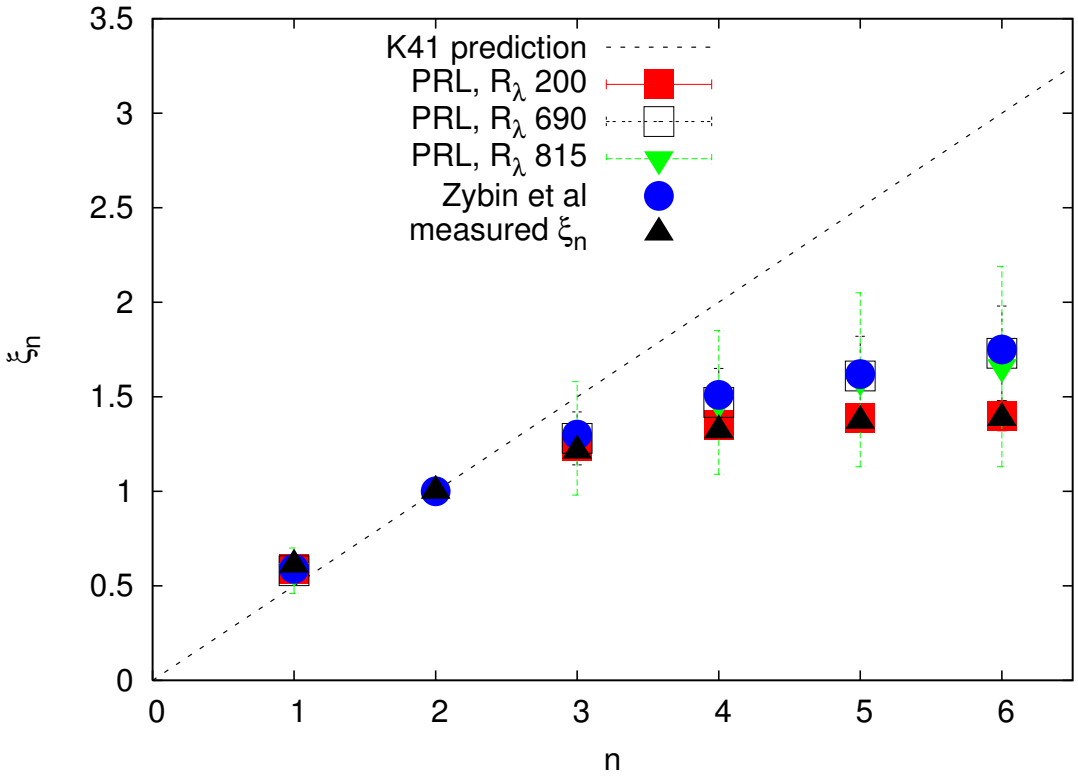

Figure VII.29: Exponents of the Lagrangian structure function of velocity at 1.66 Hz (+500 rpm) (bMV). The scaling exponents were obtained in figure VII.28 through power law fits to K_n in the Lagrangian inertial range. *Zybin* et al denotes the prediction from [34], whereas *PRL* denotes the measurements published [30, 35]. The dashed line show scaling according to K41. Clearly, no K41 scaling was not observed. Our data (▲) is in very good agreement with the measurement (■) at the same Reynolds number of $R_\lambda \approx 200$ [30, 35]. With increasing Reynolds numbers the measurements approach their prediction.

Lagrangian structure functions of position

The same methods to obtain the scaling exponents of velocity can be used to predict the behavior of the Lagrangian structure function of position, $R_n(\tau)$. The latter is defined as

$$R_n(\tau) = \langle |\mathbf{x}(t+\tau) - \mathbf{x}(t)|^n \rangle \tag{VII.24}$$

They calculated [1] that $R_n(\tau) \propto \tau^3$ in the inertial range for all $n > 3$. The first ten structure functions of position at random forcing and forcing at 1.66 Hz (+500 rpm) are shown in figure VII.31 and figure VII.28. In a log-log plot all R_n with $n > 3$ should be parallel in the inertial range. Clearly, both figures do not show this behavior. For a further investigation power law functions were fitted to $R_n(\tau)$ of forcing at 1.66 Hz (+500 rpm) in the inertial range. The latter was taken from the Lagrangian structure function, K_2, as discussed before. The obtained exponents, β_n^L, are shown in figure VII.29 and table VII.4. The measured exponents, β_n^L, seem to proportional to the order n. With the help of a linear fit, we determined

$$\beta^L(n) = (0.8984 \pm 0.0088) \cdot n \tag{VII.25}$$

In other words

$$R_n(\tau) \propto \tau^{0.9\,n} \tag{VII.26}$$

We also plotted the compensated structure function, $\frac{R_n}{\tau^3}\frac{\tau_\eta^3}{\eta^n}$ for $n > 3$ in figure VII.32. The compensated R_n show a plateau region for $t > 8\tau_\eta$. However, this region is only a few τ_η wide and depends on the order, n, of the structure function. That is in agreement with the results from figure VII.31 and VII.33 discussed before.

Thus, the prediction of Zybin *et al* [1] could not be verified at $R_\lambda \approx 200$. However, we can try to relate the linear dependence of β_n^L to its physical meaning. The inner part of R_n, $\mathbf{x}(t+\tau) - \mathbf{x}(t)$ can be expressed with the velocity

$$\mathbf{x}(t+\tau) - \mathbf{x}(t) = \int_t^{t+\tau} \mathbf{u}(t')dt' \tag{VII.27}$$

Inserting (VII.27) into equation (VII.24) yields

$$R_n(\tau) = \langle |\mathbf{x}(t+\tau) - \mathbf{x}(t)|^n \rangle = \left\langle \left| \int_t^{t+\tau} \mathbf{u}(t')dt' \right|^n \right\rangle \tag{VII.28}$$

We can decompose the velocity, $\mathbf{u}(t')$, into an average velocity, $\langle \mathbf{u} \rangle$, plus fluctuations in the velocity, $\mathbf{u}'(t')$. The integral (VII.27) transforms then into

$$\int_t^{t+\tau} \mathbf{u}(t')dt' = \langle \mathbf{u} \rangle \tau + \int_t^{t+\tau} \mathbf{u}'(t')dt' \tag{VII.29}$$

If $\int_t^{t+\tau} \mathbf{u}'(t')dt'$ is small compared to $\langle \mathbf{u} \rangle \tau$, we get

$$R_n(\tau) = \langle |\mathbf{u}\,\tau|^n \rangle \tag{VII.30}$$

In other words,

$$R_n \propto \tau^n \tag{VII.31}$$

which is close to our observation $R_n \propto \tau^{0.9\,n}$. The deviation is probably mainly due to the negligence of $\int_t^{t+\tau} \mathbf{u}'(t')dt'$. Moreover, measurement errors introduce a further bias. Yet, this first approximation yields a result comparable to the observation.

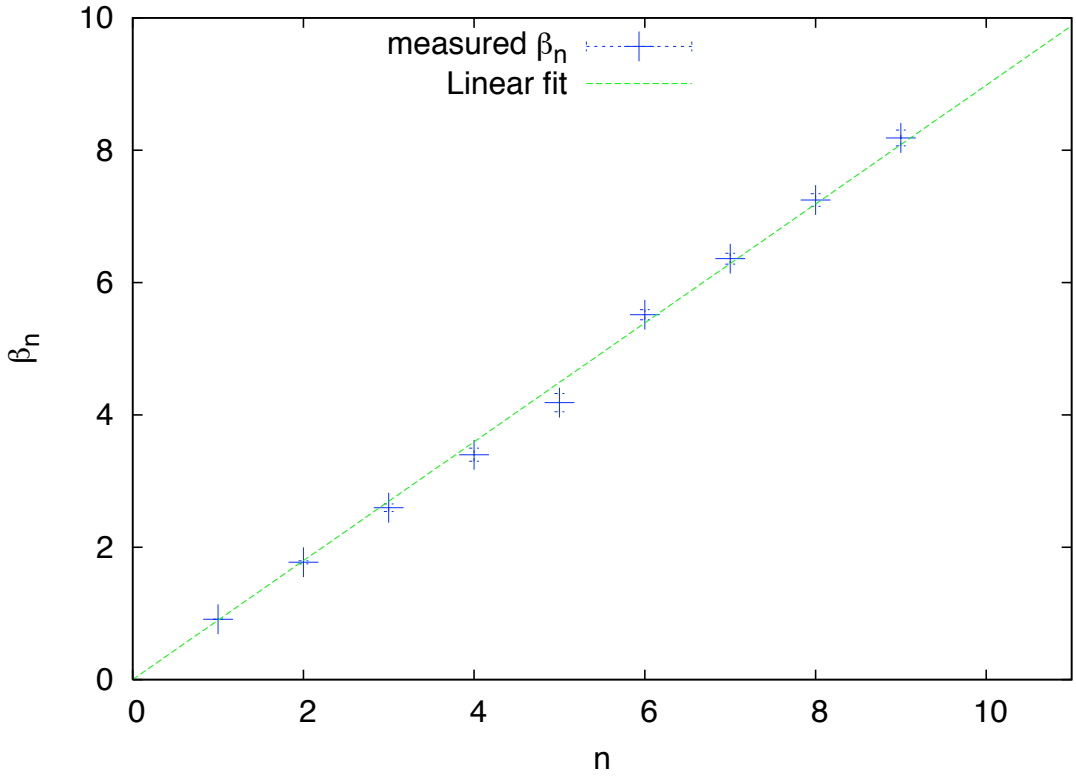

Figure VII.30: Exponents of the Lagrangian structure function of position. Power laws were fitted to the Lagrangian structure function of position with forcing at 1.66 Hz (+500 rpm) (bMV) (figure VII.33) to the inertial range (see figure VII.27). According to [1], the scaling exponents obtained, β_n^L, should be 3 for order four and higher. Clearly, this was not observed. On the contrary, the exponents, β_n^L, increase linear with n as indicated by the linear fit, $\beta^L(n) = (0.8984 \pm 0.0088) \cdot n$. In other words, $R_n(\tau) \propto \tau^{0.9\,n}$.

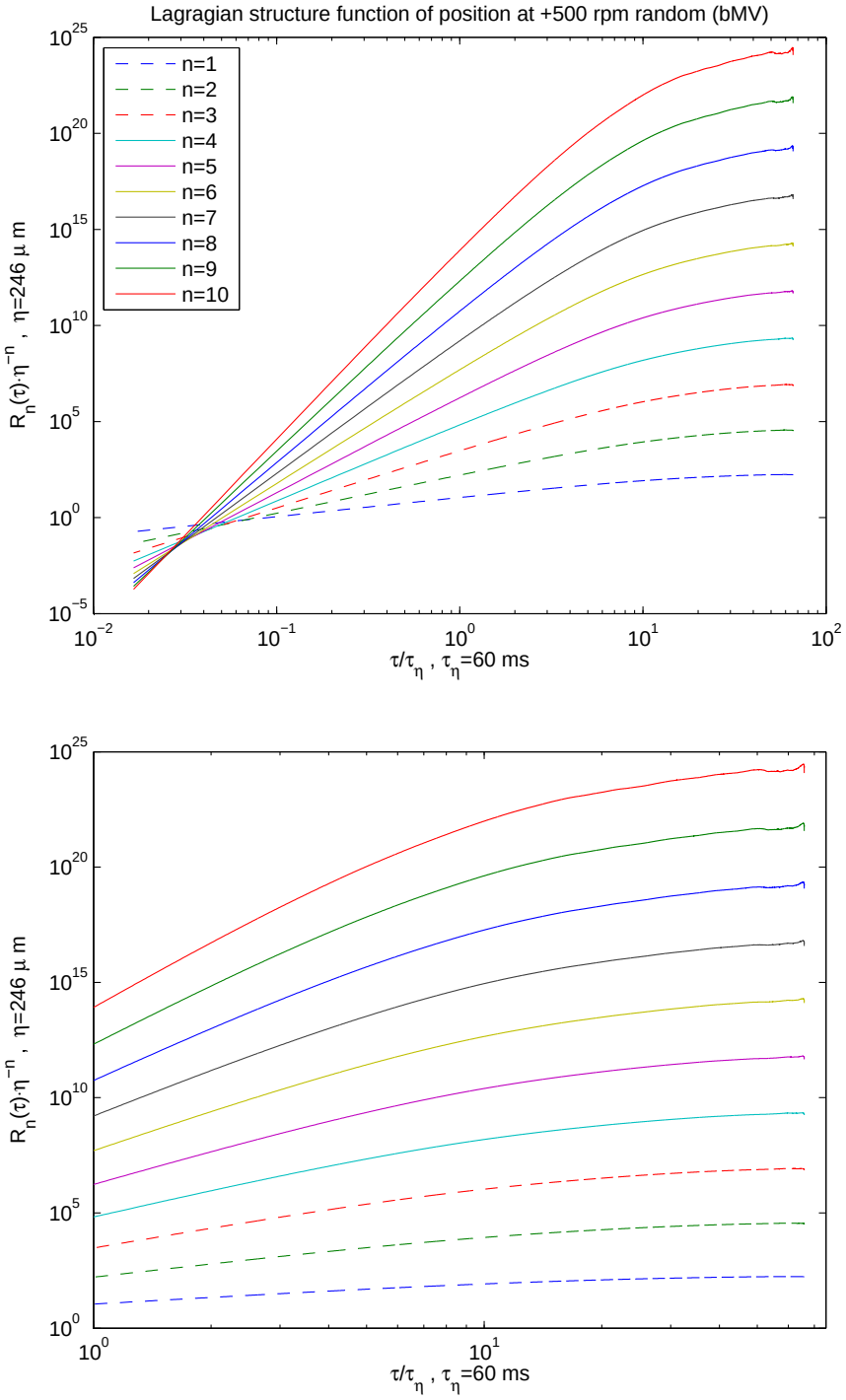

Figure VII.31: Dimensionless Lagrangian $n-$order structure function R_n/η^n of position. The top figure shows the Lagrangian structure functions of position for the random forcing (bMV). The bottom figure is an enlargement of the probable inertial range, the legend did not change. For the first three R_n/η^n (dashed curves) no prediction was made. According to [1] all R_n/η^n with $n > 3$ should scale with τ^3. Therefore, the R_n/η^n should be approximately parallel in the inertial range. Our data allows us to cover a possible inertial range between 1 τ_η and approximately 40 τ_η. Obviously, the $R_{n>3}$ are not parallel in this range. Moreover, using the inertial range found in figure VII.27, the scaling exponents, β_n^L are increasing with the order, n, of R_n.

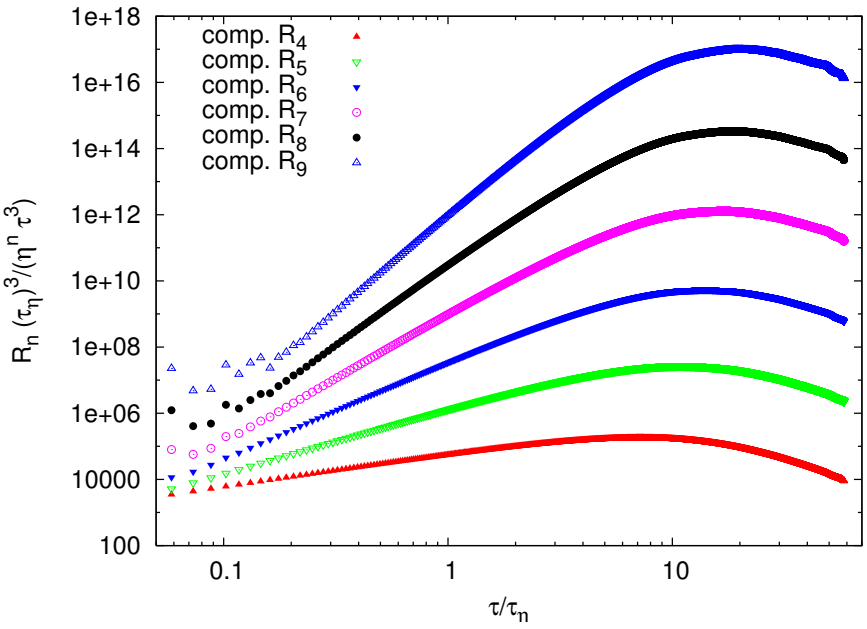

Figure VII.32: Compensated Lagrangian $n-$order structure function of position. Clockwise forcing at 1.66 Hz (+500 rpm) (bMV) was used to obtain the compensated dimensionless Lagrangian structure function of position $\frac{R_n}{\tau^3}\frac{\tau_\eta^3}{\eta^n}$ for $n > 3$. A plateau region can be observed for $t > 8\tau_\eta$. However, this region is only a few τ_η wide, and the location of the peak depends on the order, n, of the structure function.

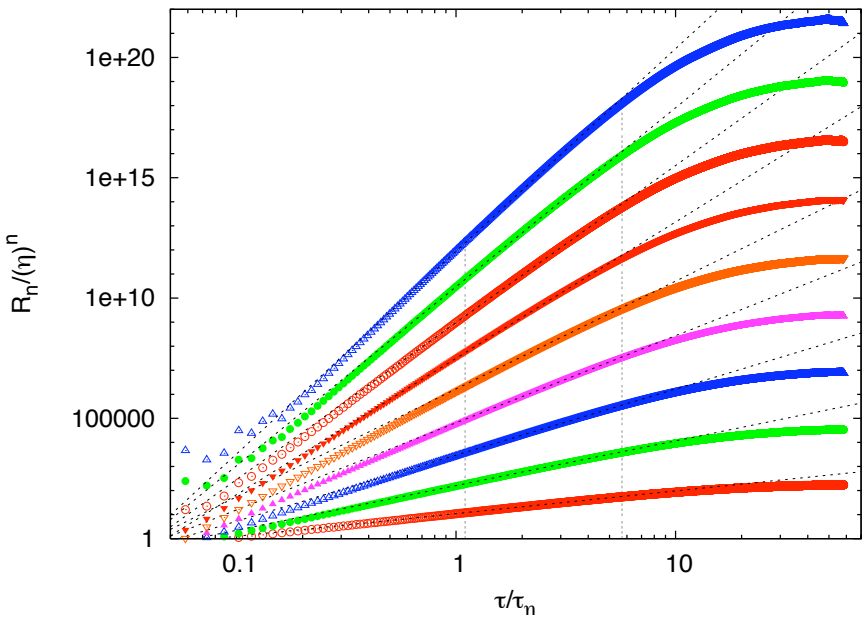

Figure VII.33: Dimensionless Lagrangian $n-$order structure function of position. Clockwise forcing at 1.66 Hz (+500 rpm) (bMV) was used to obtain the dimensionless Lagrangian structure function of position R_n/η^n. The order, n, is starting from 1 and increasing from the bottom to the top. The black dashed lines show power laws which were fitted to the inertial rage (as obtained in figure VII.27).

Table VII.4: Measured scaling exponents β_n^L the Lagrangian structure function of position R_n. The measured β_n^L were obtained at $R_\lambda \approx 200$ at forcing with 1.66 Hz (+500 rpm) (bMV).

Order n	1	2	3	4	5	6	7	8	9
β_n^L	0.91	1.77	2.60	3.40	4.19	5.51	6.36	7.25	8.2

Table VII.5: Measured and predicted Lagrangian scaling exponents $\frac{\xi_n^L}{\xi_2^L}$. The measured ξ_n^L were obtained at $R_\lambda \approx 200$ at forcing with 1.66 Hz (+500 rpm) (bMV).

Order n	$\frac{\xi_n^L}{\xi_2^L}$	value from [34]
1	0.61	0.59
2	1	1
3	1.21	1.30
4	1.32	1.51
5	1.37	1.65
6	1.38	1.75

VIII Conclusion and Outlook

The Lagrangian Exploration Module was characterized at different propeller speeds and different forcing schemes with Particle Tracking Velocimetry. It was demonstrated that the LEM produced nearly isotropic and homogeneous turbulence in a volume of the size of the integral length scale. The turbulence was characterized by values of R_λ up to about 350. Higher turbulence levels under similar experimental conditions are most likely achievable by increasing the speed of the propellers, or by using a different propeller design. The mean flow was shown to be of the order of a few $\frac{mm}{s}$, and the fluctuating velocity was found to be several times stronger than the underlying mean-flow. Consequently, the LEM is a good tool for Lagrangian experiments.

It is possible to change the properties of the flow by adjusting the speed of each propeller individually. By driving the flow in two different ways, we investigated the differences both in the turbulence and the mean flow field of the two experiments. In the first run, the propeller speed was held constant and in the second, the propeller speed changed randomly over time. We ensured that the energy rate injected was the same in both experiments. Only small variations in the turbulence and the mean flow were observed between the data obtained with these two different forcings. This recalls the idea of Kolmogorov, which is that the statistics at scales much smaller than the scales at which the turbulence is created are independent of the way the turbulence was created.

The predictions by Zybin *et al* [1, 33, 34] were compared to results obtained in the LEM at $R_\lambda \approx 200$. Good agreement was found for the scaling exponents, ξ_n^L, of the Lagrangian $n-$th order structure functions of velocity, $K_n(\tau)$. The scaling exponents obtained in the LEM were also in very good agreement to those obtained in a French-Washing machine at the same turbulence level [30, 35].

Furthermore, the scaling exponents, β_n^L, of the Lagrangian $n-$th order structure function of position, $R_n(\tau)$, were measured at $R_\lambda \approx 200$. In contrast to [1], β_n^L did not appear to be 3 for $n > 3$. Moreover, we observed $\beta_n^L = (0.898 \pm 0.009) \cdot n$ for $n < 10$. Therefore, this prediction is not supported by our experiments at the turbulence level investigated.

A possible future project for the Lagrangian Exploration Module is a detailed study of how to generate turbulence. After automatizing the measuring and analysis process, one could use genetic algorithms to explore the space of possible forcings more quickly than with our present analysis methods. The insights gained through this research could also improve the design of actively–driven grids in wind-tunnels.

The large number of windows on the LEM enables us to use several measurement techniques at the same time, thus allowing more stringent tests and comparisons of new or existing instruments. For example, new physical insights can be gained through the simultaneous observation of particles of different sizes or types, and from

the combination of Eulerian with Lagrangian measurement techniques.

A further possible project is to use pressurized sulfur-hexafluoride (SF_6) as a working fluid in the LEM. The Göttingen U–Boot pressure vessel provides SF_6 at pressures up to 15 bar. SF_6 has a kinematic viscosity of $1.5 \cdot 10^{-7}\ m^2\ s^{-1}$ at this pressure. Since the maximum turbulence level observable is limited mainly by the Kolmogorov time scale and the frame rate of the cameras, SF_6 would allow us to reach higher turbulence levels up to $R_\lambda \approx 3000$.

In addition, it is planned to use the LEM to investigate the behavior of copepods in a turbulent environment. These small crustaceans are an important food source for fish larvae.

IX Acknowledgements

This project would never have been possible without the help of many people.

First of all, I want to thank my advisor, Professor Eberhard Bodenschatz, for the opportunity to conduct the diploma thesis in his group and his confidence in my ability to build the new apparatus. While working on my diploma thesis, he was very kind to nominate me for the Lindau Nobel Laureate Meeting, which I enjoyed very much. I have greatly appreciated working in his group and enjoyed many fruitful discussions. I am also very grateful to Haitao Xu. He introduced me to the work as an experimentalist. Without his independent analysis of the data my analysis code would probably still tell me that water is created inside the LEM. Also, I want to express my gratitude to Jean-François Pinton, Mickaël Bourgoin and Yoann Gasteuil for many fruitful discussions at the ENS Lyon. I wish to thank the technical staff of the machine shop of the Max–Planck–institute of dynamics and self-organization for the fast construction of technical components, in general. In particular, I am grateful to Mr. Schminke for his aid in the conceptual design of these. Furthermore, I want to thank Sarah, Christian, Murkel and Greg for continuously reading and correcting drafts of my diploma thesis. Finally, I would not have survived without the support of my family and my friends. Thank you.

Bibliography

[1] K. P. Zybin, V. A. Sirota, A. S. Ilyin, and A. V. Gurevich. Lagrangian structure functions in fully-developed hydrodynamical turbulence. *arXiv:0712.3944v1*, 2007.

[2] G.K. Bachelor. *an introduction to fluid dynamics*. Cambridge University Press, 2000.

[3] A. Kolmogorov. The local structure of turbulence in incompressible viscous fluid for very large Reynolds' numbers. *Dokl. Akad. Nauk SSSR*, 30:301–305, 1941.

[4] Boris Shraiman and Eric Siggia. Scalar turbulence. *Nature*, 405:639–646, 2000.

[5] G. Falkovich, K. Gawedzki, and M Vergassola. Particles and fields in turbulence. *Reviews of modern physics*, 73:913–975, November 2001.

[6] W. H. Snyder and J. L. Lumley. Some measurements of particle velocity autocorrelation functions in a turbulent flow. *Journal of Fluid Mechanics*, 48:41–71, 1971.

[7] Federico Toschi and Eberhard Bodenschatz. Lagrangian properties of particles in turbulence. *Annual Review of Fluid Mechanics*, 41(1), 2009.

[8] Stephen B. Pope. *Turbulent Flows*. Cambridge University Press, 2000.

[9] L.D. Landau and E. M. Lifschitz. *Lehrbuch der theoretischen Physik – Hydrodynamik*, volume 4. Akademie Verlag, 5 edition, 1991.

[10] Uriel Frisch. *Turbulence: The Legacy of A. N. Kolmogorov*. Cambridge University Press, 1995.

[11] H. Tennekes and J. L. Lumley. *A First Course in Turbulence*. MIT Press, 1972.

[12] Greg A. Voth, A. La Porta, Alice M. Crawford, Jim Alexander, and Eberhard Bodenschatz. Measurement of particle accelerations in fully developed turbulence. *Journal of Fluid Mechanics*, 469:121–160, 2002.

[13] X. Shen and Zellman Warhaft. The anisotropy of the small scale structure in high Reynolds number ($R_\lambda \sim 1000$) turbulent shear flow. *Physics of Fluids*, 12(11):2976–2989, 2000.

[14] Luca Biferale and Federico Toschi. Anisotropic homogeneous turbulence: Hierarchy and intermittency of scaling exponents in the anisotropic sectors. *Physical Review Letters*, 86(21), 2001.

[15] G. K. Batchelor. The theory of axisymmetric turbulence. *Proceedings of the Royal Society of London. Series A, Mathematical and Physical Sciences*, 186(1007):480–502, 1946.

[16] S. Ayyalasomayajula, A. Gylfason, L. R. Collins, E. Bodenschatz, and Z. Warhaft. Lagrangian measurements of inertial particle accelerations in grid generated wind tunnel turbulence. *Physical Review Letters*, 97(144507), 2006.

[17] Cameron Tropea, Alexander Yarin, and John F. Foss, editors. *Springer Handbook of Experimental Fluid Dynamics*. Springer-Verlag Berlin-Heidelberg, 2007.

[18] Genevieve Comte-Bellot. Hot–wire anemometry. *Annual Review of Fluid Mechanics*, 8:209–231, 1976.

[19] B. Lehmann, H. Nobach, and C. Tropea. Measurement of acceleration using the laser Doppler technique. *Measurement Science and Technology*, 13(9):1367–1381, 2002.

[20] R. J. Adrian. Particle-imaging techiniques for experimetal fluid-mechanics. *Annual Review of Fluid Mechanics*, 23:261–304, 1991.

[21] John R Cressman, Jahanshah Davoudi, Walter I Goldburg, and Jörg Schumacher. Eulerian and lagrangian studies in surface flow turbulence. *New Journal of Physics*, 6(53), 2004.

[22] M. K. Rivera and R. E. Ecke. Pair dispersion and doubling time statistics in two-dimensional turbulence. *Physical Review Letters*, 95(194503), 2005.

[23] Nicolas Mordant, Pascal Metz, Jean-Francois Pinton, and Olivier Michel. Acoustical technique for Lagrangian velocity measurement. *Review of scientific instruments*, 76, 2005.

[24] R. Volk, N. Mordant, G. Verhille, and J.-F. Pinton. Laser Doppler measurement of inertial particle and bubble accelerations in turbulence. *Europhysics Letters*, 81(34002), February 2008.

[25] W.L. Shew, Y. Gasteuil, M. Gibert, P. Metz, and J.F. Pinton. Instrumented tracer for Lagrangian measurements in Rayleigh-Bénard convection. *Review of Scientific Instruments*, 78:065105, 2007.

[26] R. Tsai. A versatile camera calibration technique for high-accuracy 3D machine vision metrology using off-the-shelf TV cameras and lenses. *IEEE Journal of Robotics and Automation*, 3(4):323–344, 1987.

[27] N.T. Ouellette, H. Xu, and E. Bodenschatz. A quantitative study of three-dimensional Lagrangian particle tracking algorithms. *Experiments in Fluids*, 40(2):301–313, 2006.

[28] Haitao Xu. Tracking Lagrangian trajectories in position–velocity space. *Measurement Science and Technology*, 19(075105), 2008.

[29] N. Mordant, A.M. Crawford, and E. Bodenschatz. Experimental lagrangian acceleration probability density function measurement. *Physica D*, 193(1-4):245 – 251, 2004.

[30] Nicholas Ouellette. *Probing the satistical structure of turbulence with measurements of tracer partcile tracks*. PhD thesis, Cornell University, 2006.

[31] A. La Porta, Greg A. Voth, Alice M. Crawford, Jim Alexander, and Eberhard Bodenschatz. Fluid particle accelerations in fully developed turbulence. *Nature*, 409(6823):1017–1019, 2001.

[32] Haitao Xu, Nicholas T Ouellette, and Eberhard Bodenschatz. Evolution of geometric structures in intense turbulence. *New Journal of Physics*, 10(013012), 2008.

[33] K. Zybin, V. Sirota, A. Il'in, and A. Gurevich. Generation of small-scale structures in well-developed turbulence. *Journal of Experimental and Theoretical Physics*, 105(2):455–466, 2007.

[34] K. P. Zybin, V. A. Sirota, A. S. Ilyin, and A. V. Gurevich. Lagrangian statistical theory of fully developed hydrodynamical turbulence. *Physical Review Letters*, 100(17):174504, 2008.

[35] Haitao Xu, Mickael Bourgoin, Nicholas T. Ouellette, and Eberhard Bodenschatz. High order Lagrangian velocity statistics in turbulence. *Physical Review Letters*, 96(2):024503, 2006.